

AD A091853

MARTIN MARIETTA

Martin Marietta Laboratories

ARO 14543.4-P

TEL

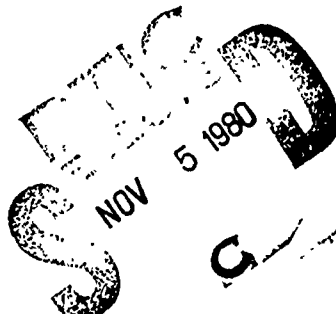
MML TR 80-38c

DP

INVESTIGATION OF SURFACE

PLASMON DISPERSION

Final Report



W.P. Chen
and
J.M. Chen

September 30, 1980

U.S. Army Research Office
P.O. Box 12211
Research Triangle Park, NC 27709

Contract No. DAAG29-77-C-0036

Martin Marietta Laboratories
1450 South Rolling Road
Baltimore, Maryland 21227

DISTRIBUTION STATEMENT A

Approved for public release;
Distribution Unlimited

8011 03 098

REPORT DOCUMENTATION PAGE		READ INSTRUCTIONS BEFORE COMPLETING FORM
1. REPORT NUMBER MML TR80-38c	2. GOVT ACCESSION NO. AD-A091	3. RECIPIENT'S CATALOG NUMBER 863
4. TITLE (and Subtitle) ⑥ Investigation of Surface Plasmon Dispersion	5. TYPE OF REPORT & PERIOD COVERED ⑦ FINAL REPORT 16 Aug 77 - 15 Aug 80	
7. AUTHOR(s) W. P. Chen and J. M. Chen	14) PERFORMING ORG. REPORT NUMBER MML-TR-80-38c	8. CONTRACT OR GRANT NUMBER(s) DAAG29-77-C-0036/m
9. PERFORMING ORGANIZATION NAME AND ADDRESS Martin Marietta Laboratories 1450 South Rolling Road Baltimore, Maryland 21227	10. PROGRAM ELEMENT, PROJECT, TASK AREA & WORK UNIT NUMBERS 11) DAAG29-77-C-0036/m	
11. CONTROLLING OFFICE NAME AND ADDRESS Department of the Army U.S. Army Research Office, P.O. Box 12211 Research Triangle Park, North Carolina 27709	12. REPORT DATE 30 September 1980	
14. MONITORING AGENCY NAME & ADDRESS (if different from Controlling Office) ⑩ Wenpeng Chen	13. NUMBER OF PAGES 15) 12	
16. DISTRIBUTION STATEMENT (of this Report) Approved for public release, distribution unlimited. Jan-Mo Chen	15. SECURITY CLASS. (of this report) Unclassified	
17. DISTRIBUTION STATEMENT (of the abstract entered in block 20, if different from report) ⑯ DAKO	15a. DECLASSIFICATION/DOWNGRADING SCHEDULE ⑯ 128	
18. SUPPLEMENTARY NOTES THE VIEW, OPINIONS, AND/OR FINDINGS CONTAINED IN THIS REPORT ARE THOSE OF THE AUTHOR(S) AND SHOULD NOT BE CONSTRUED AS AN OFFICIAL DEPARTMENT OF THE ARMY POSITION, POLICY, OR DECISION, UNLESS SO DESIGNATED BY OTHER DOCUMENTATION.		
19. KEY WORDS (Continue on reverse side if necessary and identify by block number) Surface plasma waves, Attenuated-total-reflection, Thin metal film, Cs monolayer, Narrow-Beam Excitation, Dielectric Constant, Photoemission, Diode, Spectroscopy		
20. ABSTRACT (Continue on reverse side if necessary and identify by block number) See other side.		

DD FORM 1 JAN 73 1473

407998

Abstract

The attenuated-total-reflection (ATR) technique was used to study surface plasma wave (SPW) dispersion of Cs- and Cs-O-covered Ag surfaces. Our data indicate that SPW are heavily damped by an adsorbed Cs submonolayer with no obvious change in their wavevectors. However, in the presence of an adsorbed Cs-O submonolayer, SPW show changes in their wavevectors, but without any obvious damping. Based on our theoretical analysis, we have concluded that the Cs-Ag and the Cs-O-Ag surface layers are strongly absorptive and transparent, respectively. The relationship between the SPW damping and Cs coverage indicates that SPW can be damped by a photoelectric effect.

A least-squares fit for the ATR data was used to determine the optical constant $\epsilon = \epsilon' + i\epsilon''$ and thickness, d , of Ag films thinner than 600 Å. We found two sets of ϵ and d from the fitting for each wavelength that can be distinguished by simultaneously fitting data for another wavelength. For a slowly deposited Ag film with mass thickness t smaller than 250 Å, we found that, for decreasing t 1) the derived ϵ'' becomes less negative, 2) ϵ'' increases dramatically, and 3) the derived effective thickness is about 200 Å, which suggests that the Ag films are more likely to be island types with an island height of 200 Å.

SPW were also used to enhance photoemission signals from a cathode and to enhance the photovoltaic signal from a Si-Au diode.

Accession For	
NTIS	Govt
DTIC T 3	<input type="checkbox"/>
Unannexed	<input type="checkbox"/>
Justification	
By	
Distribution/	
Availability Class	
Dist	Avail and Special

MML TR 80-38c

INVESTIGATION OF SURFACE PLASMON DISPERSION

Final Report

September 30, 1980

U.S. Army Research Office
P.O. Box 12211
Research Triangle Park, North Carolina 27709

Contract No. DAAG29-77-C-0036

Wenpeng Chen

Wenpeng Chen

Jar-mo Chen

Jar-Mo Chen

Martin Marietta Laboratories
1450 South Rolling Road
Baltimore, Maryland 21227

THE FINDINGS IN THIS REPORT ARE NOT TO BE
CONSTRUED AS AN OFFICIAL DEPARTMENT OF
THE ARMY POSITION, UNLESS SO DESIGNATED
BY OTHER AUTHORIZED DOCUMENTS.

TABLE OF CONTENTS

	<u>Page</u>
LIST OF FIGURES.	
I. INTRODUCTION.	1
II. SPW STUDY OF Ag SURFACES COVERED WITH SUBMONOLAYERS OF Cs AND Cs-O.	4
III. SPW STUDY OF THIN (30 Å -500 Å) Ag FILMS.	9
A. DETERMINATION OF DIELECTRIC CONSTANT AND THICKNESS OF METAL FILM	9
B. DEPENDENCE OF RESONANCE OF SPW ON FILM THICKNESS. .	12
IV. SPW ENHANCEMENT	15
A. SPW ENHANCED - PHOTOEMISSION.	15
B. SPW-INDUCED COUPLING OF EM WAVES IN A Si-Au DIODE .	19
V. BIBLIOGRAPHY.	22
APPENDIX I - Surface Plasma Wave Study of Submonolayer Cs and Cs-O Covered Ag Surfaces	
APPENDIX II - On the Use of Surface Plasma Waves for Determination of the Thickness of Optical Constants of Thin Metallic Films	
APPENDIX III - Narrow-Beam Excitation of Electromagnetic Modes in Prism Configurations	

LIST OF FIGURES

<u>Figure</u>		<u>Page</u>
1	Typical R vs α curves for a Ag-vacuum interface, for the Ag surface in the presence of 2.5×10^{14} atoms/cm ² of Cs, and the Cs layer exposed to O ₂ gas.	5
2	Variation of reflectance (R) and photoemission current (I) with Cs coverage. α was set equal to α_{ATR} for a fresh Ag-vacuum interface and the reflectance of a He-Ne laser light was measured during Cs deposition	7
3	Data fitting of measured R versus $K_x^1/(\omega/c)$ curves at 6328 Å and 4358 Å. Solid curves are data. Calculated reflectances for each fitting are shown by the symbols Δ , \bullet , Δ , and \circ . For Δ : $(t, \epsilon_1) = (387 \text{ \AA}, -17.45 + i 0.92)$, \bullet : $(483 \text{ \AA}, -16.72 + i 1.66)$, Δ : $(567 \text{ \AA}, -5.25 + i 0.53)$, and \circ : $(467 \text{ \AA}, -5.25 + i 0.32)$	10
4	a) Data for the resonant reflectance R versus cK/ω curves of the SPW at the He-Ne laser frequency (6328 Å) in a prism-Ag-vacuum configuration for various Ag film thicknesses t. b) The corresponding calculated R versus cK/ω curves using $n = 1.52$ and a t -independent $\epsilon_1 = -16 + i 0.52$	13
5	Variation of reflectance R with θ , and photoemission current I with θ at $\lambda = 6328 \text{ \AA}$. The angular positions of the peak of I and the dip of R differ by 0.05°	16
6	Experimental configuration for enhancement of photoemission from a commercial S-1 cathode.	17

LIST OF FIGURES (continued)

<u>Figure</u>		<u>Page</u>
7	The enhancement factor (the ratio of photo-emission currents with and without the prism) vs wavelength.	18
8	The reflectance minimum and the photovoltage maximum which occur at resonant coupling of SPW. The inset shows the Otto configuration	20

I. INTRODUCTION

In this final report, we will summarize the findings of our research under this contract on surface plasma wave (SPW) dispersion. The objectives of this research program are: 1) to use the attenuated-total-reflection (ATR) technique to study SPW dispersion of Cs and Cs-O covered Ag surfaces, 2) to investigate the effects of ATR-enhanced photo-emission from Cs-covered Ag surfaces, and 3) to investigate the feasibility of ATR-induced coupling of electromagnetic (EM) waves into planar solid state devices.

Surface plasma waves are EM waves that can propagate along a metal-vacuum interface; their amplitude decreases exponentially with distance from the interface. Let us consider a case in which the metal is an optically isotropic, homogeneous medium characterized by a dielectric constant, $\epsilon_1(\omega)$, and with magnetic permeability $\mu = 1$. For a model in which the interface is considered a sharp geometric boundary, the SPW of the metal-vacuum interface are transverse-magnetic (TM)-polarized, and their dispersion can be given by¹:

$$K^2 = \frac{\epsilon_1(\omega) \epsilon_2}{\epsilon_1(\omega) + \epsilon_2} \frac{\omega^2}{c^2}, \quad K = \text{Re}(K) + i \text{Im}(K) \quad (1)$$

where K and ω are the wavevector and frequency of the SPW, respectively, $\epsilon_2 = 1$ is the dielectric constant of vacuum, and c is the speed of light in vacuum.

Surface plasma waves exist in the frequency region in which $\epsilon'_1(\omega) < -1$, where $\epsilon_1(\omega) = \epsilon'_1(\omega) + i\epsilon''_1(\omega)$. The real parts of their wavevectors are larger than the wavevector of corresponding light in vacuum,

i.e., $\text{Re}(K) > (\omega/c)$. Therefore, SPW are nonradiative and cannot couple directly with light in vacuum. However, the Otto² and Kretschmann³ ATR prism configurations can be used to augment the wavevectors and therefore excite SPW at an air-metal interface. The Otto configuration is formed by placing a prism above the metal surface, leaving an air gap; the Kretschmann configuration is formed by depositing a thin metal film on the base of a prism. In the Kretschmann configuration, SPW also exist at the prism-metal interface. However, only the SPW at the air-metal interface can be excited in the ATR configuration.¹ When light is incident upon the prism-metal interface at angles θ larger than the critical angle θ_c , it can create an evanescent EM wave with the proper parallel component of wavevector K_x^1 to match the wavevector of SPW. Here $\theta_c = \sin^{-1}(1/n)$ and $n > 1$ is the index of refraction of the prism. Therefore, SPW can couple directly with light in the prism.

Under proper conditions, resonant coupling between SPW and light in the prism can occur. The resonance is a high Q phenomenon and results in high electric fields at the metal surface.^{1,4} These high electric fields are the key to this research program. Recently, there has been a growing interest in using visible and infrared light as probes for studying surfaces. Conventional optical spectroscopy, such as reflectance measurement, suffers from two deficiencies: 1) the sampling depth is on the order of 100 Å thick, much thicker than a monolayer; 2) incident light and its reflection from a highly reflective metal surface form a node in the electric field at the adsorbed layer that reduces the interaction between the adlayer and the EM field. However, the weak interaction between an adlayer and the EM field can be enhanced by using SPW as

a surface probe. It has been demonstrated that roughly 0.2% of a monolayer can be detected in this way.⁵ As part of the work conducted under this contract, we performed a spectroscopic study of submonolayers (see Appendix I) in which the coverages of the submonolayers Cs and Cs-O were monitored by work function variation.

When SPW are used in an external photoemission or in a planar solid state device, the high electric field and its concentration at the investigated interface quite naturally lead to enhancement of photoemission intensity and device performance, respectively. Using such high electric fields and the dependence of SPW on the metal film thickness, we can also deduce the dielectric constant and the thickness of the metal film. A discussion of the method is given in Appendix II.

Appendix III is a review paper on narrow-beam excitation of EM modes in prism configurations, coauthored by W.P. Chen and Prof. E. Burstein.

In this report, we shall describe the results that we have obtained in the three areas: 1) SPW study of Ag surfaces covered with submonolayers of Cs and Cs-O, 2) SPW study of thin (30 Å-500 Å) Ag films, and 3) SPW-induced coupling of EM waves in a photocathode and a planar Si-Au photodiode. Results that have been published or submitted for publication will be discussed only briefly.

II. SPW STUDY OF Ag SURFACES COVERED WITH SUBMONOLAYERS OF Cs AND Cs-O

We have studied surface plasmon waves at a vacuum-Ag interface with and without a Cs (or Cs-O) overlayer. Experiments were performed in an ultrahigh vacuum chamber, using a Kretschmann prism-Ag-vacuum configuration, in the frequency region from $0.9 \times 10^4 \text{ cm}^{-1}$ to $2.2 \times 10^4 \text{ cm}^{-1}$. Monochromatic and collimated TM-polarized light was used to excite SPW at angles beyond the critical angle. As the angle of incidence was scanned, the reflectance R showed minima when SPW were excited.

Typical $R(\alpha)$ curves at SPW resonance are shown in Fig. 1 for the frequencies indicated. Both are shown for a Ag-vacuum interface with 1) no overlayer, 2) a Cs submonolayer, and 3) a Cs-O submonolayer. The Cs coverage measured was the coverage at which the photoemission signal started to saturate, equivalent to $2.5 \times 10^{14} \text{ atoms/cm}^2$. A comparison of the $R(\alpha)$ curves shows that: 1) the $R(\alpha)$ curves for a Cs submonolayer have broader half-widths ω_α , lower values of minimum reflectance R_{\min} , and show no obvious changes in the resonant angle α_{ATR} , and 2) the $R(\alpha)$ curves for a Cs-O submonolayer show no obvious changes of half-widths and R_{\min} , but appreciable change of α_{ATR} .

The spectra of the changes in R_{\min} and α_{ATR} (see Appendix I) showed that, on the one hand, R_{\min} can be reduced by up to 10% from $\omega = 0.9 \times 10^{14} \text{ cm}^{-1}$ to $\omega = 2.2 \times 10^{14} \text{ cm}^{-1}$ due to Cs adsorption. On the other hand, the oxidation of the Cs-covered Ag surface causes a change of α_{ATR} from 0° at $\omega = 0.9 \times 10^{14} \text{ cm}^{-1}$ to -0.4° at $\omega = 2.2 \times 10^{14} \text{ cm}^{-1}$. The data indicate that SPW are heavily damped by an adsorbed Cs submonolayer, with no obvious change in their wavevectors. However, in the

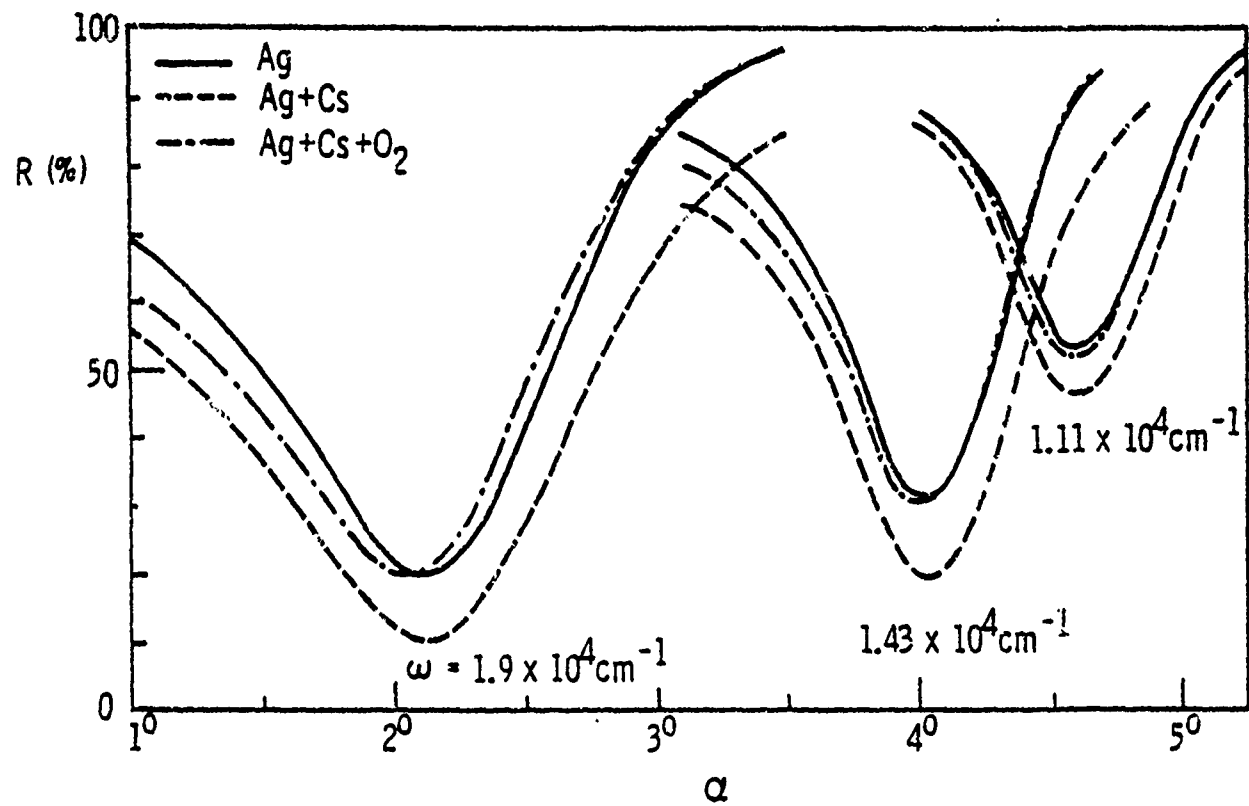


Figure 1. Typical R vs α curves for a Ag -vacuum interface, for the Ag surface in the presence of 2.5×10^{14} atoms/ cm^2 of Cs , and the Cs layer exposed to O_2 gas.

presence of an adsorbed Cs-O submonolayer, SPW show changes in their wavevectors, but without any obvious damping.

We also measured R versus the wavelength of light at several angles α . The spectra (see Appendix I) indicate no sharp structures, in agreement with the spectra of α_{ATR} , ω_a , and R_{\min} . The absence of sharp structures indicates that the electronic states of Cs-Ag and the Cs-O-Ag surface layers are likely to have energy bands rather than discrete energies.

We have analyzed the data presented in Appendix I using an optically anisotropic slab model to represent the surface layer, which includes the adlayer and the substrate surface atoms. The response to an electric field normal to the surface was set to be different from that parallel to the surface. Theoretically, the analysis seems somewhat arbitrary because the thickness of the surface layer is not well defined. However, the final result shows that choice of the thickness is not critical, and, when there is no resonant dipole transition normal to the surface, that the effect on the surface plasma waves depends only on the product of the adlayer coverage and its electric susceptibility per adatom. Based on this theoretical analysis, we have concluded that the Cs-Ag layer is strongly adsorptive and the Cs-O-Ag surface layer is transparent.

We also studied the relationship between Cs coverage and SPW. We set $\alpha = \alpha_{\text{ATR}}$ for a fresh Ag-vacuum interface and measured the reflectance of a TM-polarized He-Ne laser light during Cs deposition. The photoemission current was measured simultaneously. As shown in Fig. 2, at the initial stage of Cs deposition, R decreases linearly with deposition time t , which is equivalent to surface coverage. This is interpreted as

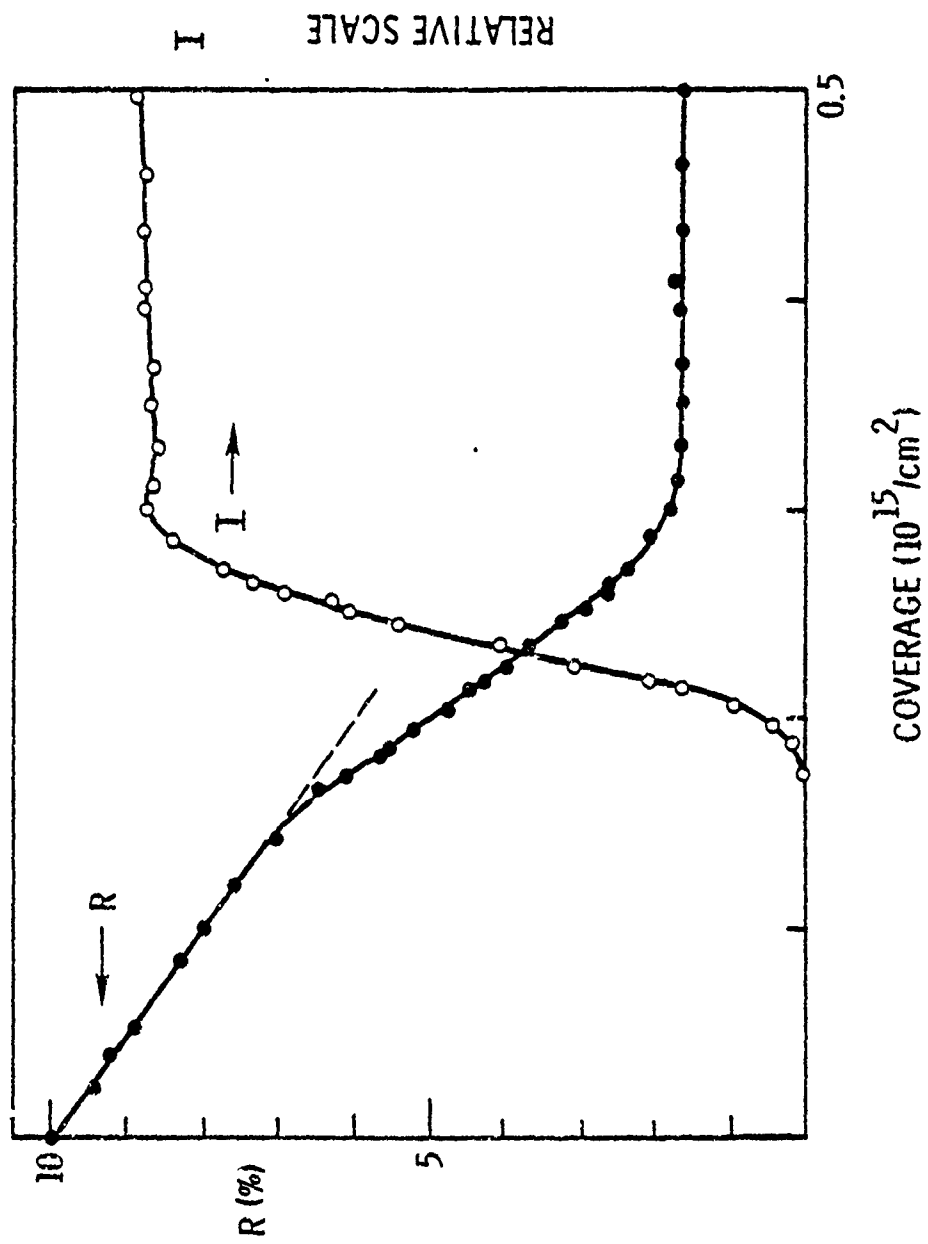


Figure 2. Variation of reflectance (R) and photoemission current (I) with Cs coverage. α was set equal to α_{ATR} for a fresh Ag-vacuum interface and the reflectance of a He-Ne laser light was measured during Cs deposition.

a result of a linear change in the \bar{K} of SPW with increasing Cs coverage. Interestingly, the slope of the R vs T curve changes abruptly at a coverage of about 1/3 monolayer. At the same coverage, the photoelectric threshold is also reached. If we assume that the sticky coefficient of Cs has not changed abruptly at $\sim 1/3$ monolayer coverage, then the abrupt change of the slope indicates a change in the properties of the Cs-Ag surface layer. Further investigation of the coverage dependence of R_{min} , using monochromatic light from a Hg lamp, shows that the coverage at which the abrupt change occurs increases with increasing wavelength of light. Because the photoemission current excited by the light is not strong enough for us to determine a clear photoelectric threshold, we could not directly correlate between the abrupt change of the slope and the threshold of photoemission. However, we know that the photoelectric threshold shifts to higher coverages at longer wavelengths at the initial stages of Cs deposition because the work function of the surface decreases with increasing Cs coverage. Therefore, we can speculate that the photoelectric effect is responsible for the abrupt change of the slope in R vs t . A probable reason for the change is that, beyond the photoelectric threshold, SPW can be damped by exciting electrons into the vacuum.

III. SPW STUDY OF THIN (30 Å - 500 Å) Ag FILMS

A. DETERMINATION OF DIELECTRIC CONSTANT AND THICKNESS OF METAL FILM

It is well known that the properties of SPW in a Kretschmann configuration depend on both the dielectric constant and the thickness of the metal film. The thickness dependence becomes significant when the thickness is comparable to or smaller than the penetration depth of the SPW in the metal. From these dependencies, we can deduce the dielectric constant at any given wavelength and the thickness of a metal film (d) from the resonant reflectance curve of the corresponding SPW.

We found that a least-squares fit of the R vs K_x data provides two sets of ϵ_1 and d solutions, one corresponding to undercoupling of a damped SPW, and the other corresponding to the overcoupling of a less damped SPW. With the help of a d determined at another frequency, these two sets of solutions can be distinguished.

Results of the data fitting are given in Fig. 3. The average deviation of R between the measured and theoretical values is about 2%. For the case of $\lambda = 6328 \text{ Å}$, two equally good fits are presented, one for $\epsilon_1 = -17.45 + i 0.92$ and $d = 387 \text{ Å}$, and one for $\epsilon_1 = -16.72 + i 1.66$ and $d = 483 \text{ Å}$. For 4358 Å , fits are presented for $\epsilon_1 = -5.25 + i 0.53$ and $d = 567 \text{ Å}$ and for $\epsilon_1 = -5.25 + i 0.32$ and $d = 467 \text{ Å}$.

Note that there are slight differences between the fits for the two sets of solutions. A measurement of R more accurate than $\pm 2\%$ may allow distinction between these two sets of values. However, the distinction can be easily achieved by comparing the resultant d 's. By comparing the thicknesses, we conclude that d is about 475 Å and the

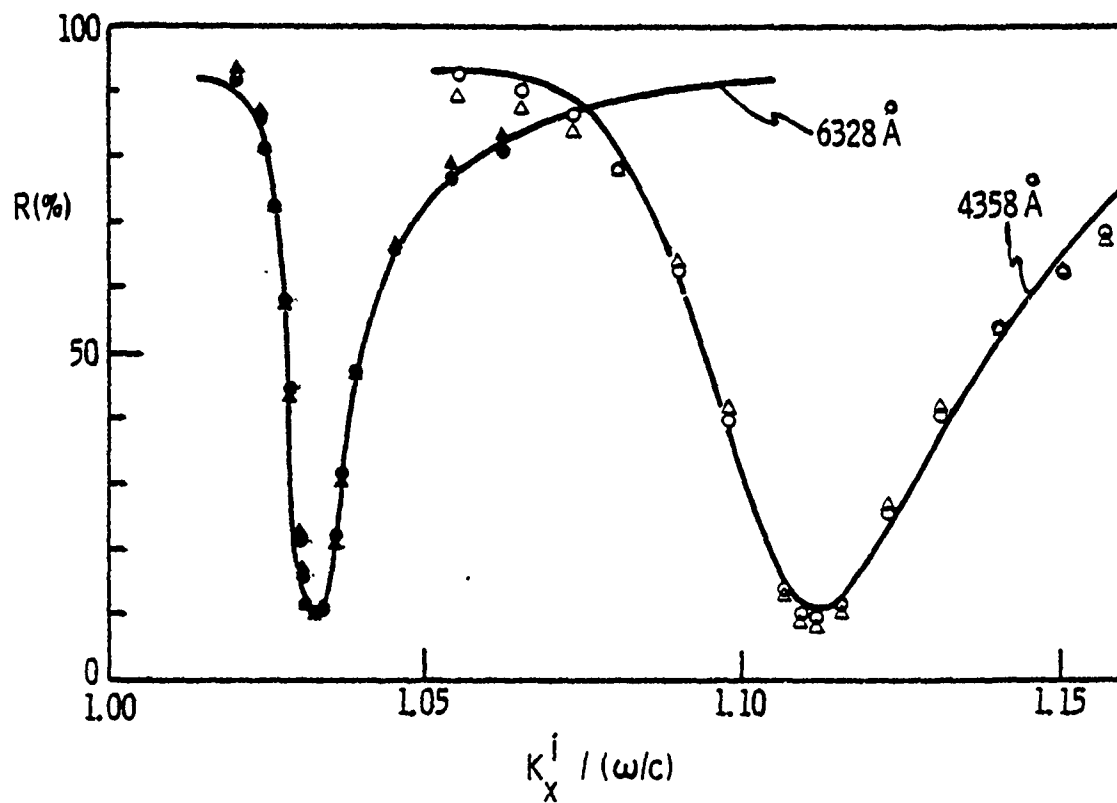


Figure 3. Data fitting of measured R versus $K_x^i / (\omega/c)$ curves at 6328 Å and 4358 Å. Solid curves are data. Calculated reflectances for each fitting are shown by the symbols \blacktriangle , \bullet , \triangle , and \circ . For \blacktriangle : $(t, \epsilon_1) = (387 \text{ \AA}, -17.45 + i 0.92)$, \bullet : $(483 \text{ \AA}, -16.72 + i 1.66)$, \triangle : $(567 \text{ \AA}, -5.25 + i 0.53)$, and \circ : $(467 \text{ \AA}, -5.25 + i 0.32)$.

dielectric constants are $\epsilon_1 = -16.72 + i 1.66$ at 6328 \AA and $\epsilon_1 = -5.25 + i 0.32$ at 4358 \AA . These values agree well with the known bulk constants of Ag:^{6,7} $\epsilon_1 = -16.32 + i 0.54$ at 6328 \AA and $\epsilon_1 = -5.19 + i 0.28$ at 4358 \AA .

The above procedure can be extended to fit the SPW reflectance minima at several (e.g., m) frequencies. The number of parameters to be fitted for a thickness d and m complex dielectric constants is $2m+1$. A least-squares fit can solve these parameters simultaneously without a pre-determined formula for the $\epsilon(\omega)$.

This fitting method is important for determining $\epsilon_1(\omega)$ of a metal film 100 \AA to 1000 \AA thick when the thickness cannot be known within an accuracy of $\pm 50 \text{ \AA}$. In this thickness range, the leakage loss and the Joule loss of SPW are comparable. The least-squares fit can also be applied to fit $R(\theta)$ curves for $d < 100 \text{ \AA}$. In this case, the angular dependence of EM fields in the metal film is primarily determined by ϵ_2 and n . Therefore, the relative angular dependence of reflectance (absorption is equal to $1-R$) does not show a significant dependence on ϵ_1 , and only the absolute value of reflectance is a function of the product of the absorption coefficient and the area density of electrons. Thus, the least-squares fit gives only the $d \times \epsilon_1''$ product, but not an accurate ϵ_1' or $\epsilon_1'd$. The correlation between d and ϵ_1'' cannot be eliminated by including more data at different ω , but it can be circumvented by a determination of d by other methods.

B. DEPENDENCE OF RESONANCE OF SPW ON FILM THICKNESS

We have studied the thickness dependence of SPW excitation in a prism-Ag-vacuum configuration, using TM-polarized light from a He-Ne laser and a Hg lamp. Ag films were evaporated on the prism under vacuum at 1×10^{-8} torr, and reflectance (R) versus cK/ω curves were measured in situ. Evaporation and the reflectance measurements were carried out alternatively. Assuming mass thickness t of the Ag film is proportional to the deposition time, we found that, with decreasing mass thickness, R_{\min} increases, the dip K_{ATR} shifts to large values of cK/ω , and the width ω of the R vs cK/ω curves broadens until $t \approx 250 \text{ \AA}$. With further reduction of t , R_{\min} at first decreases and then increases; K_{ATR} shifts somewhat; ω broadens at a faster rate. These findings are valid for all wavelengths used ($\lambda = 6328 \text{ \AA}$, 5780 \AA , 5461 \AA , 5358 \AA , and 4047 \AA). A typical set of data ($\lambda = 6328 \text{ \AA}$) is shown in Fig. 4a.

To check the t -dependence of the R vs cK/ω curves theoretically, we calculated these curves at $\lambda = 6328 \text{ \AA}$ for the above configuration in the same thickness range. In our calculation, $n = 1.52$ and $\epsilon_1 = -16 + i 0.52$ (ϵ_1 is assumed to be independent of t). The results are shown in Fig. 4b. The calculated curves show that, as t decreases 1) the dip shifts to larger cK/ω values, 2) the dip broadens, and 3) R_{\min} increases monotonically. A comparison between Figs. 4a and 4b indicates that the t -dependence of R vs cK/ω curves in Fig. 4a cannot be fully explained by the t -dependence of SPW for those curves where $t \underset{\sim}{<} 250 \text{ \AA}$, if we assume that $\epsilon_1(\omega)$ is independent of t . A least-squares fit of the R vs θ curves for $t \underset{\sim}{<} 250 \text{ \AA}$ shows that, for decreasing t 1) the derived

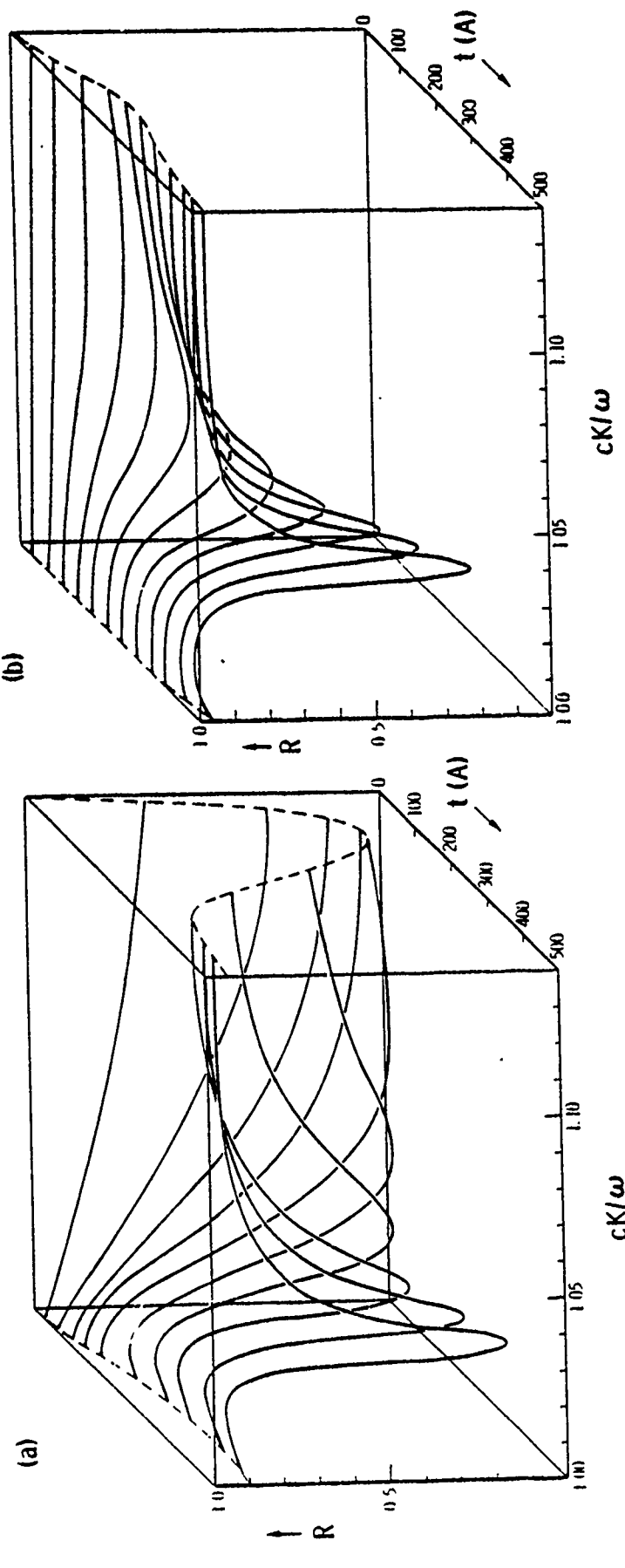


Figure 4. a) Data for the resonant reflectance R versus cK/ω curves of the SPW at the He-Ne laser frequency (6328 Å) in a prism-Ag-vacuum configuration for various Ag film thicknesses t . b) The corresponding calculated R versus cK/ω curves using $n = 1.52$ and a t -independent $\epsilon_1 = -16 + i 0.52$.

ϵ'_1 of Ag becomes less negative, 2) the derived ϵ'' increases dramatically, and 3) the derived d is almost constant ($d \approx 200 \text{ \AA}$), which suggests that the Ag films of $t < 250 \text{ \AA}$ are more likely to be island types, with an island height of $\sim 200 \text{ \AA}$. The increase of ϵ''_1 may play a role in the recently reported surface-enhanced-Raman scattering process.

IV. SPW ENHANCEMENT

A. SPW ENHANCED - PHOTOEMISSION

In other work under this contract, we have measured photoelectron emissions from the silver surface due to light excitation and the reflectance of the light as functions of the angle of incidence in the presence of a Cs overlayer with a coverage of 2.5×10^{14} atoms/cm². We found that the intensity curve showed a peak while the reflectance curve showed a dip. A typical example for light of 6328 Å is shown in Fig. 5. The intensity at the peak is about 100 times larger than that at the off-peak position. The absolute quantum yield was not established. Because the penetration depth of surface plasmons is different from the escape depth of photoelectrons in silver, the angular positions of the peak and dip differ -- by 0.05° for this case.

ATR-enhanced photoemission has been achieved directly with a commercial S-1 (Ag-O-Cs) photocathode by optically coupling a right-angle prism to the flat window of a RCA 7102 photomultiplier tube (Fig. 6). Photoemission current was measured as a function of wavelength (λ) and angle of incidence (θ) of incoming radiation. Since the Ag film of the photocathode was very thin and impure, strong ATR resonances were not obtained. Instead, the photoemission current exhibited a broad maximum at $\theta \approx 45^\circ$. Nevertheless, by measuring the photoemission currents at $\theta = 45^\circ$ with and without the coupling prism, we could detect the effect of ATR on photoemission. As shown in Fig. 7, the measured enhancement factor for TM waves (the ratio of photocurrents with and without a prism) increases from 1.5 at $\lambda = 1.3 \mu\text{m}$ to 2.5 at $\lambda = 0.45 \mu\text{m}$.

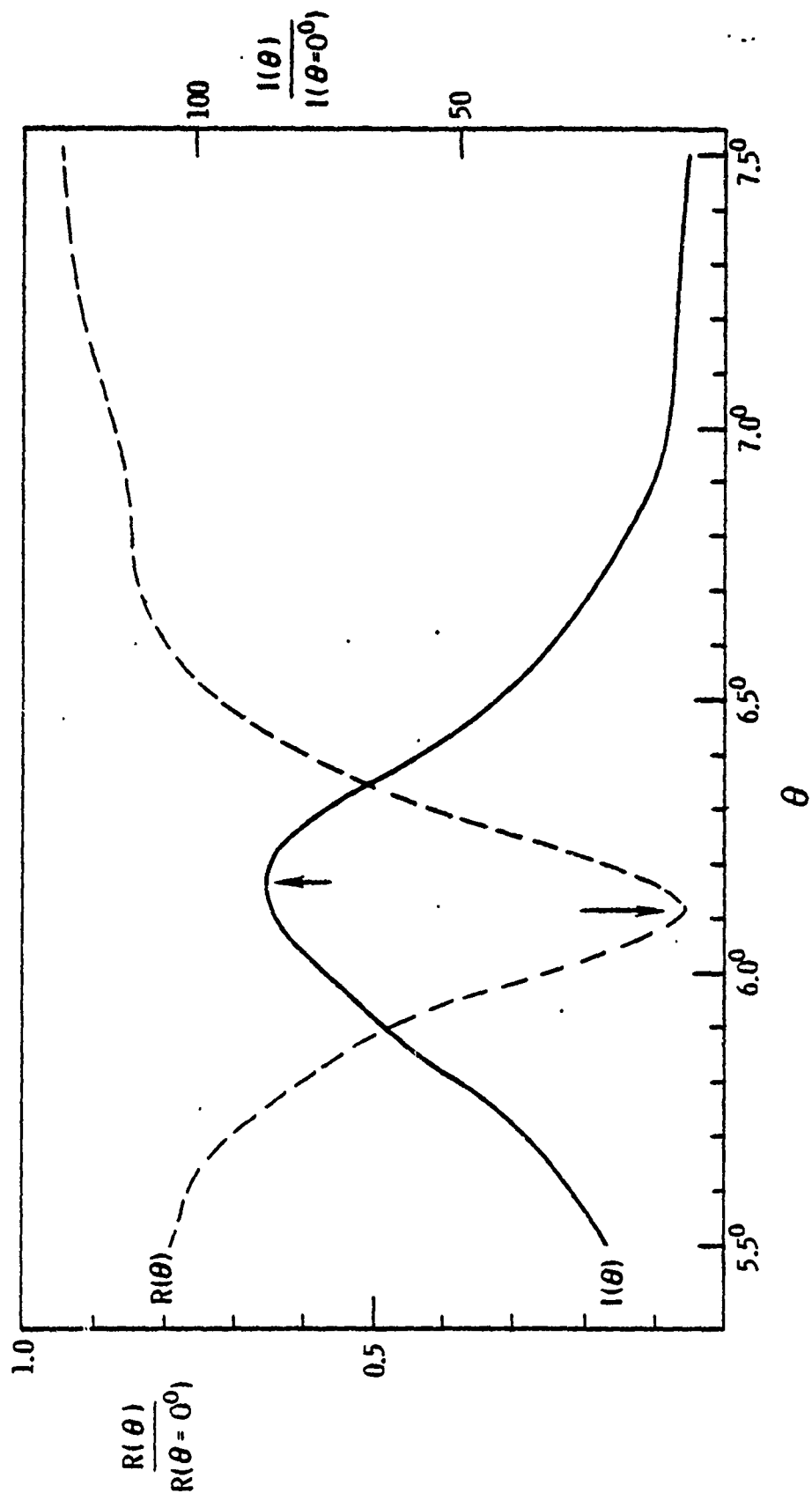


Figure 5. Variation of reflectance R with θ , and photoemission current I with θ at $\lambda = 6328 \text{ \AA}$. The angular positions of the peak of I and the dip of R differ by 0.05° .

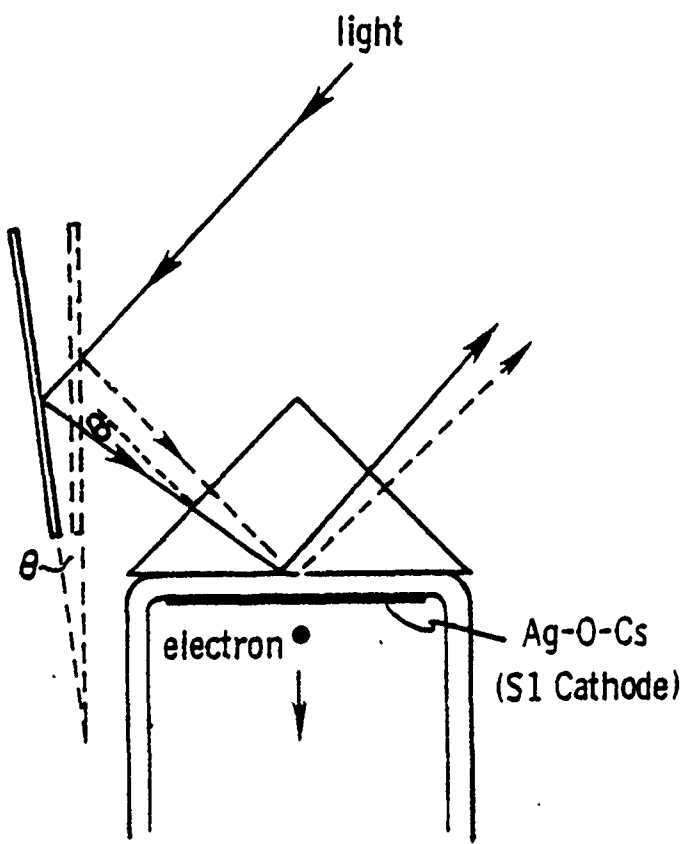


Figure 6. Experimental configuration for enhancement of photoemission from a commercial S-1 cathode.

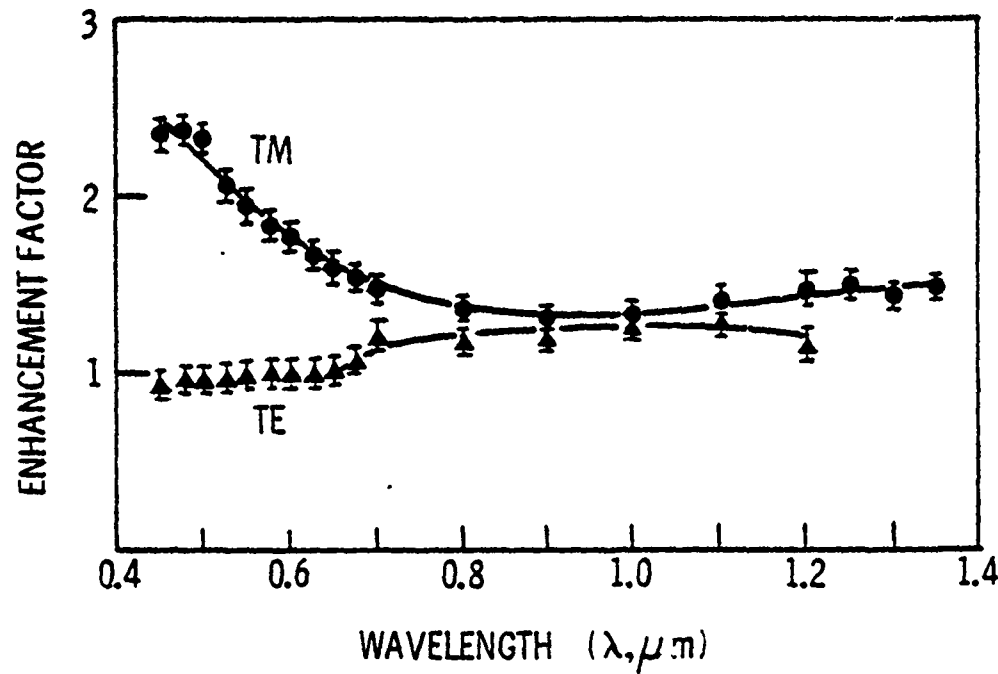


Figure 7. The enhancement factor (the ratio of photoemission currents with and without the prism) vs wavelength.

We believe that these results, as well as those reported by G. Hincelin and A. Septier⁸ -- who observed enhancement factors of 20-50 on evaporated Ag films -- suggest that a large enhancement factor can be expected by proper control of relevant parameters (e.g., Ag film thickness, film perfection, surface work function, etc.).

B. SPW-INDUCED COUPLING OF EM WAVES IN A Si-Au DIODE

When a metal film is deposited on a semiconductor surface, as in a diode, SPW exist at both the air-metal and the metal-semiconductor interfaces. The SPW can be coupled with the bulk electromagnetic wave by placing a prism close to the device. When a glass prism is placed above the Au surface with an air gap of several thousands Å (inset of Fig. 8), a visible light in the prism can couple with SPW at the air-Au interface. At coupling, the reflectance shows a minimum, as shown in Fig. 8 where $\lambda = 6328 \text{ \AA}$.

The coupled electromagnetic field, guided by the SPW, can extend into the Au-Si interface. When the photon energy is larger than the band gap of the semiconductor, as in our case, the EM field can create electron-hole pairs in the space-charge region, and a photovoltage V is developed. As shown in Fig. 8, a plot of V versus θ shows a local maximum where excitation of SPW occurs.

Furthermore, the SPW that propagate along the Au-Si interface of the diode can also be used to enhance the internal photoemission, in which electrons are injected from Au into Si. To study only the internal photoemission, SPW with photon energies between the band gap of Si and the Schottky barrier height should be used. For Au-Si (p-type) diodes, these

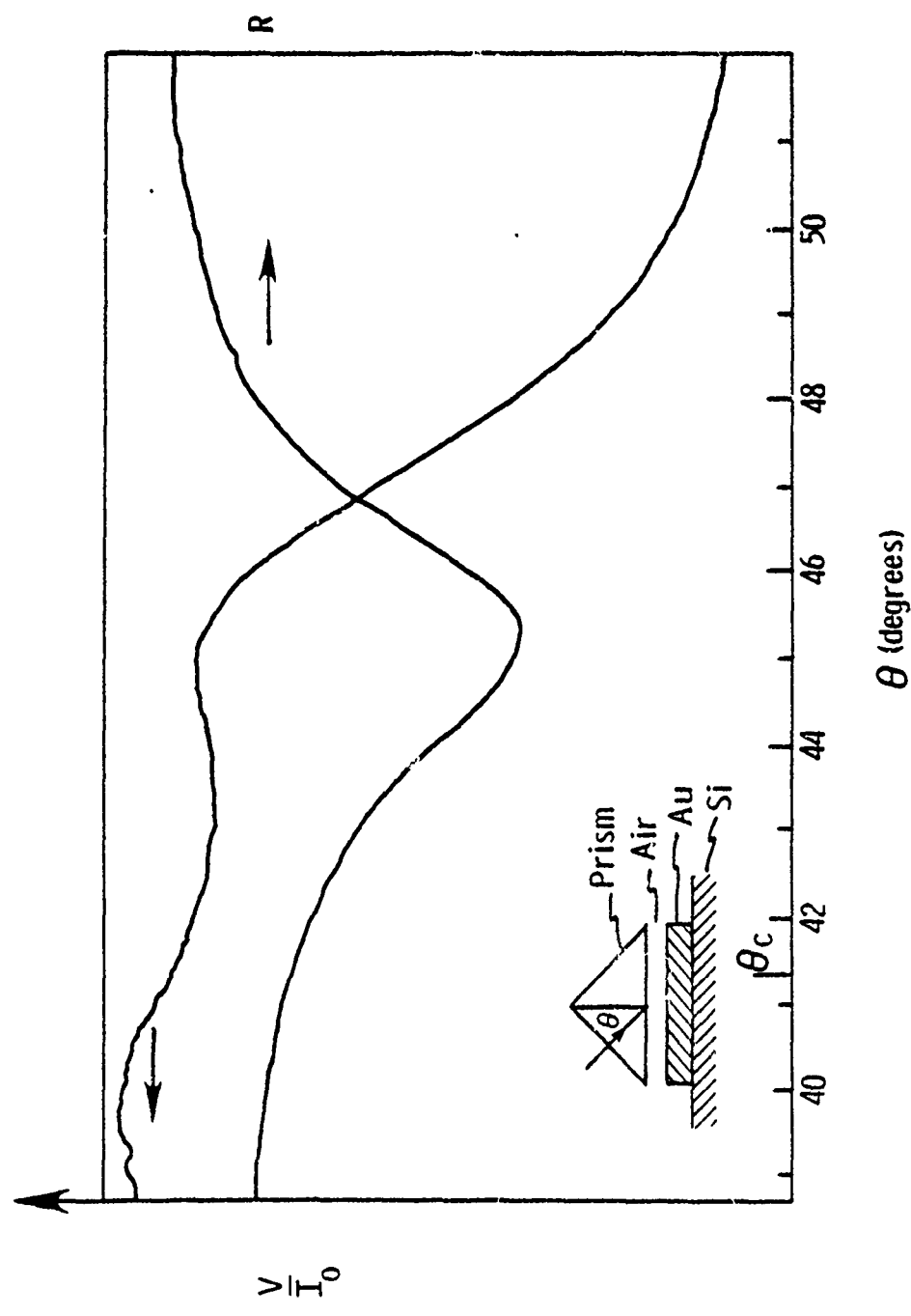


Figure 8. The reflectance minimum and the photovoltage maximum which occur at resonant coupling of SPW. The inset shows the Otto configuration.

energies correspond to infrared radiation of wavelengths from $\sim 1.1 \mu\text{m}$ to $3 \mu\text{m}$.

Our theoretical study showed that resonant coupling between SPW at the Au-Si interface and infrared radiation at $\lambda = 2 \mu\text{m}$ can be achieved by using a Ge prism and 1) a 61° incident angle, 2) a 450 \AA -thick Au film, and 3) no air gap between the Ge prism and the Au film. However, further analysis indicated that an air gap as small as 800 \AA can prohibit the coupling completely. In principle, filling the gap with a material with a high index of refraction can solve this problem, although we have not yet developed the technique. Our study also showed that the SPW at Au-Si interfaces can be coupled with a grating to bypass the matching problem.

V. BIBLIOGRAPHY

1. E. Burstein, W.P. Chen, Y.J. Chen, and A. Hartstein, *J. Vac. Sci. Technol.* 11, 1004 (1974).
2. A. Otto, *Z. Phys.* 216, 398 (1968).
3. E. Kretschmann, *Z. Phys.* 241, 313 (1971).
4. A. Otto, Proc. Taormina Conf. on Polaritons, eds., E. Burstein and F. DeMartini (Pergamon, New York, 1974) p. 117.
5. W.H. Weber, *Phy. Rev. Lett.* 39, 153 (1977).
6. L.G. Schulz, *J. Opt. Soc. Am.* 44, 357 (1954).
7. L.G. Schulz and F.R. Tangherlini, *J. Opt. Soc. Am.* 44, 362 (1954).
8. G. Hincelin and A. Septier, Proc. 7th Int. Vac. Congress and 3rd Int. Conf. Solid Surfaces (Vienna, 1977) p. 1269.

APPENDIX I

APPENDIX I

SURFACE PLASMA WAVE STUDY OF SUBMONOLAYER
Cs AND Cs-O COVERED Ag SURFACES *

W. P. Chen and J. M. Chen
Martin Marietta Laboratories
Baltimore, Maryland, 21227, U.S.A.

*Work supported by Army Research Office contract DAAG29-77-C-0036

ABSTRACT

We have carried out theoretical and experimental studies of surface plasma wave (SPW) on clean and submonolayer Cs and Cs-O covered Ag surfaces. An attenuated total reflection (ATR) technique was employed to study the resonant excitation of SPW with transverse magnetic (TM)-polarized light in the 4500\AA - 11000\AA wavelength region. The reflectance of TM light was measured as a function of incident angle at various wavelengths. The reflectance shows a minimum (R_{\min}) at an angle (θ_{ATR}) when the TM light couples resonantly with SPW. We found that a monolayer of Cs coverage causes a change in R_{\min} by as much as 10%, without causing any obvious shift of θ_{ATR} . On the other hand, with the presence of a Cs-O monolayer, we observed a shift of θ_{ATR} without appreciable change of R_{\min} . Analyzing the data with a theoretical model, we found that the Ag-Cs surface layer is strongly absorptive and the Ag-O-Cs surface layer is transparent, within the wavelength region of our study.

1. Introduction

Metal surfaces and their adsorbed layers have been interesting subjects of investigation for a long time. They have been investigated by using electrons, ions, UV-radiation and X-rays as probes. Recently, there has been a growing interest in visible and infrared light as surface probes. The conventional optical spectroscopy such as reflectance measurement suffers from two weaknesses. First, the sampling depth is of the order of 100 \AA , which is much larger than the thickness of a monolayer. Second, incident light and its reflection from a highly reflective metal surface form a node in the electric field at the location of the adsorbed layer. Consequently, the interaction between the adlayer and the electromagnetic (EM) field is largely reduced. However, the weak interaction between an adlayer and the EM field can be enhanced by using surface plasma waves (SPW) as a surface probe [1].

The SPW study of metal surfaces can be divided into two categories. One is the propagation technique in which SPW are launched and propagate on a metal surface. The propagation length can be as large as macroscopic distances [2,3] and leads to a long interaction duration between adlayer and surface plasma waves. This can enhance the sensitivity of the EM probe at metal surfaces. In the propagation technique, one observes overlayer-induced reduction of the propagation length which is measured as a reduction in re-radiation at a fixed distance away from the excitation region. The second study category is the attenuated total reflection (ATR) technique [4,5] by which surface plasma waves can be coupled resonantly with TM-polarized light. The resonance is a high Q phenomenon and results in high electric fields at

a metal surface [1,6]. Thus, its surface sensitivity is greater than with conventional optical techniques. Roughly 0.2% of a monolayer can be detected [7]. In the ATR technique, one observes overlayer-induced changes of the SPW resonance which are shown in the reflectance (R) vs. incident angle (θ) curve as a change of resonance angle, half width and reflectance minimum [8].

Theoretical studies show that the overlayer-induced changes are further enhanced when SPW of the metal substrate interact resonantly with dipole oscillations of the overlayer [9-12]. The spectra of the induced changes, therefore, can provide a spectroscopic tool to study dipole excitations in the overlayer. Both the propagation technique and the ATR technique have been used to study various kinds of overlayer-metal systems in the visible [7-8, 13-16] and infrared [9,17,18] areas. The published works [7-8, 15-18] on overlayers of thickness of the order of a monolayer are particularly interesting and reveal the power of the SPW technique as an optical probe of monolayers.

Among various overlayer-substrate systems, the problem of alkali adsorption on metals [19-22] remains one of the most studied chemisorption systems because of its many technological applications and relative ease of experimental control and theoretical analysis. Experimental information has been obtained mainly from several techniques: (1) LEED analyses involving determination of the periodic arrangement of the adatoms on the surfaces; (2) work-function measurements involving changes of surface potential barrier with adsorbate coverage; and (3) photoemission measurement involving energy distribution of emitted electrons. However, optical properties of the system are still not clear.

In this paper, we present our results of a SPW study of an Ag surface covered by a Cs or Cs-O submonolayer. The Kretschmann [5] ATR technique was used. From the adlayer-induced changes of resonance of SPW of the Ag-vacuum

interface, we have derived the optical properties of the submonolayer-covered Ag surface. We found that in the visible and the near infrared wavelength regions, the Cs-Ag surface layer is strongly absorptive and that the Cs-O-Ag surface layer is transparent.

2. Theory

2.1 Nature of Surface Plasma Waves

Surface plasma waves are EM waves which can propagate along a metal-vacuum interface, decreasing exponentially in amplitude with distance from the interface. Let us consider a case in which the metal is an optically isotropic homogeneous medium characterized by a dielectric constant $\epsilon_1(\omega)$ and magnetic permeability $\mu = 1$. For a model in which the interface is considered a sharp geometric boundary (Fig. 1a), the SPW of the metal-vacuum interface are TM-polarized and have a dispersion relation given by [4]:

$$K^2 = \frac{\epsilon_1(\omega) \epsilon_2}{\epsilon_1(\omega) + \epsilon_2} \frac{\omega^2}{c^2} , \quad K = \text{Re}(K) + i \text{Im}(K) \quad (1)$$

where K and ω are the wavevector and the frequency of the SPW respectively, and $\epsilon_2 = 1$ is the dielectric constant of vacuum.

Surface plasma waves exist in the frequency region in which $\epsilon_1'(\omega) < -1$, where $\epsilon_1(\omega) = \epsilon_1'(\omega) + i\epsilon_1''(\omega)$. This condition is satisfied for Ag in the visible. The wavevector of SPW is larger than the wavevector of light in vacuum, i.e., $\text{Re}(K) > \frac{\omega}{c}$. Therefore, SPW are nonradiative and cannot couple directly with light in vacuum. However, one can place a prism close to the metal-vacuum interface to form a prism-metal-vacuum Kretschmann configuration (Fig. 1b) to augment the wavevector. In this configuration, the metal is in the form of a thin film. When light is incident upon the prism-metal interface at angles θ larger than the critical angle θ_c , it can create an evanescent EM wave which has a proper parallel component of wavevector K_x^i to match with

the wavevector of SPW. Here $n > 1$ is the index of refraction of the prism and $\theta_c = \sin^{-1}(1/n)$. Therefore, SPW can couple directly with light in the prism.

When a metal-vacuum interface is examined on a microscopic scale, the model of a sharp geometric boundary for the interface is not exactly correct. The metal-vacuum interface is better described by a transition layer of atomic thickness at the metal surface [23]. The electronic states of the transition layer differ from the metal bulk states; and when atoms or molecules are adsorbed on the metal surface, the transition layer changes to a new form. Thus, the theoretical dispersion-relation of SPW of a metal-vacuum interface given by equation (1), which is based on a one-sharp-boundary model, should be modified. Although the modification to the dispersion-relation is usually small, the spectral dependence of the modification can reveal the change in optical property of the interface due to the presence of the adsorbed layer. The exact dispersion-relation of SPW of the metal-vacuum interface can be calculated only when the depth profile of the dielectric constant of the transition layer is known; and, even under those conditions, an exact analytical solution of the dispersion-relation can only be obtained for some special cases [24]. Here, we use a slab to model the transition layer and look for an approximate solution in general cases. We find that such a model calculation is satisfactory to describe the influence of the adlayer on the SPW of the metal-vacuum interface. The metal-vacuum interface then has a metal-slab-vacuum configuration (Fig.1c) with two sharp geometric boundaries. The slab which represents the transition layer has an effective thickness and an effective dielectric constant. The effective thickness, d_s , is chosen so that there is no contribution to the dielectric constants of

the adjacent bulk media from the surface states. Since there is no clear cut boundary of a transition layer, such a choice is somewhat arbitrary; however, we will show later that it is not critical in the present case. Because of the existence of surface electric fields and chemisorption bonds, the EM response of a transition layer in the direction normal to the interface is different from that in the parallel direction. Therefore, the effective dielectric constant of the slab is set to have two different components, one normal to the interface, $\epsilon_{\perp}(\omega)$, and the other parallel to the interface, $\epsilon_{\parallel}(\omega)$.

Furthermore, it is known that SPW in the Kretschmann configuration are perturbed by the prism [1,6], and that the interaction can change the dispersion relation of SPW. The perturbation can only be neglected in a weak coupling limit, i.e., in the case of a thick metal film. In order to take into account the perturbation due to the prism in the Kretschmann configuration, we extend our model to a four layer (prism-metal-slab-vacuum) configuration (Fig. 1d), where the slab again represents the transition layer. After applying Maxwell's equations and boundary conditions, the dispersion relation of surface plasma waves at the metal-vacuum interface in the four-layer configuration is given by:

$$\begin{aligned}
 & \left(\frac{K_{2Z}}{\epsilon_2} - \frac{K_{1Z}}{\epsilon_1} \right) - i \tan(K_{4Z}d_s) \left(\frac{K_{2Z} K_{1Z}}{K_{4Z}} \frac{\epsilon_{\parallel}}{\epsilon_1 \epsilon_2} - \frac{K_{4Z}}{\epsilon_{\parallel}} \right) + \\
 & \left[\left(\frac{K_{1Z}}{\epsilon_1} - \frac{K_{3Z}}{\epsilon_3} \right) / \left(\frac{K_{1Z}}{\epsilon_1} + \frac{K_{3Z}}{\epsilon_3} \right) \right] \exp(2iK_{1Z}d_1) \left[\left(\frac{K_{2Z}}{\epsilon_2} + \frac{K_{1Z}}{\epsilon_1} \right) + \right. \\
 & \left. i \tan(K_{4Z}d_s) \left(\frac{K_{2Z} K_{1Z}}{K_{4Z}} \frac{\epsilon_{\parallel}}{\epsilon_1 \epsilon_2} + \frac{K_{4Z}}{\epsilon_{\parallel}} \right) \right] = 0 \quad (2)
 \end{aligned}$$

with

$$K_{jZ} = (\epsilon_j \frac{\omega^2}{c^2} - K^2)^{1/2} \text{ for } j = 1, 2, 3$$

$$K_{4Z} = [\epsilon_{\parallel} \frac{\omega^2}{c^2} - \frac{K^2}{\epsilon_1}]^{1/2}$$

where K_{jZ} are the wavevector components perpendicular to the surface; $j = 1, 2, 3, 4$ labels the physical quantities of the metal, the vacuum, the prism and the slab, respectively; $\epsilon_3 = n^2$ is the dielectric constant of the prism; and d_1 is the thickness of the metal film.

In our experimental conditions we only need to consider those SPW which can couple directly with light in a prism. These SPW are damped by radiative and dielectric losses. The K_{jZ} of these SPW should have positive real parts here. There are many branches of complex ω vs. complex K solution to equation (2) for these damped SPW. Here we look for a real ω vs. complex K solution. When $\epsilon_{\parallel}(\omega) = \epsilon_1(\omega)$, (i.e., when the transition layer is assumed to be isotropic), the real ω vs. complex K solution given by equation (2) becomes the dispersion-relation of SPW derived by Pockrand [14] except some changes of sign.

For a thin slab with $|K_{4Z}d_5| \ll 1$ and a metal film with $|\exp[i2\pi d_1 K_{1Z}]| \ll 1$ at K given by eq. (1), an approximate expression (we followed closely the procedure of derivation given in references [5], [6] and [14]) of complex K of SPW as a function of ω can be given explicitly to first order in d_5/λ and $|\exp i2\pi d_1 K_{1Z}|$ by:

$$K = K^0 + K^R + K^T \quad (3)$$

with

$$K^0 = \left(\frac{\epsilon_1 \epsilon_2}{\epsilon_1 + \epsilon_2} \right)^{1/2} \frac{\omega}{c} \quad (4)$$

$$K^R = \frac{\omega}{c} \left[\frac{K_{1Z}\epsilon_3 - K_{3Z}\epsilon_1}{K_{1Z}\epsilon_3 + K_{3Z}\epsilon_1} \right]_{\approx K^0} \left(\frac{2}{\epsilon_1 - \epsilon_2} \right) \left(\frac{\epsilon_1 \epsilon_2}{\epsilon_1 + \epsilon_2} \right)^{3/2} \exp \left[i \frac{4\pi d_1}{\lambda} \frac{\epsilon_1}{(\epsilon_1 + \epsilon_2)^{1/2}} \right] \quad (5)$$

$$K^T = i \left(\frac{2\pi d_s}{\lambda} \right) \left(\frac{\omega}{c} \right) \left(\frac{\epsilon_1 \epsilon_2}{\epsilon_1 + \epsilon_2} \right)^2 \frac{1}{(\epsilon_1 \epsilon_2)^{1/2} (\epsilon_2 - \epsilon_1)} \left(\epsilon_{\parallel\parallel} + \frac{\epsilon_1 \epsilon_2}{\epsilon_{\perp\perp}} - \epsilon_1 - \epsilon_2 \right) \quad (6)$$

where $\lambda = \frac{2\pi c}{\omega}$ is the wavelength of light in vacuum.

Equation (3) is the new dispersion relation, and equation (4) just repeats equation (1) and gives the dispersion relation of SPW of a metal-vacuum interface in a one-sharp-boundary model. K^R , which decreases exponentially with increasing metal thickness, gives the perturbation to equation (1) of SPW due to the prism [5]. K^T , which is proportional to the thickness of the slab, gives the modification to equation (1) of SPW due to the transition layer [14] and is very sensitive to the interface condition. Since we are particularly interested in the interface, we will concentrate on K^T in the discussion below.

When the transition layer changes in the presence of an adsorbed layer, its EM response changes accordingly. Let $\Delta\chi_{\perp}$ and $\Delta\chi_{\parallel\parallel}$ represent the adlayer-induced changes of electric susceptibility per adatom in the normal and the parallel directions respectively, and N_s represent the surface density of the adatoms. The changes of dielectric constants per unit area in $\epsilon_{\parallel\parallel}$ and $\epsilon_{\perp\perp}$ are $4\pi N_s \Delta\chi_{\parallel\parallel}$ and $4\pi N_s \Delta\chi_{\perp\perp}$ respectively. In our slab model, we can keep the effective thickness d_s unchanged for the new transition layer and have $\epsilon_{\parallel\parallel}^N = \epsilon_{\parallel\parallel} + 4\pi N_s \Delta\chi_{\parallel\parallel} / d_s$ and $\epsilon_{\perp\perp}^N = \epsilon_{\perp\perp} + 4\pi N_s \Delta\chi_{\perp\perp} / d_s$, to represent the new effective dielectric components.

The change in SPW dispersion-relation due to the presence of an adlayer can be expressed as a change of K^T . With ϵ_{\parallel}^N and ϵ_{\perp}^N given above, ΔK^T (the change in K^T) can be expressed as:

$$\Delta K^T = i \left(\frac{2\pi}{\lambda} \right) \left(\frac{\omega}{c} \right) \frac{1}{(\epsilon_2 - \epsilon_1)(\epsilon_1 \epsilon_2)^{1/2}} \left(\frac{\epsilon_1 \epsilon_2}{\epsilon_1 + \epsilon_2} \right)^2 \left[(\epsilon_{\parallel}^N - \epsilon_{\parallel}) - \frac{\epsilon_1 \epsilon_2}{\epsilon_{\perp}^N \epsilon_{\perp}} (\epsilon_{\perp}^N - \epsilon_{\perp}) \right] d_s \quad (7)$$

$$= i \left(\frac{2\pi}{\lambda} \right) \left(\frac{\omega}{c} \right) \frac{1}{(\epsilon_2 - \epsilon_1)(\epsilon_1 \epsilon_2)^{1/2}} \left(\frac{\epsilon_1 \epsilon_2}{\epsilon_1 + \epsilon_2} \right)^2 [\Delta \chi_{\parallel} - \frac{\epsilon_1 \epsilon_2}{\epsilon_{\perp}^N \epsilon_{\perp}} \Delta \chi_{\perp}] 4\pi N_s \quad (8)$$

If the adlayer does not introduce new dipole transition in the transition layer so that ϵ_{\perp}^N does not deviate appreciably from ϵ_{\perp} , i.e., $|\epsilon_{\perp}^N - \epsilon_{\perp}| \ll \epsilon_{\perp}$, then ϵ_{\perp}^N in equation (8) can be replaced by ϵ_{\perp} . Then, the change ΔK^T is proportional to the total surface density of the adatoms and does not depend on the somewhat arbitrarily chosen quantity d_s . Otherwise, a microscopic calculation is required to determine ϵ_{\perp}^N and ΔK^T .

2.2 Coupling of SPW — ATR Method

Let us consider that a TM light is incident upon the prism-metal interface as shown in Fig. 1d. When the light is incident at an angle θ larger than the critical angle θ_c , it can couple directly with SPW of the metal-vacuum interface. The coupling takes place when ω and $K_x^i(\theta)$ of the incident light match with ω and K of the SPW. Here $K_x^i(\theta)$ is the component of the incident wavevector parallel to the interface. Since K_x^i is real and K is complex, an exact match between K_x^i is impossible. However, a close match can be reached at $K_x^i(\theta) = \text{Re}(K)$. When ω is fixed and θ is scanned, $K_x^i(\theta) = \text{Re}(K)$ occurs at $\theta = \sin^{-1} \left(\frac{\text{Re}(K)c}{n\omega} \right)$ which is designated θ_{ATR} .

When a TM light is incident at an angle close to θ_{ATR} , the incident light is strongly absorbed and the total reflection is attenuated. The reflectance R of the TM light can be approximately expressed as a function of θ as [5,6,14]

$$R(\theta) = 1 - \frac{4 [Im(K^0) + Im(K^T)] Im(K^R)}{[K_X^i - Re(K)]^2 + Im(K)^2} \quad (9)$$

Here, K , K^0 , K^T , and K^R are given in equations (3)-(6). The property of $R(\theta)$ has already been discussed in refs. [5], [6], and [14]. We summarize their results in the following for later discussion. The reflectance has a Lorentz dip at θ_{ATR} with a half-width W_θ (when $|Im(K)| \ll |Re(K)|$) and a minimum reflectance R_{min} given by

$$W_\theta = \frac{2Im(K)c}{n\omega\cos(\theta_{ATR})} \quad (10)$$

and $R_{min} = 1 - \frac{4n}{(1+n)^2} \quad (11)$

where $n = [Im(K^0) + Im(K^T)]/Im(K^R) \quad (12)$

Since $|Im(K^T)| \ll |Im(K^0)|$, $n \approx Im(K^0)/Im(K^R)$. By substituting ϵ_1 , ϵ_2 , and ϵ_3 [25] into equations (4) and (5), one can obtain K^0 and K^R , respectively, and n can be estimated at any d_1 . For a metal like Ag, the n vs d_1 curve is schematically plotted in Figure 2. At a particular metal thickness d_{opt} [6], n is equal to 1. R_{min} decreases as d_1 increases until d_1 reaches d_{opt} , at which point R_{min} reaches its minimum value ($R_{min} = 0$); as d_1 increases further, R_{min} increases to 100% at large film thicknesses [6].

When the transition layer of a metal-vacuum interface is transformed into a new transition layer in the presence of an adlayer, the resonant angle θ_{ATR} , the half width W_θ , and the R_{min} change by an amount $\Delta\theta_{ATR}$, ΔW_θ and ΔR_{min} respectively, where $\Delta\theta_{ATR}$, ΔW_θ and ΔR_{min} are given, to first order in ΔK^T , by:

$$\Delta\theta_{ATR} = \frac{c}{n\omega \cos(\theta_{ATR})} \operatorname{Re}(\Delta K^T) \quad (13)$$

$$\Delta W_\theta = \frac{2c}{n\omega \cos(\theta_{ATR})} \operatorname{Im}(\Delta K^T) \quad (14)$$

$$\Delta R_{min} = \frac{4\Delta n}{(n^2-1)} R_{min} \quad (15)$$

$$\text{with } \Delta n = \operatorname{Im}(\Delta K^T) / \operatorname{Im}(K^R) \quad (16)$$

Here $\Delta\theta_{ATR}$, ΔW_θ and ΔR_{min} are all proportional to ΔK^T and, therefore, proportional to the surface density of the adatoms, N_s ; and ΔW_θ and ΔR_{min} are correlated. Since n can be adjusted by varying the metal film thickness d_1 , ΔR_{min} depends not only on $\operatorname{Im}(\Delta K^T)$, i.e., on N_s , but also on the selected metal film thickness. In the case of $d_1 > d_{opt}$ (i.e., $n > 1$) a positive $\operatorname{Im}(\Delta K^T)$ (i.e., $\Delta n > 0$) will increase the R_{min} (less absorption) and vice versa for a negative $\operatorname{Im}(\Delta K^T)$. When $d_1 < d_{opt}$ (i.e., $n < 1$), a positive $\operatorname{Im}(\Delta K^T)$ will decrease the R_{min} (more absorption) and vice versa for a negative $\operatorname{Im}(\Delta K^T)$. The relative change $\frac{\Delta R_{min}}{R_{min}}$ approach infinity at $n = 1$, according to equations (11) and (15). Therefore, if the absolute value of R_{min} is not limited by a background noise, $d_1 \approx d_{opt}$ is the best condition for studying the effects of adsorbed monolayer on R_{min} . In the present experiment, we use $d_1 \approx 500 \text{ \AA}$, which is close to d_{opt} for exciting SPW of a silver surface in the frequency region of our study.

3. Experiment

The ATR experiments are carried out in a metal ultra-high vacuum system (Fig. 3a) at a background pressure of 1×10^{-9} torr. Inside the vacuum chamber, a right angle prism is mounted to the shaft of a high precision manipulator. A special ATR prism arrangement (Fig. 3b), introduced by Bösenberg [26], was used. One of the small faces of the prism is used to prepare a prism-Ag-adlayer-vacuum ATR configuration. A TM-polarized, monochromatic and collimated light beam is incident upon the large face of the prism at an angle α , (with a precision of 0.01°) and on the sample face at an angle θ . Here θ is related to α by

$$\theta = 45^\circ - \sin^{-1}\left(\frac{\sin(\alpha)}{n}\right). \quad (17)$$

The light beam is then reflected and leaves the prism anti-parallel to the incident light beam. By measuring the return beam intensity with a photodiode, we can determine the reflectance R as a function of angle α . Also an electron collector is placed close to the sample face to measure photoelectrons excited by the light beam in the ATR configuration.

The light beam used in the experiment is provided by a modified monochromator using a tungsten lamp source having an average bandwidth of 20 \AA in wavelength. The spread in angle of collimation is limited by diffraction of the output slit of the monochromator, and its average value is about $\pm 0.013^\circ$ from its central direction. Polarization of the light beam is achieved by using a Glan-type prism polarizer with an extinction ratio $< 1 \times 10^{-5}$.

In addition to the tungsten lamp, a He-Ne laser beam is used to track the light path, and also to monitor the Cs-adsorption and the oxidation of the Cs-Ag surface via photoemission.

The Cs-Ag surface is prepared as follows: First, a silver film (500 \pm 50 \AA in thickness) is deposited on the "sample" face of the prism at a pressure of 1×10^{-8} torr and at an evaporation rate of 1\AA/sec ; then Cs is deposited on top of the silver film by using an atomic beam source [27]. The Cs coverage is monitored by the photoemission current emitted from the Cs-Ag surface when excited by the He-Ne laser beam. Reflectance $R(\lambda)$ curves are measured at various wavelengths before and after the adsorption of the Cs layer.

It has been known for some time that as alkali metal atoms are adsorbed onto the surface of a metal such as W, Ni, and Ag, the work function lowers rapidly from its initial value. With continued adsorption the work function reaches a minimum, and then rises to approximately the bulk work function of the alkali metal at the completion of the first full layer coverage. The coverage dependence of the work-function lowering is only weakly dependent on the substrate material and their surface orientation. The work-function minimum occurs at Cs densities ranging from 2.2 to 2.6×10^{14} atoms/ cm^2 [19,28,29]. On the other hand, the photoelectron current reaches a maximum at work function minimum, then levels to a constant value at the first full layer coverage [28]. As an example, the work function minimum for Cs adsorption on W(100) surface occurs at $\sim 2.6 \times 10^{14}$ atoms/ cm^2 coverage and the photoelectron-current maximum occurs at $\sim 2.7 \times 10^{14}$ atoms/ cm^2 coverage [28].

In our experiment, a He-Ne laser light is incident at θ_{ATR} to resonantly excite SPW at the vacuum-Ag interface. This resonant excitation enhances the electric fields inside the Ag film and at the metal surface, thus enhancing the photoemission yield.

Our experimental results show that α_{ATR} , and, therefore, θ_{ATR} , do not change with increasing Cs coverage, and the absorptance ($1-R$) at α_{ATR} changes by about 8% (from 90% before Cs deposition to 98% at one full layer of Cs atom coverage). Thus, the photoemission yield of our present measurement represents approximately the relative quantum efficiency of the Cs-Ag surface, and the conventional relationship among photoemission yield, work function and Cs coverage holds [28]. The measured photoemission yield of the Cs-Ag surface is plotted as a function of deposition time t in Figure 4. The photoemission yield becomes detectable at $t \approx 33$ min when the work function of the Cs-Ag surface is lowered to approximately the photon energy (1.96 eV) of the He-Ne laser beam and increases dramatically with continued Cs adsorption until it reaches a saturated value at $t \approx 60$ min. Further adsorption first decreases the photoelectron yield slightly, then increases it at a very slow rate. This result indicates that the work function minimum occurs at $t \approx 60$ min at which point we set the Cs coverage $\approx 2.5 \times 10^{14}$ atoms/cm². This coverage is used as a basis throughout this paper. The Cs coverage is thus about 1.4×10^{14} atoms/cm² after 33 min of deposition when photoemission becomes detectable.

After the experiments are carried out on the Cs-Ag surface, pure O₂ gas is admitted into the chamber at $2-4 \times 10^{-8}$ torr for 2 to 3 minutes to form the Cs-O-Ag surface. In contrast with the Cs adsorption, α_{ATR} changes during the O₂ admission and the reflectance at α_{ATR} decreases monotonically back to its original value before Cs deposition. On the other hand, the

photoemission yield drops monotonically until it is no longer detectable. The completion of the oxidation is indicated by the completion of changes in α_{ATR} , reflectance and the photoemission yield. Reflectance $R(\alpha)$ curves at various wavelengths are measured again after the completion of oxidation.

4. Results

Typical experimental $R(\alpha)$ curves are shown in Fig. 5 for the frequencies indicated. The curves are for cases of a silver-vacuum interface without any overlayer, with a Cs submonolayer and with a Cs-O submonolayer respectively. The Cs coverage is 2.5×10^{14} atoms/cm².

The reflectance is normalized to the reflectance at α_c . Since the scanning range in θ is small and $R(\theta_c) \approx 1$, the normalized R is approximately equal to the reflectance $R(\theta)$ of the prism-Ag-submonolayer-vacuum multilayer system. The reflectance curves exhibit minima which indicate the excitation of SPW at the Ag-vacuum interface. We designate the angular position of the minima α_{ATR} , the half width W_θ and the reflectance R_{\min} respectively. The θ_{ATR} can be obtained by substituting α_{ATR} into equation (17). The W_θ can be obtained by the relation:

$$W_\theta = W_\alpha \cos(\alpha_{\text{ATR}}) / (n^2 - \sin^2(\alpha_{\text{ATR}}))^{1/2}. \quad (18)$$

Here the index of refraction of the prism, n , can be obtained by substituting the experimentally determined α_c into the following equation:

$$n = 2^{1/2} (\sin^2(\alpha_c) + 2^{1/2} \sin(\alpha_c) + 1)^{1/2} \quad (19)$$

where α_c is given in figure 6a.

A comparison of the $R(\alpha)$ curves for the different cases in Fig. 5 shows that the $R(\alpha)$ curves for the case with a Cs submonolayer have broader half-widths, lower values of R_{\min} and have no obvious change of α_{ATR} ; while the $R(\alpha)$ curves for the case with a Cs-O submonolayer have no obvious changes of half-widths and R_{\min} , but have an appreciable change of α_{ATR} .

From the $R(\alpha)$ curves at various frequencies, we derive the frequency-dependence of α_{ATR} , W_α and R_{\min} as shown in figures 6a, 6b, and 6c respectively.

In fig. 6a, α_{ATR} occur at angles smaller than α_c and decrease with increasing frequency. As derived from α_{ATR} and n , $\text{Re}(K)$ of the SPW has values larger than ω/c and increases with increasing frequency. This agrees with the theoretical dispersion relation given by equation (3). The detailed change of α_{ATR} due to Cs and Cs-O₂ deposition is plotted in an expanded scale in Fig. 7. The O₂ admission after the Cs adsorption causes a change of α_{ATR} from 0° at $\omega = 0.9 \times 10^4 \text{ cm}^{-1}$ to -0.4° at $\omega = 2.2 \times 10^{14} \text{ cm}^{-1}$. The change corresponds to a shift of $\text{Re}(K)$ toward large values. In Figure 6b we see that W_α increases with increasing frequency. The broadening reflects an increase of $\text{Im}(K)$ of SPW, again in agreement with equation (3). Although the broadening due to Cs adsorption is noticeable at high frequencies, the change is within the uncertainty of our measurement. Therefore, the change in $\text{Im}(K)$ of SPW due to Cs adsorption cannot be discerned. However, $\text{Im}(\Delta K^T)$ can be derived from the change of R_{\min} as will be discussed in the next section. Because the selected thickness of the Ag film favors the coupling of SPW with the incident light beams at high frequencies, R_{\min} decreases with increasing frequency as shown in Fig. 6c. With Cs adsorption, R_{\min} is reduced over the whole frequency region with a maximum reduction of 10% at $\omega = 1.7 \times 10^4 \text{ cm}^{-1}$.

It should be pointed out that the frequency dependences of α_{ATR} , W_α and R_{min} do not show any characteristic structure which can be associated with sharp dipole excitations of either the Cs-Ag or the Cs-O-Ag system. This is also verified by the measurement of the reflectance, R , as functions of frequency at some fixed angles, α , as shown in Figure 8. Thus, the theoretical slab model we discussed in the previous section, which assumes no sharp dipole transitions, is applicable to analyze the ATR data.

5. Discussion

We use the four layer model discussed in the previous section to derive the change of the complex wavevector ΔK^T of SPW from our data. We transformed all the values in α into those in θ by using equations (17) and (18) and determined n from α_c given in Figure 6a and equation (19). $\text{Re}(\Delta K^T)$ is obtained by substituting θ_{ATR} , $\Delta\theta_{\text{ATR}}$ and n into equation (13). $\text{Im}(\Delta K^T)$ is obtained as follows. At first we determine $\text{Im}(K)$, which is equal to $\text{Im}(K^0) + \text{Im}(K^R) + \text{Im}(K^T)$, with a 10% uncertainty by substituting θ_{ATR} , W_θ and n into equation (10). Then we determine n , which is equal to $(\text{Im}(K^0) + \text{Im}(K^T))/\text{Im}(K^R)$, much more accurately by substituting R_{\min} into equation (11). With $\text{Im}(K)$ and n determined, we can estimate $\text{Im}(K^R)$ with a 10% uncertainty. Then $\text{Im}(\Delta K^T)$ is determined with a 10% uncertainty by substituting R_{\min} , ΔR_{\min} , n and $\text{Im}(K^R)$ in equations (15) and (16). The frequency dependence of $\text{Re}(\Delta K^T)$ and $\text{Im}(\Delta K^T)$ are shown in Figures 9(a) and (b), respectively.

For the Cs-Ag system, the surface plasma waves have no obvious shift in phase wavevectors, but are damped appreciably. $\text{Im}(\Delta K^T)$ increases from ~ 0 to $1.3 \times 10^{-3} \frac{\omega}{c}$ with increasing frequency. The magnitude of $\text{Im}(\Delta K^T)$ is about 10% of the $\text{Im}(K)$ for the SPW of the Ag-vacuum interface. Therefore, the adlayers influences R_{\min} appreciably. Since the thickness d_1 of the Ag film is chosen to be less than d_{opt} , R_{\min} decreases in the presence of the Cs overlayer. Hincelin and Septier [30] have also investigated SPW for a Cs-Ag system at $d_1 \approx 600 \text{ \AA} > d_{\text{opt}}$ and found that R_{\min} increases with Cs adsorption. This dependence of R_{\min} on Cs adsorption and d_1 agrees with the theoretical prediction of the four layer model, showing that the model, which we use to study the interaction between a monolayer and macroscopic surface plasma waves, is at least qualitatively satisfactory.

The values of $\chi_a = (\Delta\chi_{||} + \frac{\epsilon_1 \epsilon_2}{\epsilon_1 \epsilon_1 N} \Delta\chi_{\perp})$ derived from the data and eq. (8) are predominantly imaginary with an uncertainty of $\sim 20\%$ due to the uncertainties of $\text{Im}(\Delta K^T)$ and the Cs coverage. Their real parts are less than $7 \times 10^{-24} \text{ cm}^3/\text{atom}$; their imaginary parts are between 0.2×10^{-22} to $1.4 \times 10^{-22} \text{ cm}^3/\text{atom}$. The large imaginary nature of χ_a indicates that the transition layer of the Cs-Ag surface is strongly absorptive.

For the Cs-O-Ag system, the result is completely different. The phase wavevector change of the SPW increases from ~ 0 to $5 \times 10^{-3} \frac{\omega}{c}$ with increasing frequency. The damping introduced by the overlayer is negligible. Therefore, the overlayer plays no role in the determination of R_{\min} , as observed. The values χ_a derived are predominantly real with a $\sim 10\%$ uncertainty due to the uncertainty of Cs coverage. Their real part decreases from 5.6×10^{-22} to $1.1 \times 10^{-22} \text{ cm}^3/\text{atom}$ with increasing frequency, and their imaginary part is about 0.05 of their real part. The real nature of χ_a indicates that the resultant transition layer of the Cs-O-Ag surface is transparent.

6. Conclusions

We have made theoretical and experimental studies of the surface plasma waves of Ag under the influences of a Cs and Cs-O submonolayer in the frequency region $0.9 \times 10^4 \text{ cm}^{-1} < \omega < 2.2 \times 10^4 \text{ cm}^{-1}$. In the Cs-Ag system, surface plasma waves are heavily damped with no obvious shift in the phase wavevector, while in the Cs-O-Ag system, they have shifts in their phase wavevectors without any obvious damping. By using a uniaxial slab to model the transition layer, which includes the overlayer and the very top surface layer of Ag, we conclude that: (1) the Cs-Ag system has a strongly absorptive transition layer, (2) the Cs-O-Ag system has a transparent transition layer, and (3) the four layer model qualitatively predicts the effect of a monolayer on SPW.

7. Acknowledgements

The authors wish to thank Dr. N. Byer, Dr. C. S. Wang and Dr. T. S. Sun for their aid in setting up the experiment and Professor E. Burstein for valuable discussions.

REFERENCES

1. E. Burstein, W.P. Chen, Y. J. Chen and A. Hartstein, J. Vac. Sci. Technol. 11 (1974) 1004.
2. J. Schoenwald and E. Burstein, Proc. Taormina Conf. on Polaritons, Eds. E. Burstein and F. DeMartini (Pergamon, New York, 1974) p. 139. J. Schoenwald, E. Burstein and J. M. Elson, Solid State Commun. 12 (1973) 185; D. L. Begley, D. A. Bryan, R. W. Alexander, R. J. Bell and C. A. Goben, Surface Sci. 60 (1976) 99; D. A. Bryan, D. L. Begley, K. Bhasin, R. W. Alexander, R. J. Bell and R. Gerson, Surface Sci. 57 (1976) 53.
3. W. P. Chen, G. Ritchie and E. Burstein, Phy. Rev. Lett. 37 (1976) 993.
4. A. Otto, Z. Physik 216 (1968) 398.
5. E. Kretschmann, Z. Physik 241 (1971) 313.
6. A. Otto, Proc. Taormina Conf. on Polaritons (Pergamon, New York, 1974) p. 117.
7. W. H. Weber, Phy. Rev. Lett. 39 (1977) 153.
8. F. Abeles and T. Lopez-Rios, Proc. Taormina Conf. on Polaritons (1974) p. 241.
9. W. P. Chen, Thesis, U. of Penna., Chapter VII (1977); W. P. Chen, A. Hjortsberg and E. Burstein, to be published.
10. C. A. Ward, R. W. Alexander and R. J. Bell, Phys. Rev. B 12 (1975) 3293.
11. V. M. Agranovich and A. G. Malshukov, Optics Commun. 11 (1974) 169.
12. T. Lopez-Rios, Optics Commun. 17 (1976) 342.
13. T. Lopez-Rios and G. Vuye, IL NUOVA CIMENTO 89B (1977) 823.
14. I. Pockrand, Surface Sci. 72 (1978) 577.
15. I. Pockrand, J. D. Swalen, J. G. Gordon II and M. R. Philpott, Surface Sci. 74 (1978) 237.
16. I. Pockrand, J.D. Swalon, J.G. Gordon II and M.R. Philpott, J. Chem. Phys. 70(7) (1979) 3401.
17. K. Bhasin, D. Bryan, R.W. Alexander and R.J. Bell, J. Chem. Phy. 64 (1976) 5019.

18. A. Hjortsberg, W. P. Chen and E. Burstein, Optics Commun. 25 (1978) 65.
19. C. A. Papageorgopoulos and J. M. Chen, Surface Sci. 39 (1973) 283;
20. R. Gomer, Solid State Phys. 30 (1975) 93; and references therein.
21. K. F. Wojciechowski, Surface Sci. 55 (1976) 246.
22. S. Anderson and V. Jostell, Surface Sci. 46 (1974) 625.
23. N. D. Lang, Phys. Rev. B4 (1971) 4234; and references therein.
24. D. Guidotti and S. A. Rice, Phys. Rev. B14 (1976) 5518
C. C. Kao and E. M. Conwell, Phys. Rev. B14 (1976) 2464.
25. ϵ_1 is taken from L.G. Schulz and F.R. Tangherlini, J. Opt. Soc. Am. 44 (1954) 357; $\epsilon_2 = 1$ and $\epsilon_3 = 2.25$.
26. J. Bösenberg, Phys. Lett. 37A (1971) 439.
27. H. Yasunaga, Rev. Sci. Instrum. 47 (1976) 726.
28. C.S. Wang, J. Appli, Phy. 48 (1977) 1477.
29. D.L. Fehrs and R.E. Stickney, Surface Sci. 24 (1971) 309.
30. G. Hincelin and A. Septier, Proc. 7th Int. Vac. Congress and 3rd Int. Conf. Solid Surfaces (Vienna, 1977) 1269.

FIGURE CAPTIONS

Figure 1. Geometries of (a) a sharp-boundary model of a metal-vacuum interface, (b) a prism-metal-vacuum Kretschmann configuration (c) a metal-transition layer-vacuum model of a metal-vacuum interface, and (d) a prism-metal-transition layer-vacuum Kretschmann configuration. The metal, vacuum, prism and the transition layer are labeled as media 1, 2, 3, and 4, respectively.

Figure 2. The η vs (d_1/d_{opt}) curve. η increases exponentially with increasing (d_1/d_{opt}) and is equal to 1 at $d_1/d_{opt} = 1$.

Figure 3. (a) The experimental setup. 1: prism, 2: shutter, 3: Ag evaporator, 4: electron collector, 5: Cs source, 6: ionization gauge, 7: O_2 gas tank, 8: variable leak valve and 9: window.
(b) The experimental ATR configuration.

Figure 4. The photocurrent (I) vs the deposition time (t) curve.

Figure 5. Typical R vs α curves of a silver-vacuum interface in the presence of Cs of 2.5×10^{14} atoms/cm² coverage and of the Cs layer exposed to O_2 gas.

Figure 6. The frequency dependence of (a) α_{ATR} , (b) W_α and (c) R_{min} .

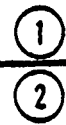
Figure 7. The frequency dependence of $\Delta\alpha_{\text{ATR}}$.

Figure 8. The reflectance R as function of frequency ω at some fixed angles α for a silver-vacuum interface and with a Cs and a Cs-O submonolayer.

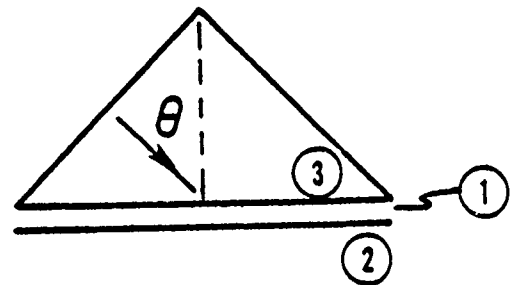
Figure 9. The spectra of (a) $\text{Re}(\Delta K^T)$ and (b) $\text{Im}(\Delta K^T)$ derived by using the four layer model.

z

x

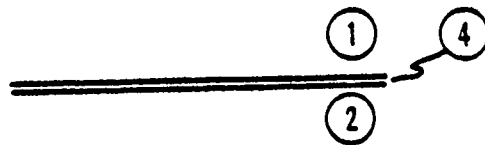


(a)

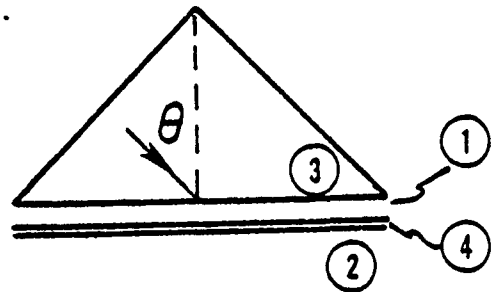


(b)

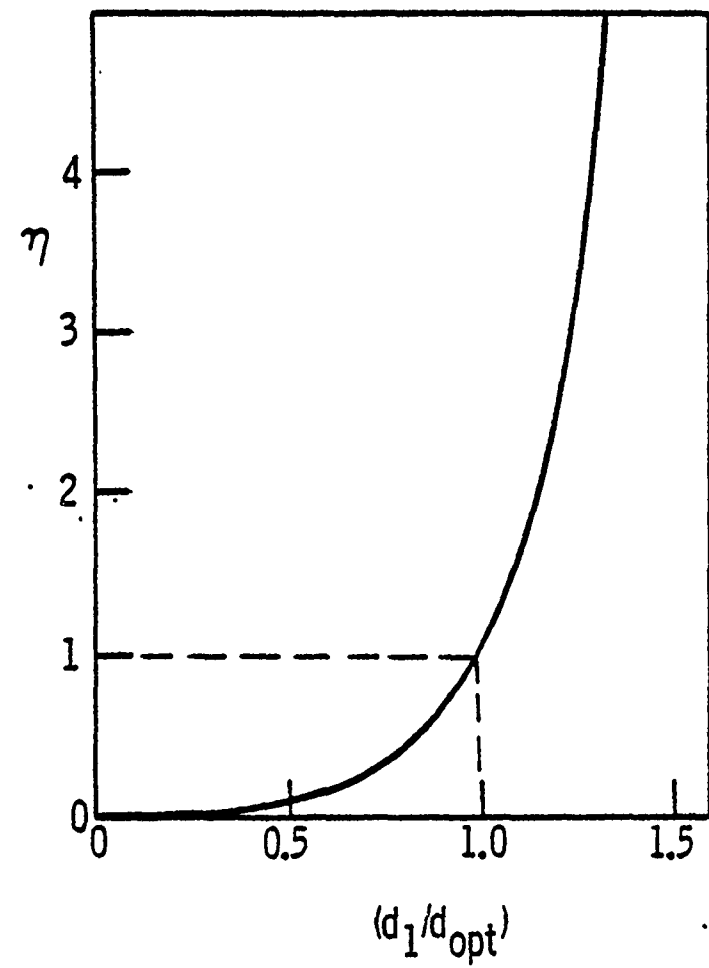
$$\theta > \theta_c$$

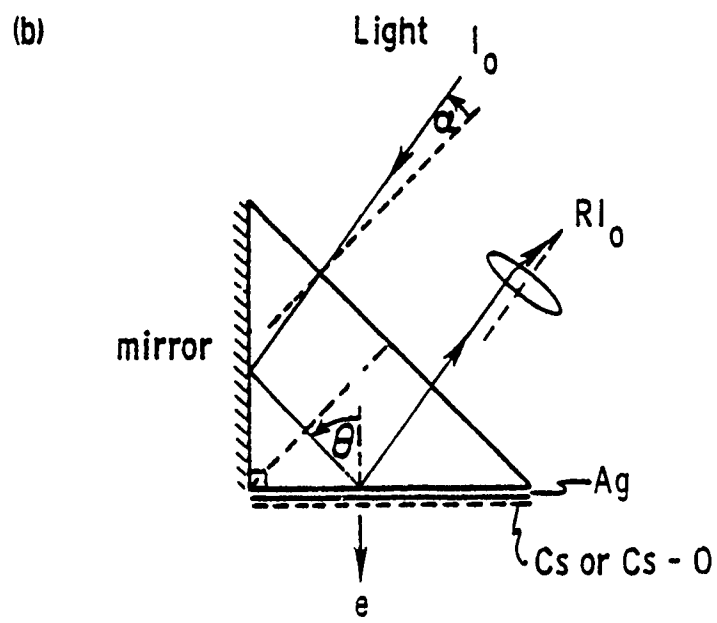
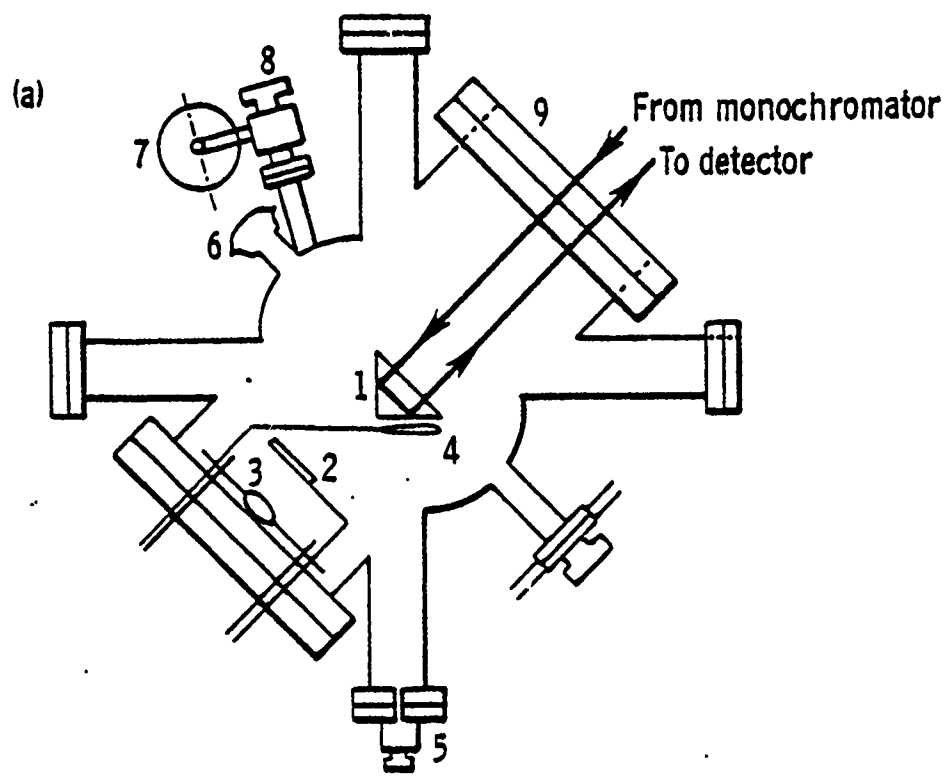


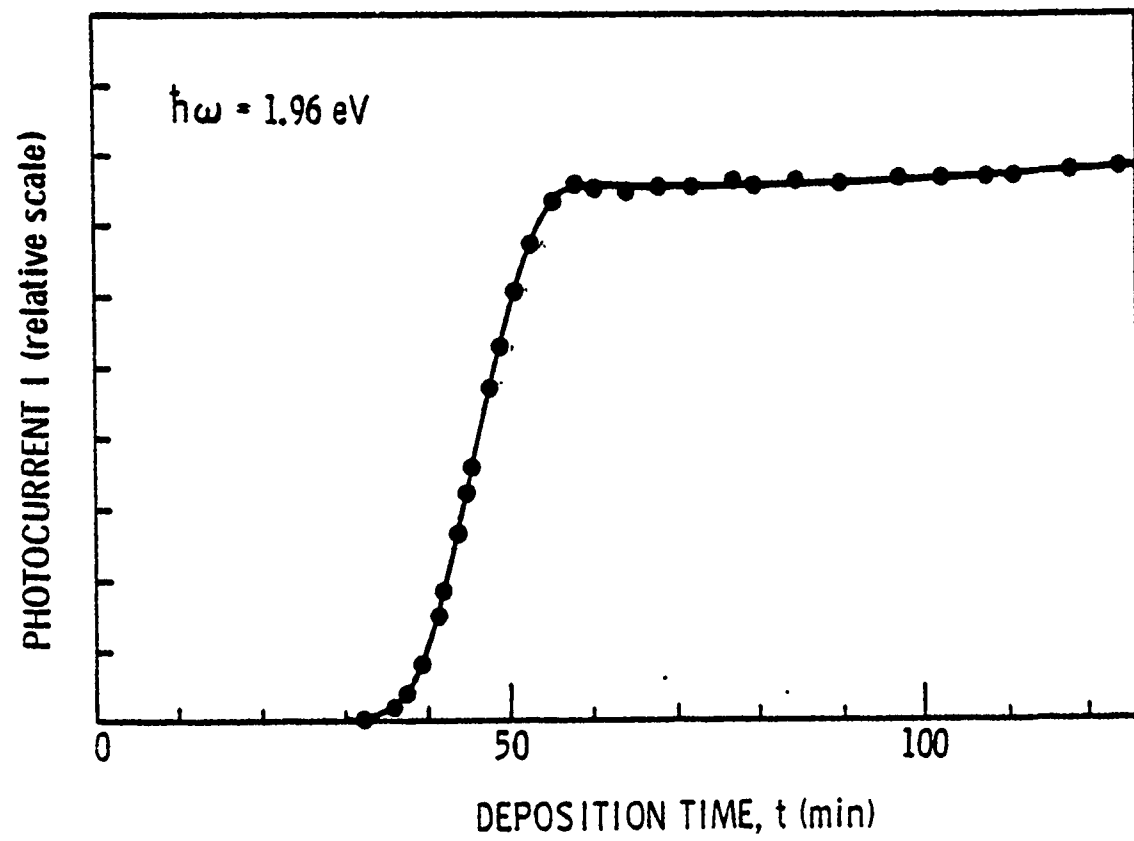
(c)

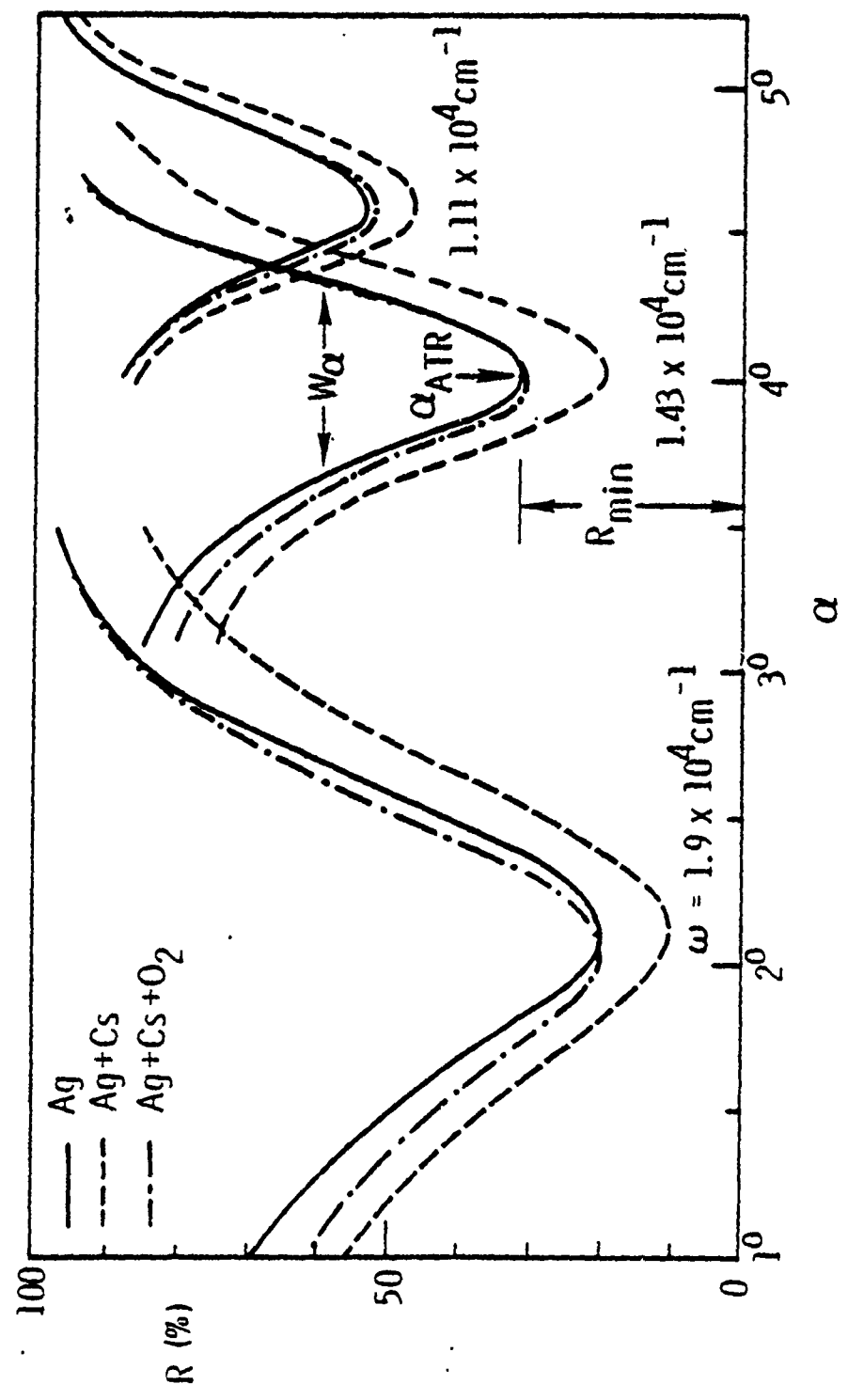


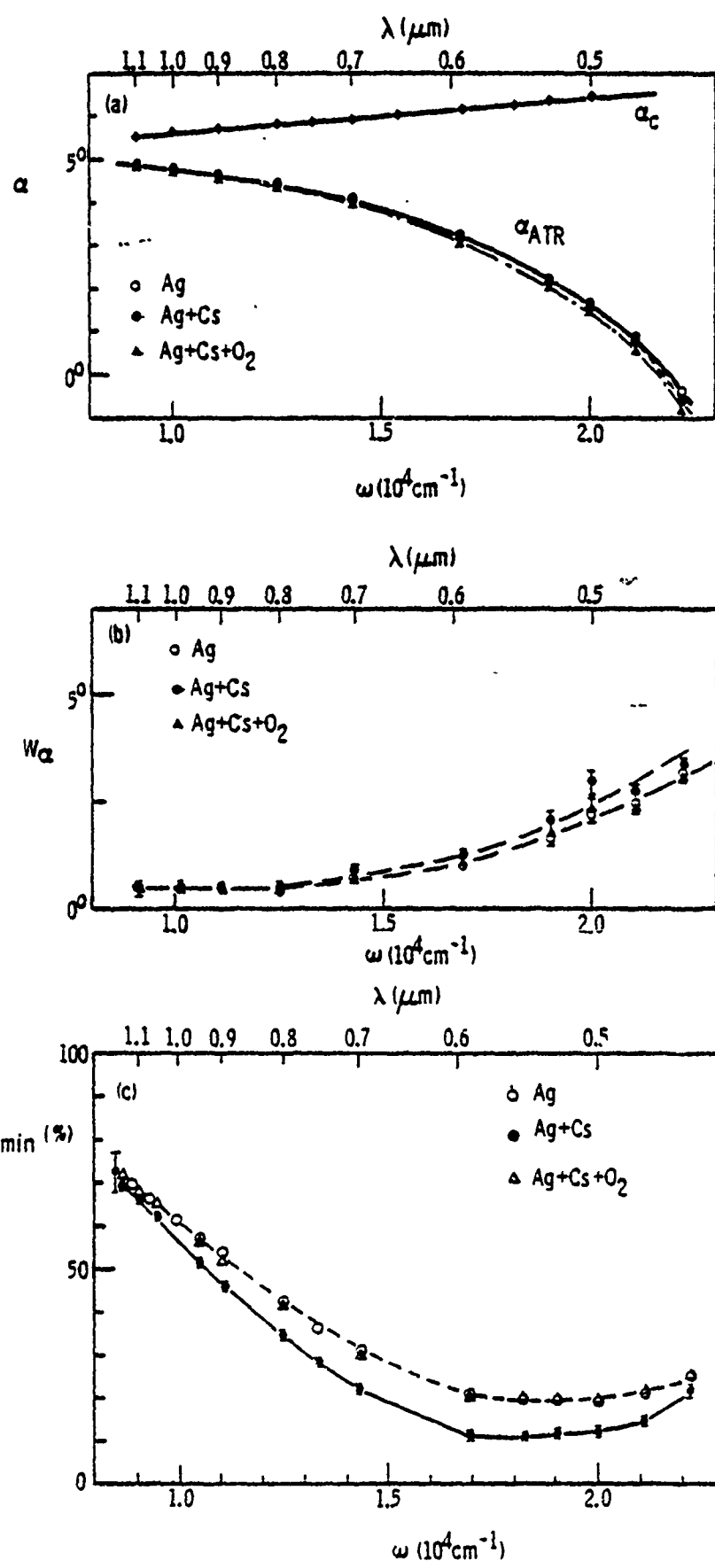
(d)

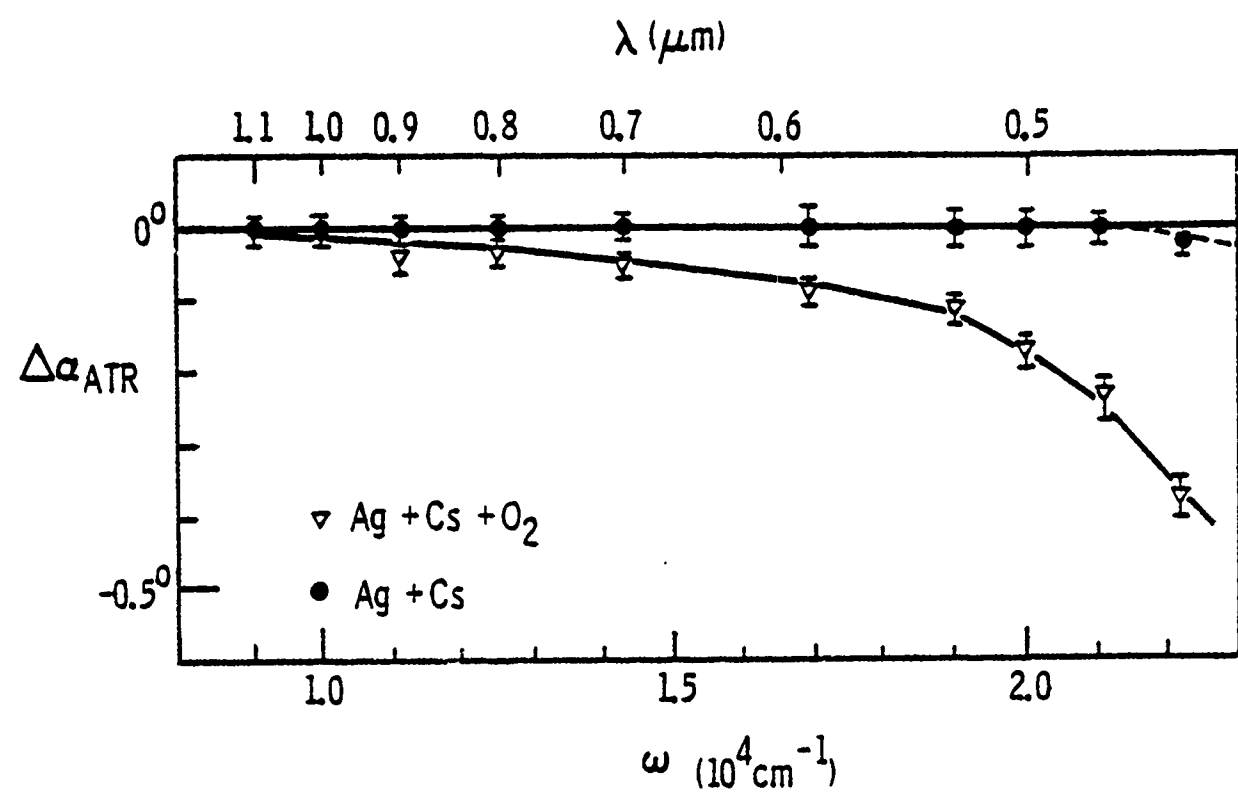


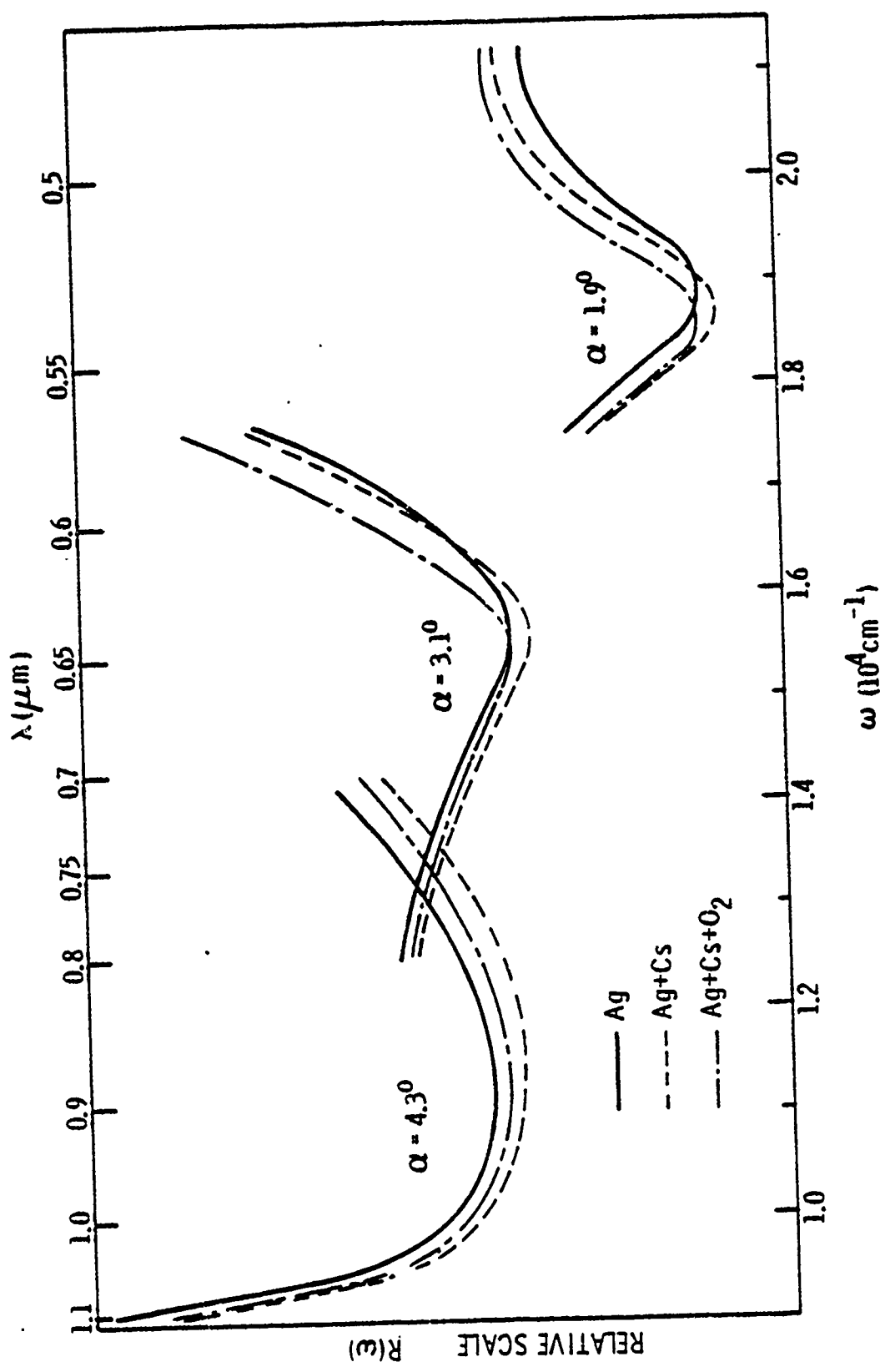


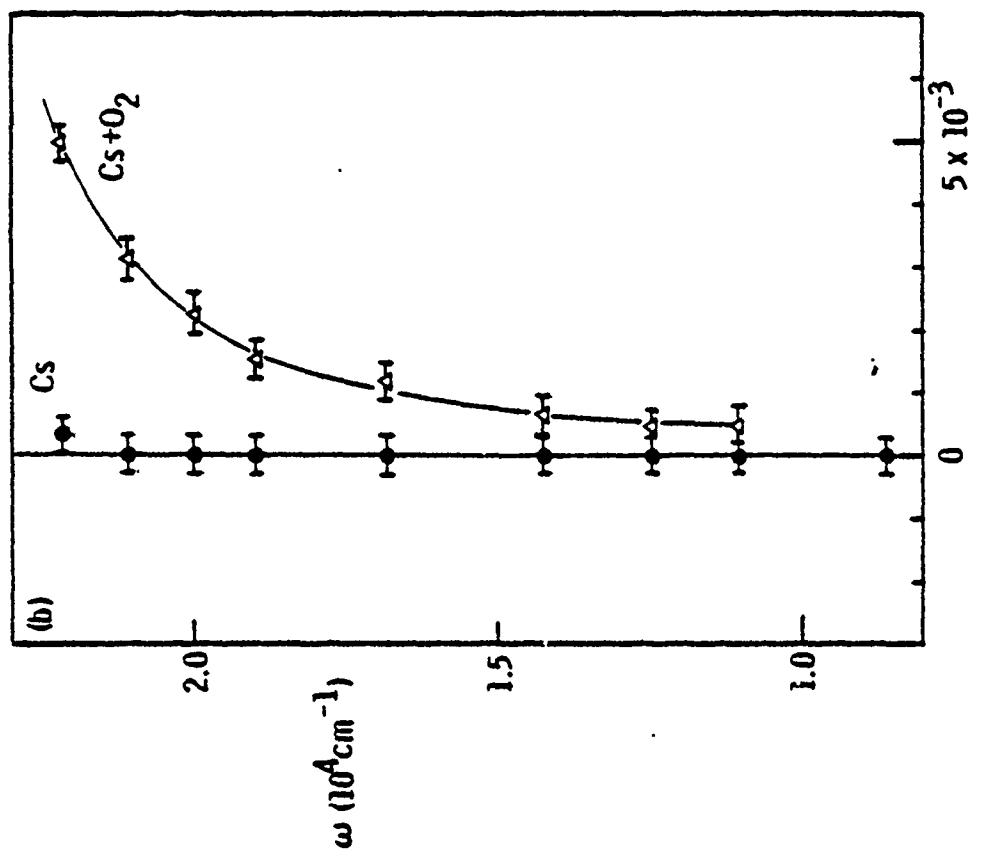
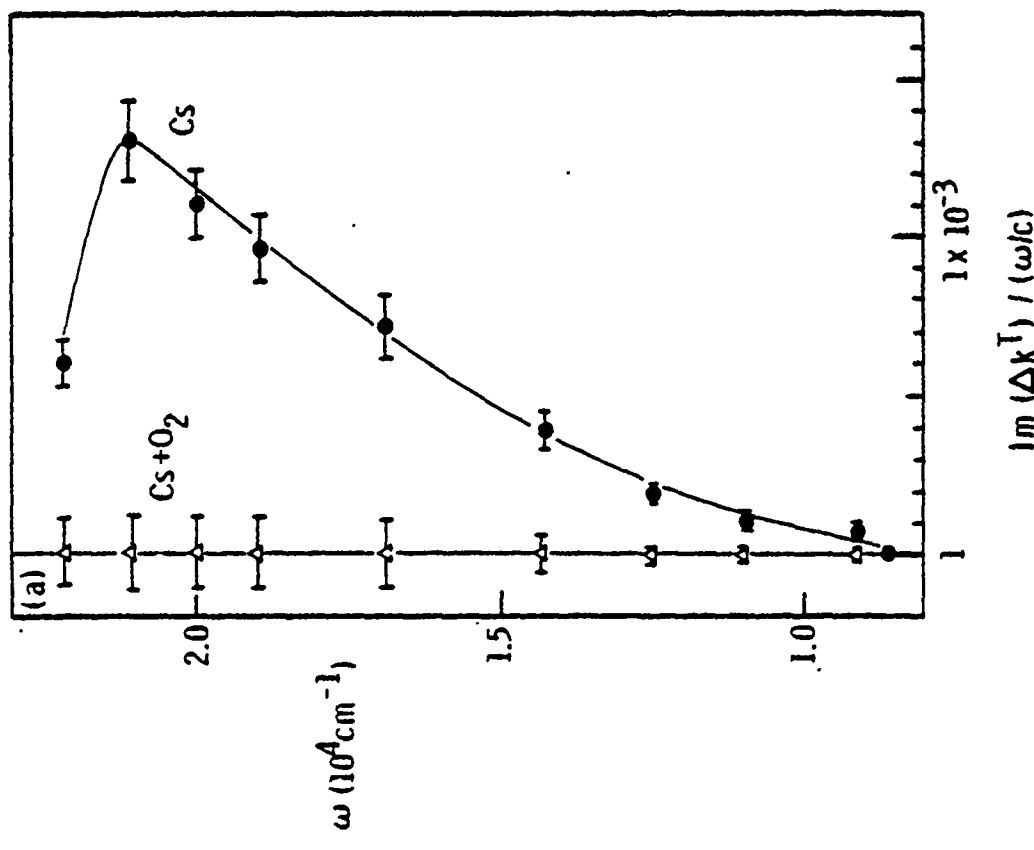












APPENDIX II

APPENDIX II

On the use of surface plasma waves for
determination of the thickness and optical constants
of thin metallic films*

W. P. Chen and J. M. Chen
Martin Marietta Laboratories
1450 South Rolling Road
Baltimore, Maryland 21227

The surface plasma wave technique for determining the dielectric constant $\epsilon(\omega)$ and the thickness d of a metal film without a preset expression for $\epsilon(\omega)$ is discussed. Two sets of solutions can be derived at a given frequency. By comparing d determined at another frequency, the correct $\epsilon(\omega)$ and d can be determined.

*Work supported by Army Research Office, Contract DAAG 29-77-C-0036.

The optical property of a metallic film can be characterized by a frequency-dependent dielectric constant $\epsilon(\omega)$. Among many optical methods,^{1,2} the surface plasma wave (SPW) technique² is particularly suited for the study of the $\epsilon(\omega)$ of a thin metallic film a few hundred Å in thickness. Recently, Lopez-Rios and Vuye² used the SPW technique to determine the thickness, d , and $\epsilon(\omega)$ of thin Ag films. They performed a least squares fit of the reflectance minima at resonant excitation of SPW in the 4000-6000 Å range. For the $\epsilon(\omega)$ of Ag they took a frequency-dependent function which accounts for both the contributions from the intraband transition of electrons and the interband transition starting at $h\nu = 3.86$ eV ($\lambda = 3250$ Å). As long as the expression for $\epsilon(\omega)$ is known, this method serves well to determine d and the parameters used in the $\epsilon(\omega)$ expression. However, in many studies, a preset expression for $\epsilon(\omega)$ that includes the contributions from the interband transition is impossible. Therefore, a method of determining $\epsilon(\omega)$ and d at any given frequency without a preset $\epsilon(\omega)$ is needed. The method was first given by E. Kretschmann³ and later used by others⁴. It has been presented that a unique set of $\epsilon(\omega)$ and d can be found from the reflectance minima of SPW at a given frequency.

In this paper, we will discuss the SPW technique for determining the $\epsilon(\omega)$ and d without a preset expression for $\epsilon(\omega)$. We found that two sets of $\epsilon(\omega)$ and d solutions can be derived

from the resonant excitation of SPW at a given frequency. One corresponds to the undercoupling of a damped SPW and the other corresponds to the overcoupling of a less damped SPW. Only with solutions determined at another frequency, the correct sets for $\epsilon(\omega)$ and d solution, namely those with the same d for both frequencies, can be selected.

For convenience of discussion, we will review briefly the excitation of SPW in a Kratzschmann attenuated total reflection (ATR) configuration.^{3,5} Let us consider an incident TM light of frequency ω in a prism-metal-vacuum configuration as shown in Fig. 1: when the light is incident at an angle θ larger than the critical angle θ_c , it can couple directly with SPW of the metal-vacuum interface; here $\theta_c = \sin^{-1}(1/n)$ and n is the index of refraction of the prism. The coupling takes place when ω and $K_x(\theta)$ of the incident light match with the frequency ω and the complex wavevector K of the SPW. Here $K_x(\theta)$ is the component of the incident wavevector parallel to the interface. Since K_x is real and K is complex, only an approximate match can be reached for $K_x(\theta) = \text{Re}(K)$ at

$$\theta = \theta_{\text{ATR}} = \sin^{-1}[\text{Re}(K) c/n] \quad (1)$$

At θ_{ATR} , the total reflection of the incident light is attenuated. The coupling can be analyzed by calculating the reflectance,

R, of the light given by

$$R = \left| \frac{\gamma_{31} + \gamma_{12} \exp(i2K_{z1}d)}{1 + \gamma_{31}\gamma_{12} \exp(i2K_{z1}d)} \right|^2 \quad (2)$$

with $\gamma_{31} = \frac{\epsilon_{3z} - \epsilon_{1z}}{\epsilon_{3z} + \epsilon_{1z}}$

$$\gamma_{12} = \frac{\epsilon_{1z} - \epsilon_{2z}}{\epsilon_{1z} + \epsilon_{2z}}$$

and $K_{jz} = \left(\epsilon_j \frac{\omega^2}{c^2} - k_x^2 \right)^{1/2}$ for $j = 1, 2, 3$ (3)

$$k_x = n \frac{\omega}{c} \sin(\theta) \quad (4)$$

where the subscripts 1, 2, and 3 designate the quantities in the metal, air, and the prism respectively, ϵ_j and K_{jz} are the dielectric constants and the wavevector components perpendicular to the interface in medium j ; d is the thickness of the metal film and $\lambda = 2\pi c/\omega$ is the wavelength of light in vacuum. Here $\epsilon_1 = \epsilon_1' + i\epsilon_1''$, $\epsilon_2 = 1$, and $\epsilon_3 = n^2$.

With θ close to θ_{ATR} , the reflectance R can be approximately expressed as a function of θ as ^{3,6,7}

$$R(\theta) = 1 - \frac{4 \operatorname{Im}(K^0) \operatorname{Im}(K^R)}{[K_z - \operatorname{Re}(K)]^2 + \operatorname{Im}(K)^2} \quad (5)$$

$$\text{with } K = K^0 + K^R$$

$$\begin{aligned} K^0 &= \left(\frac{\epsilon_1 \epsilon_2}{\epsilon_1 + \epsilon_2} \right)^{1/2} \frac{\omega}{c} \\ &= \left(\frac{\epsilon'_1 \epsilon'_2}{\epsilon'_1 + \epsilon'_2} \right)^{1/2} \frac{\omega}{c} + i \left(\frac{\epsilon''_1 \epsilon''_2}{2 \epsilon'_1 (\epsilon'_1 + \epsilon'_2)} \right)^{1/2} \frac{\epsilon''_1 \epsilon''_2}{2 \epsilon'_1 (\epsilon'_1 + \epsilon'_2)} \frac{\omega}{c} \end{aligned} \quad (7)$$

$$K^R = \frac{\omega}{c} (-\gamma_{31}) \quad K = K^0 \left(\frac{2}{\epsilon_1 + \epsilon_2} \right) \left(\frac{\epsilon_1 \epsilon_2}{\epsilon_1 + \epsilon_2} \right)^{3/2} \quad (8)$$

$$x \exp \left[i \frac{4\pi d}{\lambda} - \frac{\epsilon_1}{(\epsilon_1 + \epsilon_2)^{1/2}} \right]$$

Here K is the complex wavevector of the SPW in the Kretschmann configuration, and K^0 is the complex wavevector of the SPW at the metal-vacuum interface in the absence of the prism. K^R is the perturbation to K^0 in the presence of the prism. The imaginary parts of K^0 and K^R are the intrinsic and radiative dampings, respectively. The former represents the Joule loss in the metal, and the latter represents the leakage loss of the SPW back into the prism.

The reflectance has a Lorentz dip at θ_{ATR} with a half-width W_θ (when $|Im(K)| < |Re(K)|$) and a minimum reflectance R_{min} given by

$$W_\theta = 2 \operatorname{Im}(K) \cos(\theta_{ATR}) c/nw \quad (9)$$

$$R_{min} = 1 - 4\eta/(1+\eta)^2 \quad (10)$$

where

$$\eta = \operatorname{Im}(K^0)/\operatorname{Im}(K^R). \quad (11)$$

With Eqs. (1) to (11), we can proceed to determine the dielectric constant ϵ_1' and thickness d of a metal film from the measured R versus θ curve. The ϵ_1' and d of the metal film can be determined by best fitting of the data with R given by Eq. (2) by the method of differential correction⁸ and iteration. The initial value of ϵ_1' and d can be determined as follows: 1) substitute the measured θ_{ATR} into Eq. (1) to calculate $Re(K)$; 2) set $Re(K^0) = Re(K)$, because $Re(K^R) \ll Re(K^0)$; 3) determine ϵ_1' by using the real part of Eq. (7); 4) determine $[(\operatorname{Im}(K^0) + \operatorname{Im}(K^R)) = \operatorname{Im}(K)]$ by substituting the measured θ_{ATR} and W_θ into Eq. (9); 5) determine $\operatorname{Im}(K^0)/\operatorname{Im}(K^R)$ from the results obtained in steps 4 and 5; 7) determine ϵ_1'' by substituting ϵ_1' and $\operatorname{Im}(K^0)$ into the imaginary part of Eq. (7); 8) determine d by substituting θ_{ATR} , ϵ_1' , ϵ_1'' , and $\operatorname{Im}(K^R)$ into the imaginary part of Eq. (8).

In this fashion, we obtain two sets of initial values for ϵ_1 and d , because there are two solutions for $\text{Im}(K^0)/\text{Im}(K^R)$ when R_{\min} is substituted into Eq. (10). These two solutions of $\text{Im}(K^0)/\text{Im}(K^R)$ are reciprocals of each other. One corresponds to the case in which the intrinsic damping is larger than the radiative damping (undercoupling) and the other is the reverse (overcoupling). The estimated d of the former is larger than that of the latter. In the absence of the prism, the SPW corresponding to undercoupling has a shorter propagation length than that corresponding to overcoupling. However, to a first-order approximation, these SPW's are indistinguishable in an ATR configuration. Therefore, both sets of solutions serve equally well as the initial values for the iteration process and lead to equally good fits. Consequently, we have two solutions of ϵ_1 and d for a $R(\theta)$ curve at a given frequency. Since the d value should not depend on frequency, the correct ϵ_1 at each frequency can be selected by comparing the resultant d from fitting at two different frequencies.

In our experiment, we have deposited a thin Ag film on the base of a glass prism to form a prism-Ag-vacuum configuration in an ultra-high-vacuum chamber at a pressure of 1×10^{-8} Torr. The reader is referred to reference 6 for details of the experimental setup. The measured angular dependence of R at resonance of SPW is shown in Fig. 2 as R vs $K_x/(w/c)$ for $\lambda = 6328 \text{ \AA}$ and

and 4358 Å, respectively.

Results of the data fit are also given in Fig. 2. The average deviation of R between the data and theoretical value is about 2%. For the case of 6328 Å, two equally good fits are presented as solid triangles (Δ) for $\epsilon_1 = -17.45 + i 0.92$ and $d = 387$ Å and as solid circles (\bullet) for $\epsilon_1 = -16.72 + i 1.66$ and $d = 483$ Å. Note that a measurement of R more accurate than 2% would allow these two sets of values to be distinguished. However, this requires a theoretical analysis of the SPW resonance beyond the first-order approximation. For 4358 Å, the fits are presented as open triangles (Δ) for $\epsilon_1 = -5.25 + i 0.53$ and $d = 567$ Å and as open circles (\circ) for $\epsilon_1 = -5.25 + i 0.32$ and $d = 467$ Å. After comparing the thicknesses, we conclude that d is about 475 Å and the dielectric constants are $\epsilon_1 = -16.72 + i 1.66$ at 6328 Å and $\epsilon_1 = -5.25 + i 0.32$ at 4358 Å. The dielectric constants agree well with the existing bulk constants of Ag:^{9,10} $\epsilon_1 = -16.32 + i 0.54$ at 6328 Å and $\epsilon_1 = -5.19 + i 0.28$ at 4358 Å.

The above procedure can be extended to fit the SPW reflectance minima at several (e.g., m) frequencies. In this case, the thickness d and the m complex dielectric constants form $2m+1$ parameters to be fitted. A least squares fit can solve these parameters simultaneously without a preset formula for the $\epsilon(\omega)$.

This fitting method is important for determining $\epsilon_1(\omega)$ of a metal film of thickness from 100 \AA to 1000 \AA when the thickness can not be known within an accuracy of $\pm 50 \text{ \AA}$. In this thickness range, the leakage loss and the Joule loss of a SPW are comparable. The method can also work for $d > 1000 \text{ \AA}$. However, due to the fact the leakage loss is much smaller than the Joule loss, $\epsilon_1(\omega)$ can be simply derived from equations (1), (7), and (9) by taking $K \approx K^*$, i.e. ignoring K^R . The resultant $\epsilon_1(\omega)$ derived from the approximate method only deviated from that derived from an exact fitting about $(1 - R_{\min})/4$. For example, when $R_{\min} = 90\%$, the deviation is only 2.5%. The least squares fit can also be applied to fit $R(\theta)$ curves for $d < 100 \text{ \AA}$. For this case, because the angular dependence of EM fields in the metal film is dominantly determined by ϵ_2 and ϵ_3 , the relative angular dependence of reflectance (absorption is equal to $1-R$) does not show significant dependence on ϵ_1 . Only the absolute value of reflectance depends on the product of d and ϵ_1'' , because the product is equivalent to the product of the absorption coefficient and the area density of electrons. Therefore, the least squares fit only given the $d \times \epsilon_1''$ product, but not an accurate ϵ_1' or $\epsilon_1'd$. The correlation between d and ϵ_1'' can not be removed by including more data at different ω , but can be removed by a determination of d by other methods.

In conclusion, fitting the angular dependence at SPW resonance at a given frequency provides two sets of ϵ_1 and d . One corresponds to undercoupling of a damped SPW and the other corresponds to overcoupling of a less damped SPW. With the help of the d determined at another frequency, a distinction can be made between these two sets. Therefore, the thickness and optical constants of thin metallic films can be determined by using the resonance of surface plasma waves at any given frequency without a preset $\epsilon(\omega)$.

References

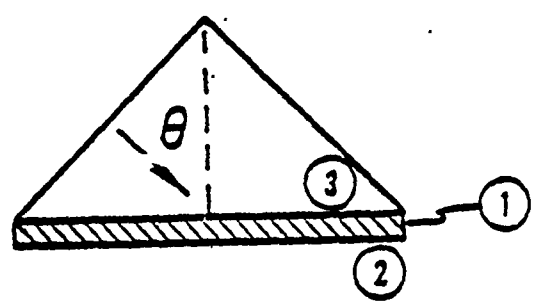
*Work supported by Army Research Office, Contract #DAAG29-77-C-0036.

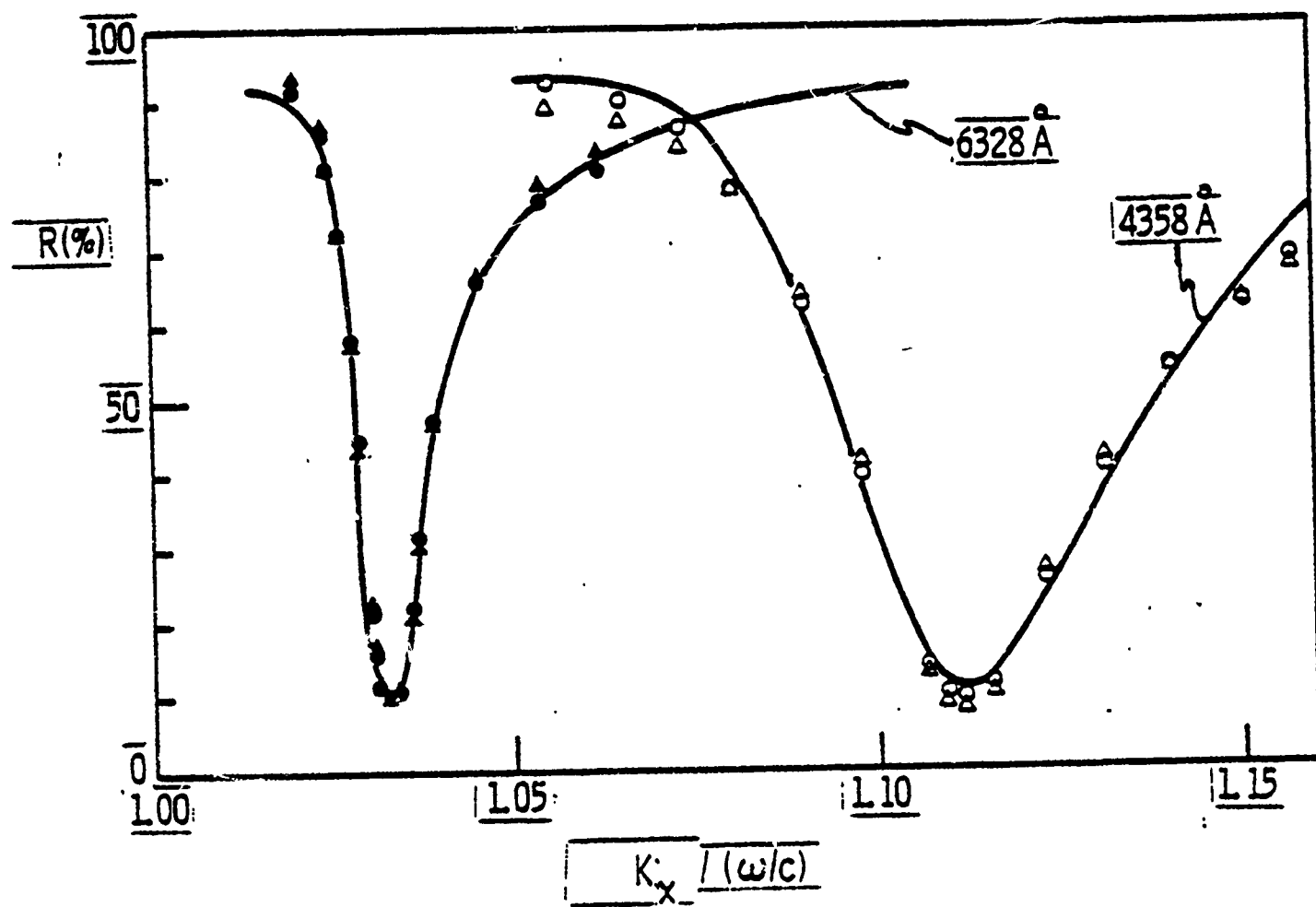
1. Optical Properties and Electronic Structure of Metals and Alloys. Edited by F. Abeles, North-Holland, Amsterdam, (1965).
2. T. Lopez-Rios and G. Vuye, "Use of surface plasmon excitation for determination of the thickness and optical constants of very thin surface layers," Surf. Sci. 81, 529-538 (1979).
3. E. Kretschmann, "Die bestimmung optischer konstanten von metallen durch anregung von oberflachenplasmaschwingungen," Z. Physik 241, 313-324 (1971).
4. T.L. Haltom, E.T. Arakawa, M.W. Williams, and E. Kretschmann, Applied Optics 18, 1233-1236 (1979).
5. E. Burstein, W. P. Chen, Y. J. Chen, and A. Hartstein, "Surface polaritons-propagating electromagnetic modes at interfaces," J. Vac. Sci. Technol. 11, 1004-1019 (1974).
6. W. P. Chen and J. M. Chen, "Surface plasma wave study of submonolayer Cs and Cs-O covered Ag surfaces," Surf. Sci. 91, 601-617 (1980).
7. I. Pockrand, "Surface plasma oscillations at silver surfaces with thin transparent and absorbing coatings," Surf. Sci. 72, 577-588 (1978).
8. K. L. Nielsen, Methods in Numerical Analysis, p. 308. MacMillan, New York, (1964).
9. L. G. Schulz, "The optical constants of silver, gold, copper, and aluminum I. the absorption coefficient k ," J. Opt. Soc. Am., 44, 357-362 (1954).
10. L. G. Schulz and F. R. Tangherlini, "Optical constants of silver, gold, copper, and aluminum II. the index of refraction n ," J. Opt. Soc. Am. 44, 362-368 (1954).

Figure Captions

Figure 1. A prism-metal-vacuum Kretschmann configuration. The metal, vacuum, and prism are labeled as media 1, 2, and 3, respectively.

Figure 3. Numerical fitting of measured R versus $K_x/(\omega/c)$ curves at 6,328 Å and 4,358 Å. Solid curves are data. Calculated reflectance for each fitting are shown by the symbols A, \bullet , Δ , and O. For A, $(d, \epsilon_1) = (387 \text{ \AA}, -17.45 + i 0.92)$; \bullet , $(483 \text{ \AA}, -16.72 + i 1.66)$; Δ , $(567 \text{ \AA}, -5.25 + i 0.53)$; and O, $(467 \text{ \AA}, -5.25 + i 0.32)$.





APPENDIX III

APPENDIX III
**NARROW-BEAM EXCITATION OF ELECTROMAGNETIC MODES
IN PRISM CONFIGURATIONS**

Wenpeng Chen
Martin Marietta Laboratories
1450 South Rolling Road
Baltimore, Maryland 21227

and

Elias Burstein
Department of Physics
University of Pennsylvania
Philadelphia, Pennsylvania 19104

1. Introduction

Otto¹ and Kretschmann² attenuated-total-reflection (ATR) prism configurations are frequently used to excite surface electromagnetic (S-EM) waves at an air-metal interface. The Otto configuration is formed by placing a prism above the metal surface and leaving an air gap, whereas the Kretschmann configuration is formed by depositing a thin metal film on the base of a prism. In the Kretschmann configuration, S-EM waves also exist at the prism-metal interface. However, only the S-EM waves at the air-metal interface can be excited in the ATR configuration.³ In this chapter, when we use the term S-EM waves, we will be referring to the S-EM waves at the air-metal interface of the two ATR configurations.

For the present purpose, we will limit our discussion to the case of isotropic media, where S-EM waves are transverse magnetic polarized. The S-EM waves in both ATR configurations are leaky because of their coupling with volume EM (V-EM) waves in the prism. These coupled V-EM waves always propagate at angles θ_1 (with respect to the normal to the interfaces), which are larger than the critical angle $\theta_c = \sin^{-1}(1/n)$, where n is the index of refraction of the prism.

Moreover, there also exist, specifically in the Otto configuration, many branches of Fabry-Perot (FP) EM waves which couple with V-EM waves propagating at angles $\theta_i < \theta_c$.⁴⁻⁶ The FP-EM waves are also leaky. They can be either transverse magnetic (TM) or transverse electric (TE) polarized. The EM fields within the air gap mainly are evanescent in the case of the S-EM waves, but mainly are propagating in the case of the FP-EM waves. The FP-EM waves are due to interference of the two propagating EM waves which are incident at grazing angles upon the metal and the prism base, respectively. Since the EM fields within a metal film are evanescent in the frequency region of interest, FP-EM waves do not exist in the Kretschmann configuration.

Although S-EM waves and FP-EM waves have different field patterns and coupling angles, as far as excitation, launching, and propagation are concerned, they can be described by the same theoretical formulation and investigated by the same experimental setup.

Experimental ATR studies of the EM modes, i.e., the S-EM and the FP-EM waves, can be grouped into two categories: 1) studies of reflection attenuation caused by resonant excitation of the EM modes in a one-prism configuration,⁷⁻²⁰ and 2) studies of propagation of the EM modes in either a one-prism configuration^{6,21} or a two-prism configuration.^{22,25} One of the major differences between these two categories, although usually not mentioned explicitly, is the lateral beam width (W) of the incident V-EM wave used. In general, a broad W , larger than the propagation length (L) of the EM modes, is used for the reflection studies, and a narrow $W \leq L$ is employed for the propagation studies.

Let us consider a V-EM wave of frequency ω incident in a one-prism configuration, as shown in figure 1. In the study of the reflection attenuation, the reflectance (R) of the V-EM wave is measured as a function of angle θ_1 . The R vs θ_1 curve shows a maximum attenuation, i.e., minimum in the reflection, at the angle of resonant excitation of the EM modes. Attenuation occurs because of dielectric loss (absorption) in the metal and "runaway" loss (propagation beyond the excitation region) of the EM modes.

When a broad beam is used, the runaway loss can be ignored. In the theoretical formulation and data analysis of the reflectance minimum, the incident and the reflected V-EM waves can be treated as plane waves. Such a treatment is reasonable for experiments involving the excitation of S-EM waves in the visible, because the propagation lengths of the S-EM waves are on the order of 10 μm , which is much shorter than the width of the incident V-EM wave generally used.

When a narrow beam is used, the runaway loss becomes important and the plane-wave treatment for analyzing the reflectance minimum becomes invalid.²¹ Such is the case when a V-EM wave, with a width in the mm or cm range, is used to excite S-EM waves in the infrared and FP-EM waves in the visible and infrared, because the propagation lengths of these EM modes are comparable to or greater than the beam width generally used.²¹⁻²⁵ In such a narrow-beam excitation, the excited EM modes propagate beyond the illuminated region and radiate into V-EM waves. As a consequence, the reflectance minimum and the shape profile of the reflected beam are different from those derived from a plane-wave treatment. Specifically, when the incident beam has a Gaussian profile, the reflected beam at resonance of the EM modes exhibits a double-peak structure at the leading

edge of the illuminated region, followed by an exponential decay beyond. The R vs θ_1 curve shows a minimum when the reflectance is measured from a local area in the illuminated region, but shows a maximum for "reflection" from the region beyond. Both the profile of the reflected beam and the R vs θ_1 curves can be analyzed by a formulation similar to the one used by Tamir and Bertoni²⁶ to analyze the "lateral displacement of optical beams" in multilayer configurations.

In this chapter, we will limit our discussion to the narrow-beam excitation of leaky S-EM and FP-EM waves in an Otto prism-air-metal configuration. Extensions to a Kretschmann configuration and to prism configurations involving surface-active media other than metals^{3,27-32} are straightforward. The dispersion relation of the leaky EM modes will be discussed in section 2. In section 3, a theoretical analysis of the narrow-beam excitation of the leaky EM modes will be presented. In section 4, we will present data on the narrow-beam excitation of leaky EM modes in the infrared. In the final section, we will present the application of the leaky EM modes as an EM probe of thin layers at metal surfaces, compare the narrow-beam excitations between a one-prism and a two-prism configuration, and discuss other configurations for narrow-beam excitations of S-EM waves.

2. Leaky EM modes in a prism configuration

The dispersion relation of EM modes in a prism configuration is usually derived from the boundary conditions on the EM fields of the EM modes at the prism-air and the air-metal interfaces. It can also be derived using an equivalent process from the Fresnel reflection and

transmission coefficients of an incident V-EM wave in the prism. The latter derivation has the advantage of more clearly relating the dispersion relation to the coupling of the EM modes with incident V-EM waves in the prism. Let us consider a homogeneous, incident, TM-polarized V-EM wave and its reflected and transmitted (into the metal) V-EM waves in a prism-air-metal configuration, as shown in figure 2a. In this figure, the xy plane is the prism-air interface, the z axis is normal to the interface, and the wave vectors of the EM waves lie in the xz plane. Each of these waves is a plane wave with electric and magnetic fields that have components parallel and normal to the interfaces. Since, by applying Maxwell equations, we can use the parallel component E_x of the electric field to express other electric and magnetic field components in each medium, we need only focus on E_x in the following discussion.

Let E_x^0 and E_x^r denote the parallel components of the incident and the reflected electric fields, respectively, at the prism-air interface ($z = 0$), and E_x^t denote the parallel component of the transmitted electric field in the metal at the air-metal interface ($z = -d$). E_x^r and E_x^t can be expressed in terms of E_x^0 by

$$E_x^r = r(K_x) E_x^0 \quad (1)$$

$$E_x^t = t(K_x) E_x^0 \quad (2)$$

$$\text{with } K_x = (\eta\omega/c) \sin\theta_i \quad (3)$$

where K_x is the parallel component of the wavevector of the incident V-EM wave, and $r(K_x)$ and $t(K_x)$ are the reflection and transmission coefficients, respectively. The $r(K_x)$ and $t(K_x)$ are given by

$$r(K_x) = \frac{(\epsilon_2 K_{z3} + \epsilon_3 K_{z2})(\epsilon_1 K_{z2} - \epsilon_2 K_{z1}) + (\epsilon_2 K_{z3} - \epsilon_3 K_{z2})(\epsilon_1 K_{z2} + \epsilon_2 K_{z1}) \exp(i2K_{z2}d)}{(\epsilon_2 K_{z3} + \epsilon_3 K_{z2})(\epsilon_1 K_{z2} + \epsilon_2 K_{z1}) + (\epsilon_2 K_{z3} - \epsilon_3 K_{z2})(\epsilon_1 K_{z2} - \epsilon_2 K_{z1}) \exp(i2K_{z2}d)} \equiv \frac{N}{D} \quad (4)$$

$$t(K_x) = \frac{4 \epsilon_2 \epsilon_1 K_{z3} K_{z2} \exp(iK_{z2}d)}{D} \quad (5)$$

$$\text{with } K_{zj} \equiv K'_{zj} + iK''_{zj} = [(\omega^2/c^2)\epsilon_j - K_x^2]^{1/2} \quad \text{for } j = 1, 2, \text{ and } 3 \quad (6)$$

where the subscripts 1, 2, and 3 designate the quantities in the prism, the air, and the metal, respectively, and ϵ_j and K_{zj} are the dielectric constants and the normal components of the wavevectors in medium j , respectively. When $r(K_x)$ is used to calculate reflectance R , the K_{z1} must have a negative real part and K_{z3} must have a negative imaginary part.

Because the expressions for $r(K_x)$ and $t(K_x)$ are derived from Maxwell's equations and boundary conditions, they can be extended to a case where the "incident" V-EM wave is inhomogeneous. In this case, the denominator (D) in $r(K_x)$ can be used to determine the dispersion relation of EM modes in the prism-air-metal configuration.

Let us consider the effect of the presence of a prism on surface EM waves at an air-metal interface. In the presence of a prism, the evanescent EM field of the S-EM waves in the air undergoes multiple reflections at the prism-air and the air-metal interfaces. The result is a pattern of EM fields which can be represented by one EM field in the metal, one in the prism, and a pair in the air gap, thereby mutually satisfying the boundary conditions.

For simplicity, but without sacrificing generality, we will ignore dielectric loss in the metal for the moment and assume ϵ_3 is real. In

the case where the S-EM waves have $K_x > \epsilon_1^{1/2} \omega/c$, the resultant EM field in the prism is nonradiative and decays in the positive z direction. Since all ϵ_j are real, K_{Zj} are purely imaginary. If we require that K_{Z1} and K_{Z3} are negative imaginary and $D = 0$, then we have E_x^r , E_x^t , and a pair of EM fields in the air without an incident EM wave, i.e., $E_x^o = 0$. E_x^r and E_x^t decay exponentially in the positive and negative direction, respectively. These four fields constitute the pattern of EM fields of nonradiative S-EM waves in the presence of the prism. Thus, $D = 0$ with the condition of negative imaginary K_{Z1} and K_{Z3} gives the dispersion relation of the nonradiative S-EM waves in the prism-air-metal configuration.

In the case where the S-EM waves have $K_x < \epsilon_1^{1/2} \omega/c$, the resultant EM field in the prism is leaky into the prism. Its Poynting vector reflects away from the prism as shown in figure 2b. Because of radiative damping, the leaky S-EM wave decays exponentially during propagation, i.e., $K_x (= K_x' + iK_x'')$ is complex where K_x' and K_x'' are both positive. Since K_x is complex, K_{Zj} are complex. If we require that $K_{Z1}' < 0$, $K_{Z3}'' < 0$, and $D = 0$, then we have 1) an EM field E_x^r in the prism with its Poynting vector aiming in the positive z direction, 2) an EM field E_x^t in the metal decaying away from the air-metal interface, and 3) a pair of EM fields in the air gap without an incident EM wave, i.e., $E_x^o = 0$. These four fields form the field pattern of a leaky S-EM wave. Thus, $D = 0$ with the requirement that $K_{Z1}' < 0$ and $K_{Z3}'' < 0$ defines the dispersion relation of leaky S-EM waves. The dispersion relation can be derived in the same way when the dielectric loss is taken into account.

In the prism-air-metal configuration, in addition to the S-EM wave, there also exist many branches of TM and TE leaky EM modes having $K' < \epsilon_2^{1/2}\omega/c$. The prism-air-metal configuration is also a Fabry-Perot interferometer³³ for a V-EM wave incident at $\theta_1 < \theta_c$. The dark fringes of its reflected intensity correspond to excitation of the leaky EM modes having $K' < \epsilon_2^{1/2}\omega/c$. Therefore, we call the leaky EM modes Fabry-Perot EM waves. Let us consider a homogeneous EM wave propagating in the air gap. It will be multiply reflected at both the prism-air and the air-metal interfaces and undergo phase changes ψ_{21} and ψ_{23} each time it is reflected from the prism-air and the air-metal interfaces, respectively. After two consecutive reflections, one at the prism-air and the other at the air-metal interface, the EM wave returns to propagate in the same direction as the original EM wave, but with a phase difference given by

$$\psi = \psi_{21} + \psi_{23} + 2K_{Z2}'d \quad (7)$$

The result of the multiple reflection can be represented by a four-field pattern having an EM field leaky in the prism similar to that of leaky surface EM waves. Therefore, if we extend from the case of the leaky S-EM waves, $D = 0$ with $K_{Z1}' < 0$ and $K_{Z3}'' < 0$ also gives the dispersion relation of the TM FP-EM modes. The condition $D = 0$ can be rewritten as

$$1 - \rho_{21} \rho_{23} e^{i(\psi_{21} + \psi_{23} + 2K_{Z2}'d)} = 0 \quad (8)$$

where

$$\rho_{21} e^{i\psi_{21}} = - \frac{(\epsilon_1 K_{Z2} - \epsilon_2 K_{Z1})}{(\epsilon_1 K_{Z2} + \epsilon_2 K_{Z1})} \quad (9)$$

$$\rho_{23} e^{i\psi_{23}} = \frac{(\epsilon_2 K_{Z3} - \epsilon_3 K_{Z2})}{(\epsilon_2 K_{Z3} + \epsilon_3 K_{Z2})} \quad \text{with } -\frac{\pi}{2} < \psi_{21}, \psi_{23} < \frac{\pi}{2} \quad (10)$$

It is obvious that when equation (8) is satisfied, ψ must be equal to $m(2\pi)$, where m is an integer. Under this condition, constructive interference, which is the key factor of the existence of the FP-EM waves, occurs between the EM fields in the air. The FP-EM waves can be indicated by the integer m . When their K_x' closely approximates $\epsilon_2^{1/2} \omega/c$, the distance the FP-EM waves can propagate is much longer than their wavelength. This situation corresponds to the case where the EM fields in the air gap are incident at grazing angles to both the prism-air and the air-metal interfaces. At grazing incidence, the reflectances from both interfaces are close to unity and a constructive interference of high finesse can occur. The high-finesse interference is the key to obtaining FP-EM waves of long propagation length. The excitation of the FP-EM waves can be achieved by sending a radiation into the prism at an angle below and very close to the critical angle. The FP-EM waves can also exist when the EM field is TE polarized. Their dispersion relation can be derived from the poles of the reflection and the transmission coefficients

of a TE-polarized EM wave similar to our derivation for the TM case.

Note that no TE S-EM waves exist in the prism configuration. Moreover, since homogeneous EM fields do not propagate in a metal film, FP-EM waves do not exist in a Kretschmann configuration.

There are several branches of complex ω versus complex K_x solutions to $D = 0$ corresponding to leaky EM modes. Each one corresponds to the dispersion relation of the leaky EM modes excited under a specific condition. Under the condition of steady-state driving by a narrow beam, the leaky EM modes have a real ω versus complex K_x dispersion relation. If we designate the roots of D as $K = K' + iK''$, then the phase velocity of the leaky EM mode is given by ω/K' and the propagation length, at which the intensity of the EM modes drops to $1/e$, is given by $L = (4\pi K'')^{-1}$.

In figure 3, we plotted the ω versus complex K dispersion curves of leaky S-EM and FP-EM waves of a prism-air-Ag configuration of $d = 38 \mu\text{m}$.⁵ The real and the imaginary parts of K are shown in figure 3 (a and b, respectively). The parameters used are $\epsilon_1 = 2.25$, $\epsilon_2 = 1.0$, and $\epsilon_3(\omega) = 4.44 [1 - 9 \times 10^8 / \omega(\omega + 1600)]$ (where ω is in the unit of cm^{-1}), which closely resembles the measured dielectric constant of Ag in the infrared.³⁴

In figure 3(a), the dispersion curve of leaky S-EM waves is labelled as S and lies in the region of $K' > \omega/c$. The curve is indistinguishable from the dispersion curve of the S-EM wave of the air-Ag interface (shown in dashes). The dispersion curves of FP-EM waves are labelled according to the integer m in ψ (we show only the cases where $m = 0, 1, 2$, and 3). As one can see, the $K' / (\omega/c)$ of FP-EM waves increases as ω increases. For the cases of $m = 1, 2$, and 3, the dispersion curves approach the

line representing $K'/(ω/c) = 1$. As $ω$ increases, the dispersion curve of the $m = 0$ TM FP-EM wave becomes the dispersion curve of the S-EM waves.⁶ In fact, the $m = 0$ TM FP-EM wave can be considered as a modified S-EM wave in the presence of a prism: Since the influence of a prism becomes progressively stronger at a small air gap, the S-EM wave becomes the $m = 0$ TM FP-EM wave. Figure 4 illustrates the air-gap dependence of $K'/(ω/c)$ of a leaky S-EM wave of $ω = 943 \text{ cm}^{-1}$. The figure shows the change from a leaky S-EM wave into a $m = 0$ TM FP-EM wave at an air-gap of 110 μm . The parameters used for calculation are $ε_1 = 2.25$, $ε_2 = 1$, and $ε_3 = -3849 + 11451$. Since the $m = 0$ FP-EM waves originate from leaky S-EM waves, in the following discussion we refer to them as leaky S-EM waves also.

Figure 3(b) show $ω$ versus $K''/(ω/c)$ curves. The term $K''/(ω/c)$ is a measure of the decay of the leaky EM modes that is caused by 1) intrinsic damping due to dielectric loss, and 2) radiative damping, which increases exponentially with decrease of the ratio of air gap to the penetration depth, $δ$, of the EM field in the air. The $K''/(ω/c)$ of the S-EM wave decreases when $ω$ decreases from 7×10^3 to $2 \times 10^3 \text{ cm}^{-1}$. In this frequency region, the intrinsic damping of a S-EM wave dominates because $d/δ > 1$. The intrinsic damping decreases with $ω$ as shown by the dashed curve in the same figure. Therefore a decrease of $K''/(ω/c)$ reflects a decrease of the intrinsic damping. Because $d/δ$ decreases with decreases of $ω$, the radiative damping of the S-EM wave starts to play a role in $K''/(ω/c)$ at $ω = 2 \times 10^3 \text{ cm}^{-1}$, at which $d = δ$. An increase of $K''/(ω/c)$ for $ω < 2 \times 10^3 \text{ cm}^{-1}$ reflects an increase in the radiative damping with decreasing $ω$.

The $K''/(\omega/c)$ of the $m = 0, 1, 2$, and 3 FP-EM modes always increases with decreasing ω because the dominant damping is radiative for FP-EM waves. Clearly, the propagation length L , which is given by $[4\pi K'']^{-1}$, is longer for a FP-EM wave than for a S-EM wave in the high-frequency region; the reverse is true in the low-frequency region. All the leaky EM modes can have macroscopic propagation lengths. For example, from the number shown in figure 3b, we can derive $L = 1.99$ mm, 0.86 mm, 0.33 mm, and 0.15 mm at $\omega = 2 \times 10^3$ cm $^{-1}$ ($\lambda = 5$ μm), for the S-EM wave and the $m = 1, 2$, and 3 FP-EM modes, respectively.

When an incident EM wave excites leaky EM modes, its reflectance shows minima at the resonant excitation of the leaky EM modes. Typical R versus K_x curves of $\omega = 943$ cm $^{-1}$ are shown in figure 5. The air gaps are as indicated; the dielectric constants are those used for calculating K in figure 4. The large K_x minimum of each curve corresponds to the excitation of leaky S-EM waves ($m = 0$ TM FP-EM waves), and the small K_x minimum corresponds to the excitation of $m = 1$ TM FP-EM waves. The minima corresponding to excitation of higher order FP-EM waves are off the scale on the left-hand side. All the minima occur at $K_x = K'$ with a half width equal to K'' , where $K = K' + iK''$ is the wavevector of the leaky EM modes. Therefore, the plot of the R versus K_x curves can also serve as a simple method for determining K of the leaky EM modes in the prism configuration.

The agreement between K determined by $D = 0$ with $K_{Z1}' < 0$ and $K_{Z3}'' < 0$ and K determined by the R versus K_x plot is due to the condition $K'' \ll K'$ and can be clearly seen in the following discussion.

When $K_x \approx K'$, and when $K'' \ll K'$, we can approximately express $r(K_x)$ and $t(K_x)$ in terms of the wavevector of the leaky EM modes as follows:^{21,35}

$$r(K_x) = A + B \frac{1}{(K_x - K)/(w/c)} \quad (11)$$

$$t(K_x) = C \frac{1}{(K_x - K)/(w/c)} \quad (12)$$

$$\text{with } A = (N'/D') \Big|_K \quad (13)$$

$$B = (w/c)(N/D') \Big|_K \quad (14)$$

$$\text{and } C = (w/c)[4 \epsilon_3 \epsilon_2 K_{Z2} K_{Z1} \exp(iK_{Z2}d)/D']_K \quad (15)$$

where D' and N' are the derivatives of D and N with respect to K_x evaluated at K . From a mathematical viewpoint, there are four possible solutions to Maxwell equations; each has one EM field in the prism, one in the metal and a pair in the air, mutually satisfying boundary conditions. All can be derived from $D = 0$, but in combinations of $+K_{Z1}$ or $-K_{Z1}$ with $+K_{Z3}$ or $-K_{Z3}$. Changing the sign of K_{Z2} does not change the dispersion relation. Because K_{Z1} of an incident V-EM wave is negative real and K_{Z3} of its transmitted V-EM wave has a dominating negative imaginary part, equations (11) and (12), which are derived from the Taylor expansion, are valid only when K is one of the four solutions. This solution also has negative K_{Z1}' and K_{Z3}'' , i.e., the wave vector of a leaky EM wave.

From equations (2) and (12) we find that the square of the magnitude of E_x^t has a K_x dependence proportional to $1/[(K_x - K')^2 + K''^2]$. The

absorption α inside the metal is proportional to $|E_x^t|^2$ and, therefore, also has the same dependence on K_x . As a consequence, the reflectance R , which is equal to $|r|^2$ and can also be expressed as $(1-\alpha)$, shows a minimum at $K_x = K'$ with a half width equal to K'' .

3. Narrow-beam excitation - theory

An actual beam of V-EM radiation has finite widths in the x and y directions. When the widths are comparable to the propagation length of a leaky EM mode, the excitation of the leaky EM mode depends on the finite widths. To present this dependence clearly, let us consider the excitation by a beam with a finite width in only the x direction and essentially unlimited in the y direction. We will focus on the excitation of the leaky S-EM and $m = 0$ TM FP-EM waves. Extensions to excitation of other TM and TE leaky EM modes and to the excitation by a narrow beam with finite widths in both the x and y directions are straightforward.

Consider 1) an incident beam of a TM polarized V-EM wave within a prism, as in figure 1, having a lateral beam width along the prism-air interface W very much larger than either the wavelength (diffraction effects can be neglected) or the air gap, but comparable to or smaller than the propagation length of the leaky S-EM waves, and 2) a "reflected" beam for which lateral beam width is determined by a slit placed in front of the detector. At the prism-air interface, the component of the electric field parallel to the interface within the prism is given by

$$E_x^i(\theta_i, x, z = 0) = F(x) \exp(iK_x^0 x) \cos \theta_i \quad (16)$$

where $F(x)$ is the lateral form factor of the incident V-EM beam at $z = 0$, chosen, for simplicity, to be symmetrical with its center at $x = 0$; θ_i is the angle of incidence of the central ray of the incident beam; and $K_x^0 = (\eta\omega/c) \sin\theta_i$.

$E_x^i(\theta_i, x, z = 0)$ can be expressed as a Fourier integral over plane waves, i.e., the incident beam can be represented by a superposition of plane waves of different K_x and amplitude, as follows:

$$E_x^i = E_x^i(\theta_i, x, z = 0) = \int_{-\infty}^{\infty} \phi(K_x) \exp(iK_x x) dK_x = \int_{-\infty}^{\infty} E_x(K_x) dK_x \quad (17)$$

where

$$\phi(K_x) = \frac{1}{2\pi} \int_{-\infty}^{\infty} E_x(\theta_i, x, z = 0) \exp(-iK_x x) dx \quad (18)$$

All partial waves $E_x(K_x)$ of this beam have the $x-z$ plane as their common plane of incidence and are TM polarized.

The electric field of the EM wave which is "reflected" (i.e., reradiated) back into the prism and the electric field of the EM wave which is "transmitted" into the metal at the metal-air interface are given by summing the reflected and the transmitted partial waves as:

$$E_x^r = E_x^r(\theta_i, x, z = 0) = \int_{-\infty}^{\infty} r(K_x) E_x(K_x) dK_x \quad (19)$$

$$E_x^t = E_x^t(\theta_i, x, z = -d) = \int_{-\infty}^{\infty} t(K_x) E_x(K_x) dK_x \quad (20)$$

where $r(K_x)$ and $t(K_x)$ are given by equations (4) and (5) respectively.

When K_x is close to K_g' (where K_g' is the real part of the wavevector

K_y of the leaky S-EM wave), $r(K_x)$ and $t(K_x)$ can be expressed in terms of K_x as in equations (11) and (12).

By substituting equations (11) and (12) into equations (19) and (20), and applying convolution theory, we obtain

$$E_x^r = AE_x^i + iBE_x^s \quad (21)$$

$$E_x^s = iCE_x^s \quad (22)$$

$$E_x^s = \exp(iK_s x) \int_{-\infty}^x E_x^i(\theta_i, x', z = 0) \exp(-iK_s x') dx' \quad (23)$$

The term AE_x^i in equation (21) represents the "mirror reflection" of the incident beam, which is due primarily to the reflection at the prism-air interface. The second term, iBE_x^s , represents the field of the V-EM waves "radiated" by the excited leaky S-EM waves. Because the constant B is predominantly imaginary and positive, the first and second terms are 180° out of phase with each other. Furthermore, because of the difference in the spatial distribution of the mirror-reflected component and the radiated component (the latter has a maximum near the leading edge of the incident beam and decays exponentially out of the beam width), the "reflected intensity" generally will exhibit a double-peak spatial structure. The appearance of a second peak is due primarily to a destructive interference between the mirror-reflected and radiated fields, which have comparable amplitudes. The effect occurs when the radiative damping, which also indicates the degree of coupling efficiency of a leaky S-EM wave, is comparable to or larger than the intrinsic damping, that is, when the air gap, d , is comparable to or smaller than

the optimum air gap.³⁵ When the air gap is much larger than the optimum air gap, $|B|$ becomes much smaller than $|A|$ and the second peak disappears. The constant C is predominantly imaginary and negative. Thus, E_x^t has essentially the same phase as E_x^i .

We note that the integral of equation (23) is negligible for $x < W/2$ where $E_x^i(\theta_1, x, z = 0) \approx 0$, and is equal to a constant S for $x > W/2$. Thus, for $x > W/2$, i.e., for x beyond the excitation region, the expressions for E_x^r and E_x^t reduce to $E_x^r(\theta_1, x, z = 0) = iBS \exp(iK_s x)$ and $E_x^t(\theta_1, x, z = -d) \approx iCS \exp(iK_s x)$. These fields represent free (i.e., propagating) "leaky" S-EM waves which have a propagation length $L = 1/(4\pi K_s)$ and which radiate energy within the prism at an angle θ_0 , relative to the normal, where $\theta_0 = \sin^{-1} [K_s'/(K_s'^2 + K_{sz}^2)^{1/2}]$. When $K_s'' \ll K_s'$, θ_0 is the same as the angle θ_s [$= \sin^{-1} (ck_s'/\pi\omega)$] of resonant excitation of the leaky S-EM wave by a plane V-EM wave.

Integration of equation (23) can be carried out analytically when $F(x)$ has a Gaussian form, i.e., $F(x) = E_0 \exp(-4x^2/W^2)$. In this situation, we obtain the following expressions for $|E_x^t(\theta_1, x, z = -d)|$ at the metal surface and for the intensity I_r of the "reflected radiation"²⁶ in the prism:

$$I_r^r(\theta_1, x, z = 0) = |AF(x) \exp(iK_x^0 x) + iBG \exp(iK_s x)|^2 \quad (24)$$

$$|E_x^t(\theta_1, x, z = -d)| = |\cos\theta_1 CG \exp(iK_s x)| \quad (25)$$

$$G = (W/2) \exp[-(K_x^0 - K_s)^2 W^2/16] \{1 + \text{erf}[2x/W - i(K_x^0 - K_s)W/4]\} E_0 \quad (26)$$

The dependence⁶ of $E_x^t(\theta_1, x, z = -d)$ on x at $\theta_1 = \theta_s$ for several values of W is shown in figure 6. $|E_x^t/E_0|$ builds up to a maximum near the leading edge of the incident beam and decays exponentially beyond the excitation region. As W increases, the height of the maximum increases and approaches the value for an incident plane wave. We note that for weakly damped surface EM waves (where $K_s'' \ll K_s'$), the dependence of G and, therefore, of $E_x^t(\theta_1, x, z = -d)$ on θ_1 will exhibit sharp peaks at $K_x^0 = K_s'$ (i.e., at $\theta_1 = \theta_s$) for values of x both within and beyond the excitation region.

The dependence²¹ of I^r on x at $\theta_1 = \theta_s$ is represented in figure 7 by P^r versus x (solid line), where $P^r(\theta_1, x, w_c) = \int_{x - w_c/2}^{x + w_c/2} I(\theta_1, x') dx'$, and w_c is the lateral width of the detector slit, as shown in the inset of figure 9. The P^r curve shows a double-peak structure with an exponential decay beyond the excitation region. The profile of the incident Gaussian beam used for calculation is shown in the same figure by the dotted line, which also represents the dependence of I^r on x at $\theta_1 \neq \theta_s$. P^r is smaller when $\theta_1 = \theta_s$ than when $\theta_1 \neq \theta_s$ for values of x within the excitation region and larger for values of x beyond the excitation region. Therefore, the angular dependence of the reflected intensity $I^r(\theta_1, x, z = 0)$ will exhibit ATR-type minima at θ_s for values of x within the excitation region and peaks for values of x beyond.

4. Narrow-beam excitation - experimental

The experimental setup is shown in figure 8. A TM-polarized, cw CO₂ laser beam ($\lambda = 10.6 \mu m$) is incident into a prism-air-Ag configuration.

Measurement indicated that the incident beam has a Gaussian profile. The prism is made of a NaCl crystal which has $n = 1.49$ at $10.6 \mu\text{m}$. The air gap is controlled by a translator with an accuracy of $\pm 2 \mu\text{m}$. A 3-mm and a much narrower (0.125-mm) slit define the width of the incident beam and the collecting width, respectively. The slits set $W = 4.05 \text{ mm}$ and $W_c = 0.17 \text{ mm}$. The detecting slit is fixed in front of a pyroelectric detector which can be translated normal to the mirror reflection direction to measure the spatial dependence of I^r . The incident angle is scanned by rotating the prism-air-Ag configuration with respect to the incident beam. Both the configuration and the detector are mounted on a turntable so that the detector, which rotates twice as fast as the sample, can track the "reflected" beam to measure the angular dependence of I^r .

Figure 9 shows the experimental curve²¹ of the (normalized) power P^r (θ_i, x, W_c) vs x for $d = 38 \pm 2$ microns at $\theta_i = \theta_s = 42^\circ$, together with the corresponding theoretical curve based on $\epsilon_{\text{NaCl}} = 2.22$ and $\epsilon_{\text{Ag}} = -3850 + i 1450$. Apart from the magnitude of the minimum, the experimental and theoretical curves agree relatively well. The discrepancy between the theoretical and experimental curves is due to roughness scattering and surface contamination effects and to the small deviation of the incident beam from a Gaussian profile. The double peak structure is clearly evident, as is the exponential decay of P^r beyond the region of excitation. From the decay, we obtain a value of $1.6 \pm 0.05 \text{ mm}$ for L , which is in reasonable agreement with the computer-calculated theoretical value of 1.66 mm for the leaky S-EM wave.

Experimental curves of P^r vs θ_i for different values of x are also given in figure 9. As expected, these curves show sharp minima for values

of x in the vicinity of $x = 0$ and sharp peaks for values of x beyond the excitation region. The magnitudes of the peaks decrease with increasing x . The occurrence of these peaks, signaling the presence of free leaky S-EM waves, is the most significant feature of S-EM wave excitation by V-EM waves of finite beam width. Furthermore, we note that the leading edge of the incident V-EM radiation is responsible for 1) the occurrence of the reflected minima and 2) the exponential decay of the reflected intensity, whereas the back edge primarily determines the amplitude of the excited S-EM waves.

In figure 10, we present data on the excitation⁵ of the $m = 1$ TM FP-EM waves by a narrow beam. The sample configuration is the same as the one described above, except $d = 51 \mu\text{m}$. Experimental curves of P^F vs θ_1 show sharp minima for $x = 0$ and sharp peaks for $x = 2.7 \mu\text{m}$ at two resonance angles. The left-hand features signal the excitation of a S-EM wave and the right-hand features signal the excitation of a $m = 1$ FP-EM wave. The excitations of $m = 2, 3, \dots$ FP-EM modes are off the scale. Since we can detect the radiation from the $m = 1$ FP-EM wave at $x = 2.7 \mu\text{m}$, we conclude that the $m = 1$ FP-EM wave also has a macroscopic propagation length. Because FP-EM waves in a prism-air-metal configuration can propagate longer in the visible than in the infrared, the same experimental setup can be easily extended to measure the propagation length of FP-EM waves in the visible.

5. Discussion

Narrow-beam excitation is one of the most important processes used in two-prism propagation studies of S-EM waves. As shown in figure 11(a),

an incident narrow beam in the left-hand prism launches S-EM waves at the air-metal interface, which after propagating a distance, are recovered in the right-hand prism. The leaky S-EM wave in the launching ATR configuration is converted to a S-EM wave in the middle area at the prism edge. In the recovery process, the conversion is reversed. The excited leaky S-EM wave in the launching ATR configuration leaks back into the prism during propagation before it reaches the edge. Thus, the launching efficiency depends on the power of the leaky S-EM wave that reaches the edge. If we let the leaky edge of the narrow beam coincide with the prism edge, then, from the beam-width dependence of $|E_x^t/E_0|$ at the edge in figure 6, one sees the dependency of the power which can reach the edge on the width of the incident beam.

The interconversion of the EM modes at the prism edge is another important process which influences the launching efficiency. An effective interconversion is achieved when there is a close match between the phase velocities of the EM modes at both sides of the edge. Two approaches can be used to adjust the phase match. One is to trim the leading edge³⁶ of the launching prism to the shape shown in figure 11(b) to obtain a gradual change of the phase velocities from one side to the other. The other is to adjust the air gap.³⁶ In general, the larger the air gap, the closer the match. However, the larger the air gap, the weaker the coupling efficiency of the leaky S-EM waves.

Although the air-gap dependence of the launching efficiency has been experimentally examined in both parallel³⁶ and tilted air-gap situations,³⁷ an overall study of the effect of beam width on the launching efficiency, as well as the effect of the air gap, still is needed. The

narrow-beam excitation discussed here can serve as the starting point to achieve this goal.

Two-prism configurations have been successfully used as a spectroscopic tool for studying ultra-thin layers on metal surfaces.³⁸ By studying the propagation of the S-EM waves, we can use the narrow-beam one-prism configuration as a similar spectroscopic tool.^{6,14} The one-prism configuration can be considered a limiting case of the two-prism configuration, i.e., the same prism serves to both launch and recover. The known major disadvantage of "real" two-prism S-EM wave spectroscopy is the need, because of the low launching efficiency, for an intense infrared laser beam as a launching source.³⁸ However, since no prism edge is involved in the one-prism configuration, there are no reflection and conversion losses. With this advantage, the combination of a conventional infrared source and a monochromator can supply infrared EM waves with enough intensity to use the propagation study as a spectroscopic tool. Furthermore, since the propagation and the detection of the leaky EM modes can be formulated exactly, the data can be analyzed exactly.

A 100-Å-thick SiO_x overlayer on a Ag substrate has been studied by investigating the propagation of leaky S-EM waves in an ATR configuration with a 20- μm air gap.^{6,12} Narrow infrared beams (5 mm in width) with λ from 5 μm to 11 μm , provided by a monochromator with a globar source, excited leaky S-EM waves to propagate out of the illuminated region. The radiation beyond the illuminated region was collected as a function of the incident angle.

The radiation intensity P^r versus θ curves are shown in figure 12(a). The curves show peaks at angles where the leaky S-EM waves were excited. With the P^r versus θ curves for the case without SiO_x film [shown in figure 12(b) for comparison], we found that the peak heights were reduced from $\lambda = 8 \text{ \mu m}$ to 9 \mu m . The reduction is due to the decreased propagation length of leaky S-EM waves in that wavelength region in the presence of the SiO_x overlayer. The maximum reduction occurs at $\lambda = 8.3 \text{ \mu m}$, shown in the peak height versus λ plot (figure 13). This wavelength corresponds to the longitudinal phonon frequency (ω_{LO}) of a SiO_2 medium. The result having the maximum reduction at ω_{LO} agrees with theoretical predictions.^{6,39,40} From this study, we conclude that the SiO_x layer is a SiO_2 layer.

Since the FP-EM modes can also propagate macroscopic distances in the infrared, they, as well as the leaky S-EM waves, serve as an EM-surface probe. Since we know that S-EM waves can only propagate about 10 \mu m in the visible, their propagation cannot be used as a visible spectroscopic tool. On the other hand, FP-EM waves propagate even longer in the visible than in the infrared and, therefore, can serve as a surface probe in the visible.

Because S-EM waves are TM polarized, they have both E_x and E_z components and can be used to probe vibrational modes of an adsorbed molecule having transition dipoles normal and parallel to the metal surface. Although the electric field of a S-EM wave in the infrared is mainly perpendicular to the metal surface, due to the difference in oscillation strength between transition dipoles normal to the surface and those parallel to the surface, the direction of the transition dipole, and therefore, the corresponding chemical bond, can not be identified just

by examining the absorption strength of the S-EM waves. Neither can identification be achieved by using only TM FP-EM waves. However, TE FP-EM waves which have only an E_y component also exist. The TE FP-EM waves thus will probe only vibrational modes of a molecule having transition dipoles parallel to the surface. If the results obtained from both TM and TE FP-EM waves are combined, it is possible to identify the direction of the chemical bonds of the adsorbed molecules.

Excitation of a S-EM wave with a grating coupler also depends on the width of the incident beam. Theoretically, it has been shown⁴¹ that, when a narrow pulse is incident upon a grating, the frequency spectrum of the reflected pulse is distorted from that of the incident pulse at the resonant excitation of a S-EM wave, if $W < v_g/\sigma$ (where v_g is the group velocity of the S-EM wave and σ is a measure of the spread of frequencies of the incident pulse). Bisecting a grating and separating the two halves, produces the two-grating propagation configuration.⁴² Thus, narrow-beam excitation in a grating coupler plays an important role in the launching efficiency of a S-EM wave in a two-grating propagation configuration, analogous to its role in a two-prism configuration.

There are alternative ways to excite S-EM waves locally. They can be excited by a local oscillator having a lateral dimension smaller than the propagation length of the corresponding S-EM wave. Although a broad beam may be used to excite the local oscillator, the excitation of S-EM by the oscillator is indeed local. An example is the configuration shown in figure 14(a) and used by Chabal and Sievers⁴³ to launch S-EM waves at an air-metal interface. An incident beam enters the prism and strikes the base at the edge of the metal film. We believe that the

S-EM waves are excited by localized EM modes at the edge, which are themselves excited by the incident beam. Similarly, it should also be possible to launch S-EM waves by the conversion from EM modes, localized at a bump or a dip, as shown in figures 14(b) and 14(c), respectively.

6. Conclusion

Both leaky surface EM waves and TM and TE Fabry-Perot EM waves exist in an Otto ATR configuration. The FP-EM waves are due to interference of two propagating EM waves which are incident at grazing angles upon the metal and the prism base. When excited by volume electromagnetic radiation of finite beam width, the excited leaky electromagnetic modes build up along the excitation region and propagate as free damped waves beyond. Correspondingly, the spatial dependence of the reflected intensity exhibits a double-peak interference structure at the leading edge of the excitation region followed by an exponential decay beyond. The appearance of a second peak is due primarily to a destructive interference between a mirror-reflected field and a radiated field which are 180° out of phase. The phase velocity and the propagation length of the leaky EM modes can be determined from the coupling angle and the exponential decay, respectively.

When the incident angle is scanned, the angular dependence of the reflected intensity exhibits ATR-type minima at the coupling angle from the excitation region and peaks from the free-wave region. Study of the peaks provides a tool for the spectroscopic study of an overlayer. The study can be performed in the infrared by using leaky surface EM waves

and FP-EM waves and in the visible by using FP-EM waves, due to their long propagation lengths. The advantage of using finite-beam excitation in a one-prism configuration in the spectroscopic study is its high efficiency, i.e., a conventional infrared source can provide enough intensity for propagation experiments. The use of both TM and TE ^oP-EM waves provides a way to identify the direction of chemical bonds of adsorbed molecules on metal surfaces.

7. Acknowledgements

This work was supported in part (WPC) by contract DAAG 29-77-C-0036 from the Army Research Office and in part (EB) under contract N00014-76-C-0107 from ONR. We would like to thank G. Ritchie and Y.J. Chen for their critical reading of this manuscript.

References

1. A. Otto, Z. Phys., 216, 398 (1968).
2. E. Kretschmann, Z. Phys., 241, 313 (1971).
3. E. Burstein, W.P. Chen, Y.J. Chen and A. Hartstein, J. Vac. Sci. Technol., 11, 1004 (1974).
4. A. Hjortsberg, W.P. Chen and E. Burstein, Appl. Opt., 17, 430 (1978).
5. W.P. Chen, A. Hjortsberg and E. Burstein, Bull. Am. Phys. Soc., 22, 438 (1977); and to be published.
6. W.P. Chen, Ph.D. Thesis, University of Pennsylvania, 1977.
7. G. Wahling, H. Raether and D. Mobius, Thin Solid Films, 58, 391 (1979).
8. C.F. Eagen and W.H. Weber, Phys. Rev. B., 19, 5068 (1979).
9. W.H. Weber, Phys. Rev. Letters, 39, 153 (1977).

10. W.P. Chen and J.M. Chen, *Surf. Sci.*, 91, 601 (1980).
11. A. Hjortsberg, W.P. Chen, E. Burstein and M. Pomerantz, *Opt. Commun.*, 25, 65 (1978).
12. W.P. Chen, A. Hjortsberg and E. Burstein, Optical Phenomena in Infrared Materials, Annapolis Meeting (1976); and to be published.
13. I. Pockrand, *Surf. Sci.*, 72, 577 (1978).
14. I. Pockrand, J.D. Swalen, J.G. Gordon II and M.R. Philpott, *Surf. Sci.*, 74, 237 (1978).
15. F. Abeles and T. Lopez-Rios, in Proc. Taormina Conf. on Polaritons, edited by E. Burstein and F. DeMartini (Pergamon, New York, 1974) pp. 241 ff.
16. T. Lopez-Rios, *Opt. Commun.*, 17, 342 (1978).
17. T. Lopez-Rios and G. Vuye, *Nuova Cimento*, 89B, 823 (1977).
18. B.A. Loisel and E.T. Arakawa, in press.
19. E.T. Arakawa, M.H. Williams, N.R. Hamm and R.H. Ritchie, *Phys. Rev. Lett.*, 31, 1127 (1973).
20. R.W. Alexander, G.S. Kovener and R.J. Bell, *Phys. Rev. Lett.*, 32, 154 (1974).
21. W.P. Chen, G. Ritchie and E. Burstein, *Phys. Rev. Lett.*, 37, 993 (1976).
22. K. Bhasin, D. Bryan, R.W. Alexander and R.J. Bell, *J. Chem. Phys.*, 64, 5019 (1976).
23. J. Schoenwald, E. Burstein and J.M. Elson, *Solid State Commun.*, 12, 185 (1973).
24. D.A. Bryan, D.L. Begley, K. Bhasin, R.W. Alexander, R.J. Bell and R. Gerson, *Surf. Sci.*, 57, 53 (1976).
25. D.L. Begley, R.W. Alexander, C.A. Ward, R. Miller and R.J. Bell, *Surf. Sci.*, 81, 245 (1979).
26. T. Tamir and H.L. Bertoni, *J. Opt. Soc. Am.*, 61, 1397 (1971).
27. A. Otto, in Optical Properties of Solids: New Developments, edited by B. Seraphin (North-Holland, Amsterdam, 1976) pp. 677 ff.

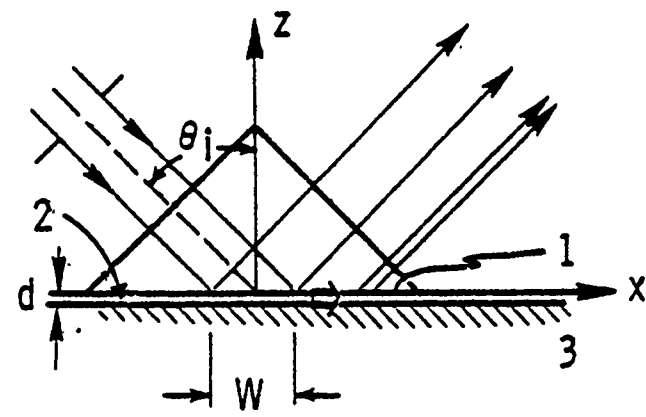
28. D.L. Mills and E. Burstein, *Rep. Prog. Phys.*, 37, 817 (1974).
29. K.L. Kliener and R. Fuchs, in Advances in Chemical Physics, edited by I. Prigogine and S. Rice, Vol. 27 (Wiley, New York, 1974) pp. 335 ff.
30. E.N. Economou and K.L. Ngai, in Advances in Chemical Physics, edited by I. Prigogine and S. Rice, Vol. 27 (Wiley, New York, 1974) pp. 205 ff.
31. R.H. Ritchie, *Surf. Sci.*, 34, 1 (1973).
32. R. Ruppin and R. Englman, *Rep. Prog. Phys.*, 33, 101 (1970).
33. M. Born and E. Wolf, Principles of Optics (Pergamon, New York, 1959), pp. 327 ff.
34. B. Dold and R. Mecke, *Optik*, 22, 435 (1965).
35. A. Otto, in Proc. Taormina Conf. on Polaritons, edited by E. Burstein and F. DeMartini (Pergamon, New York, 1974) pp. 117 ff.
36. D.L. Begley, D.A. Bryan, R.W. Alexander and R.J. Bell, *Appl. Optics*, 16, 1549 (1977).
37. D.J. Whittle, A. Hjortsberg and E. Burstein, *Bull. Am. Phys. Soc.*, 23, 277 (1978).
38. R.J. Bell, R.W. Alexander and C.A. Ward, in press.
39. C.A. Ward, R.W. Alexander and R.J. Bell, *Phys. Rev.*, B12, 3293 (1975).
40. V.M. Agranovich and A.G. Malshukov, *Opt. Commun.*, 11, 169 (1974).
41. D.L. Mills, *J. Appl. Phys.*, 48, 2918 (1977).
42. J. Schoenwald and E. Burstein, *Bull. Am. Phys. Soc.*, 19, 323 (1974).
43. Y.J. Chabal and A.J. Sievers, *Appl. Phys. Lett.*, 32, 90 (1978).

Figure Captions

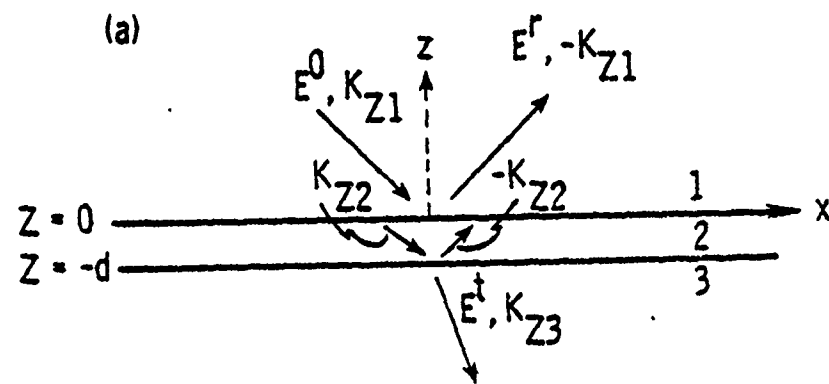
1. The single-prism Otto configuration. The prism, air, and the metal are labeled as media 1, 2, and 3.
- 2(a). Schematic diagram showing an incident V-EM wave and its reflected and transmitted V-EM waves in a prism-air-metal (1-2-3) configuration.
(b). The EM wave in the prism of a leaky EM mode. The array represents the direction of Poynting vector. The density of lines shows exponential decay of radiative intensity of the leaky EM mode (from reference 6).
3. The real ω versus K curves of leaky EM modes of a prism-air-Ag configuration. The parameters used for calculation are $d = 38 \text{ } \mu\text{m}$, $\epsilon_1 = 2.25$, $\epsilon_2 = 1$, and $\epsilon_3(\omega) = 4.44 (1 - 9 \times 10^8 / \omega [\omega + 1600])$. The curves of S-EM waves and of TM FP-EM waves are labeled as S and $m = 0, 1, 2$, and 3, respectively. For comparison, the real ω versus complex K curve of S-EM waves of the corresponding air-Ag interface is shown as a dashed line.
(a) the ω vs $K' / (\omega/c)$ curves. The curves of S-EM waves and of $m = 0$ TM FP-EM modes are the different sections of the same single continuous curve. (b) The ω vs $K'' / (\omega/c)$ curves. The horizontal bar approximately separates the curves for S-EM waves and $m = 0$ TM FP-EM waves.
4. The air-gap dependence of $K' / (\omega/c)$ of a leaky S-EM wave of $\omega = 943 \text{ cm}^{-1}$. $K' / (\omega/c)$ decreases with decreasing d . For $d < 110 \text{ } \mu\text{m}$, $K' / (\omega/c)$ becomes less than 1 and the S-EM wave becomes a $m = 0$ TM FP-EM wave.
5. The R versus $K_x / (\omega/c)$ curves of an incident V-EM wave of a CO_2 laser ($\omega = 943 \text{ cm}^{-1}$) in a prism-air-Ag configuration. The right and the left minima of each curve correspond to excitation of $m = 0$ and $m = 1$ TM FP-EM, respectively. The minima corresponding to excitation of higher order modes are off the scale on the left-hand side.
6. The dependence of $E_x^t(\theta_i, x, z = -d)$ on x at $\theta_i = \theta_s$ for values of W . $|E_x^t/E_0|$ builds up to maxima near the leading edges, which are indicated as vertical bars, of the incident beams and decay exponentially beyond the excitation regions (from reference 6).

Figure Captions (Continued)

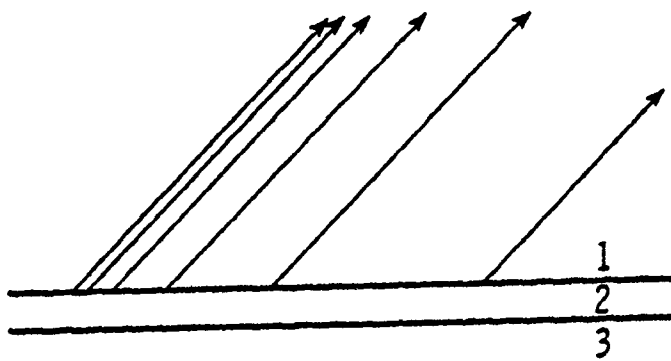
7. Curves of $P^r(\theta_i, x, W_c)/P^i(\theta_i, x = 0, W_c)$ vs x with $W = 4.05$ mm and $W_c = 0.17$ mm for a NaCl-air-Ag prism configuration having $d = 38$ microns. The experimental data for $\theta_i = \theta_s$ are represented by the dashed line and the corresponding theoretical curve by the solid line. The dash-dot-line represents the experimental data for θ_i away from θ_s and is the corresponding calculated curve for a beam having a Gaussian profile (from reference 21).
8. The experimental setup for the finite beam excitation of surface EM wave in a NaCl-air-Ag Otto configuration. CH: chopper, TT: turntable; S1 and S2: slits; T: translator; D: pyroelectric detector (from reference 6).
9. Experimental curves of $P^r(\theta_i, x, W_c)$ vs. θ_i for various values of x in mm. The data are obtained with a 3-mm slit in the incident beam and a 0.3-mm slit in front of the detector (from reference 21).
10. Experimental curves of $P^r(\theta_i, x, W_c)$ vs θ_i for $x = 0$ and 2.7 mm at $d = 51$ μ m. The propagation of the $m = 1$ TM FP-EM wave over a distance of 2.7 mm is clearly shown.
11. The two-prism Otto configuration (a) two truncated prisms (b) two trimmed prisms.
12. The P^r versus θ curves at various wavelengths as indicated for (a) a NaCl-air (20 μ m) - SiO_x (100 \AA) - Ag configuration and (b) its counterpart without the SiO_x film (from reference 12).
13. The wavelength dependence of the peak of the $P^r(\theta, \lambda)$ curves shown in figure 12 (from reference 12).
14. Schematic diagrams of (a) a prism-metal edge coupler (from reference 43), (b) a "bump" coupler, and (c) a "dip" coupler.

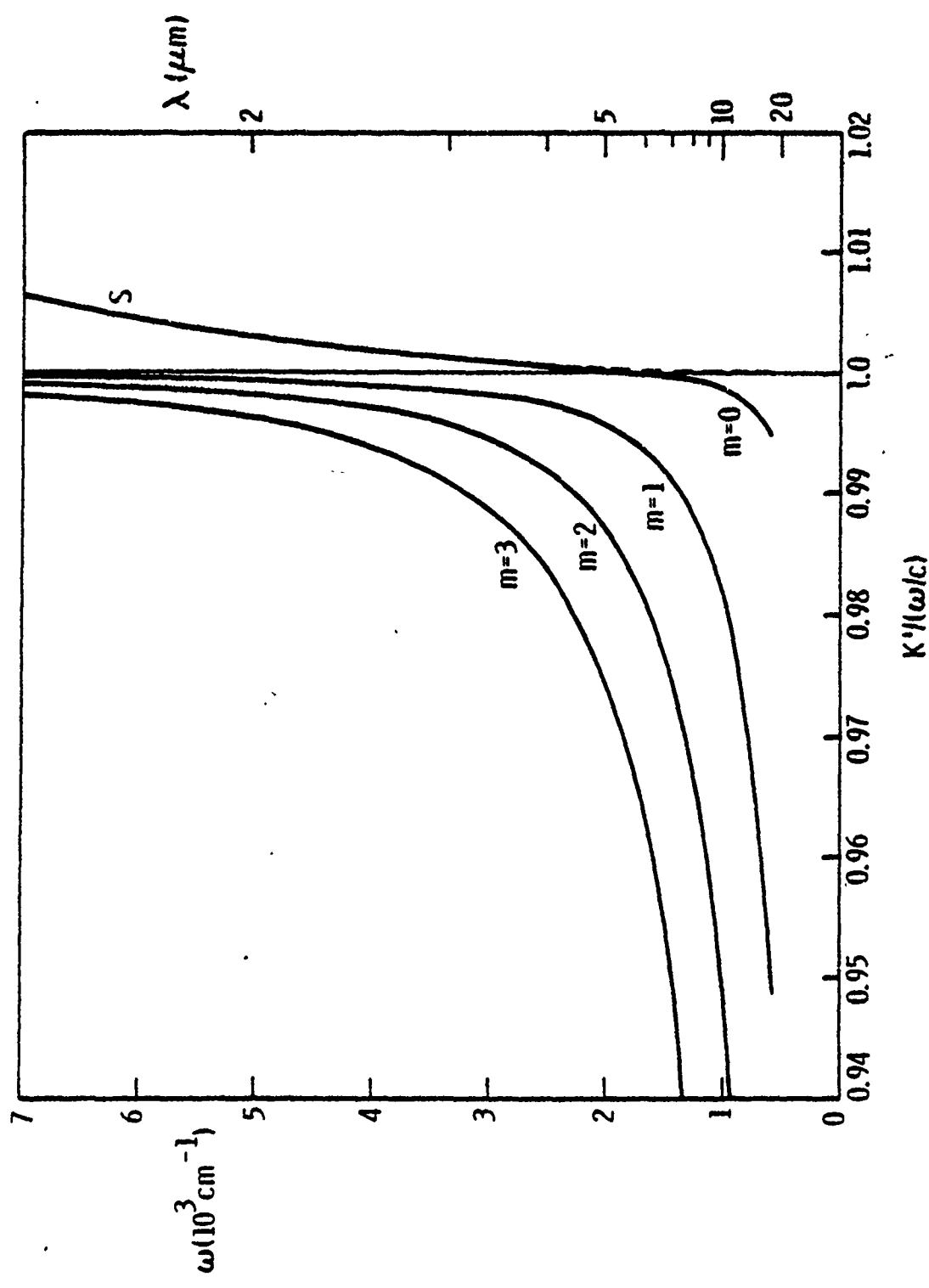


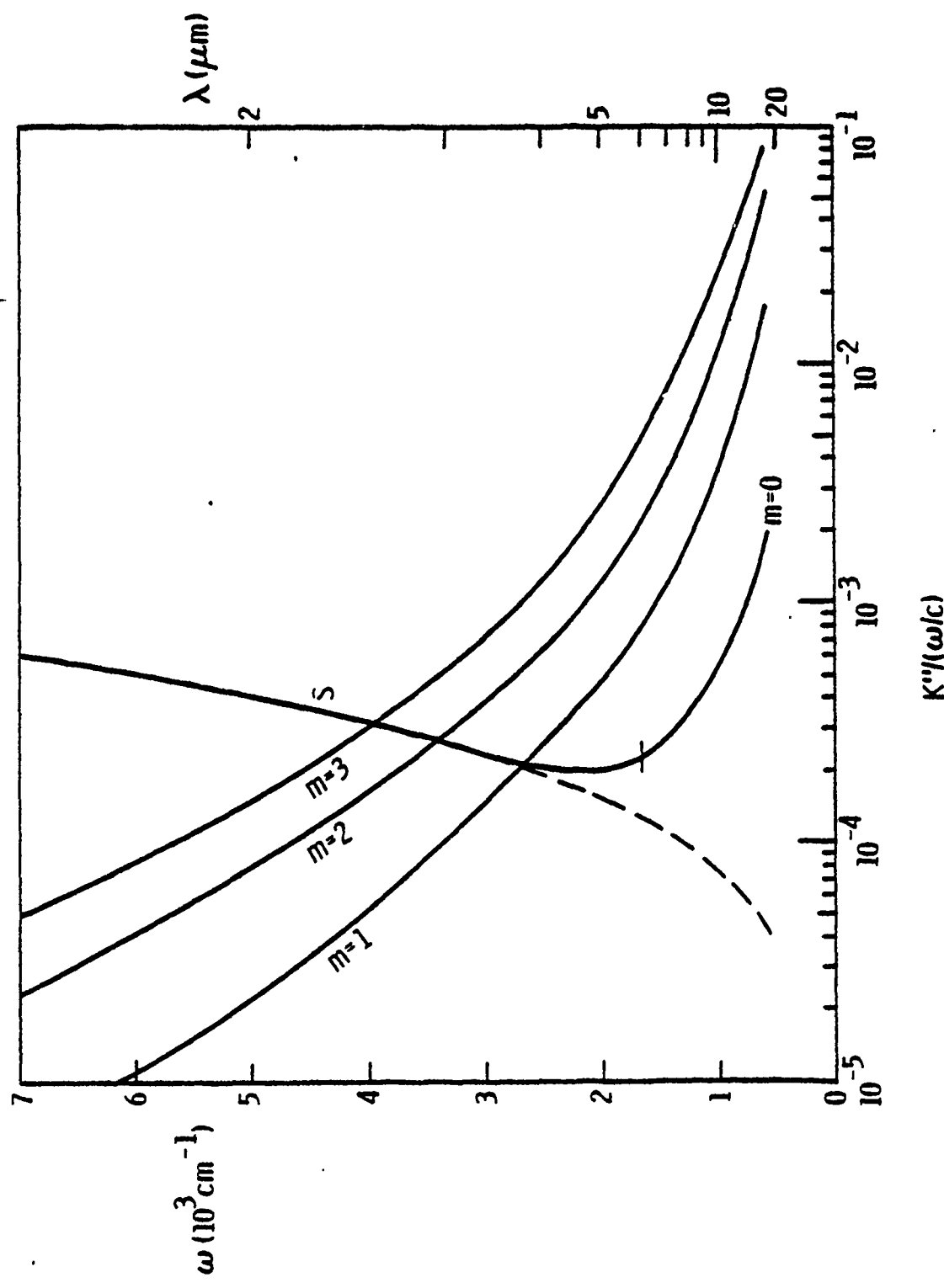
(a)

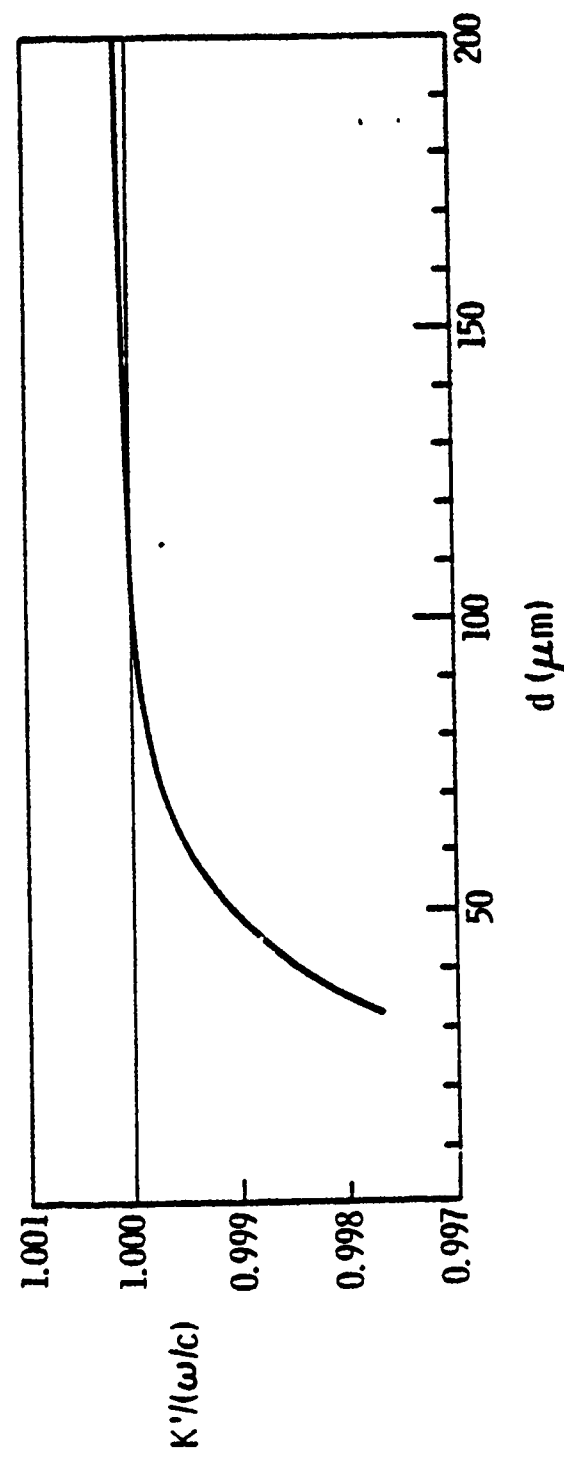


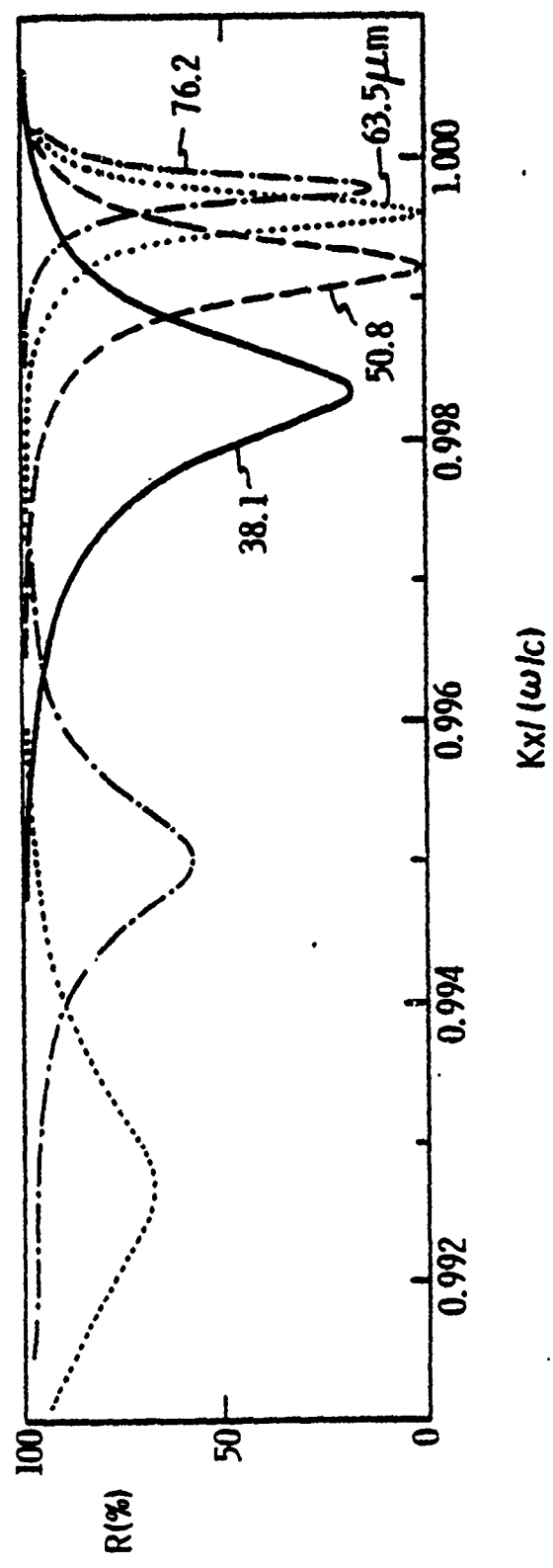
(b)

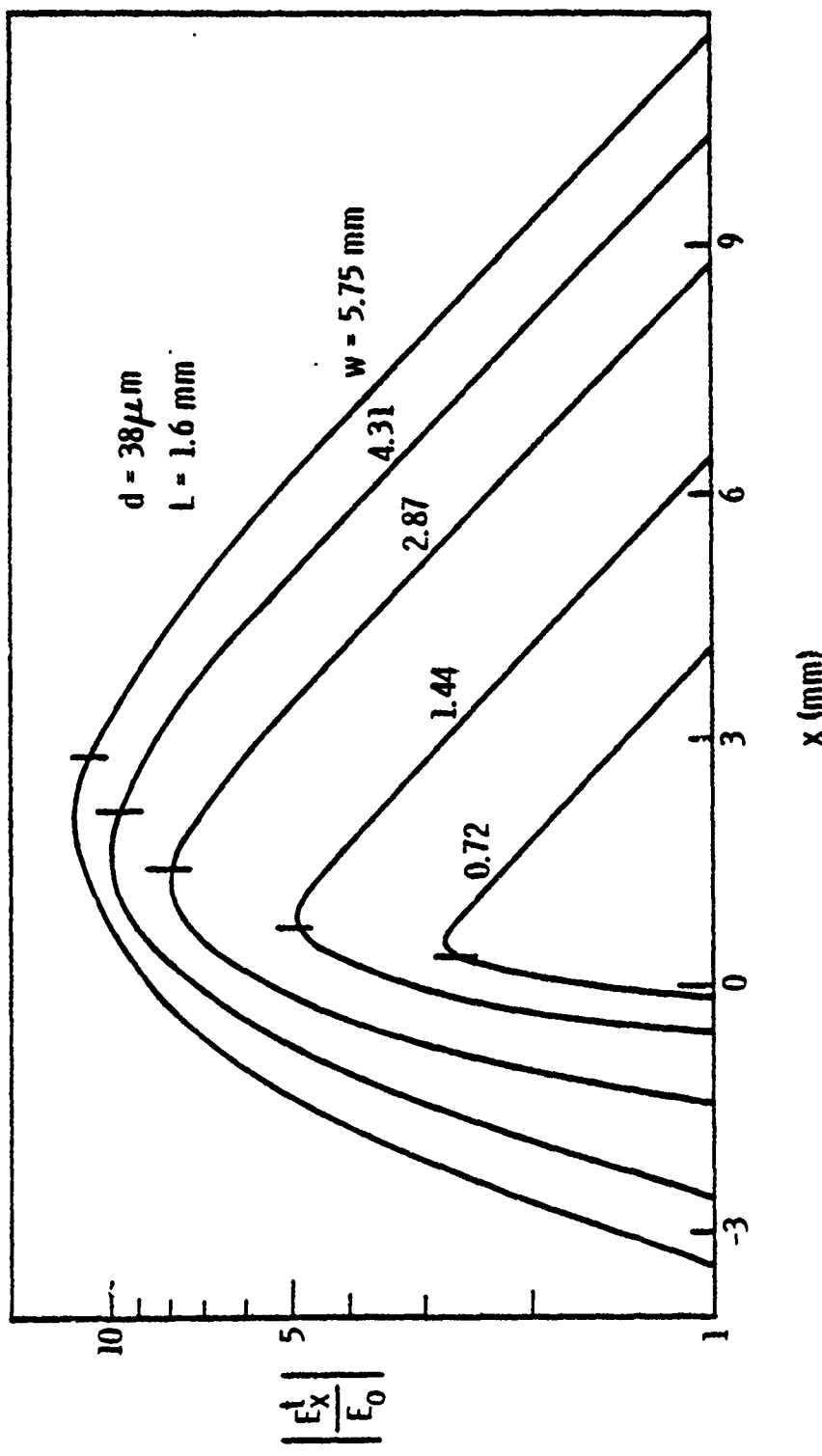


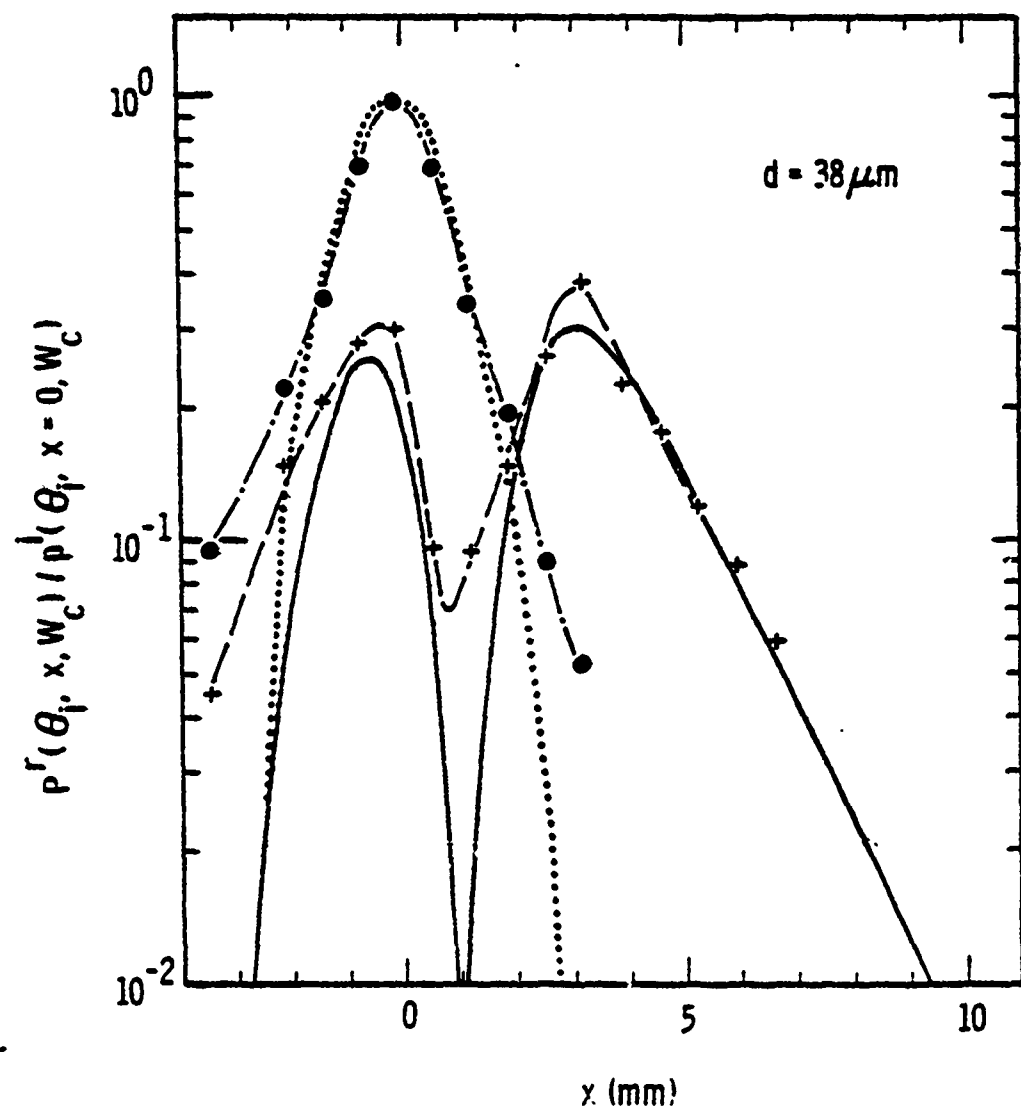


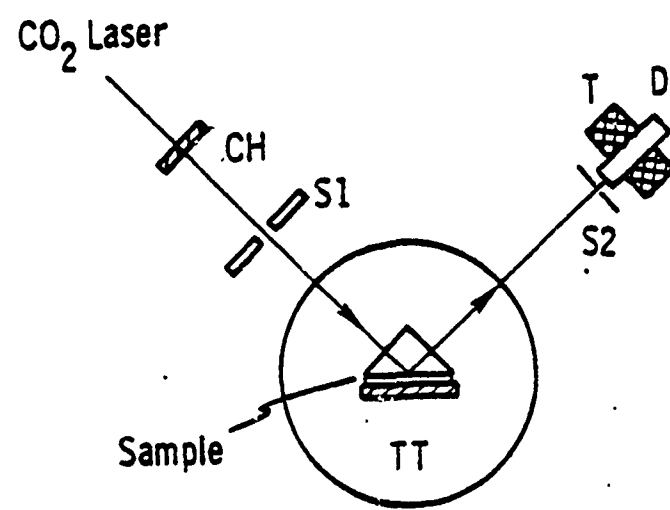


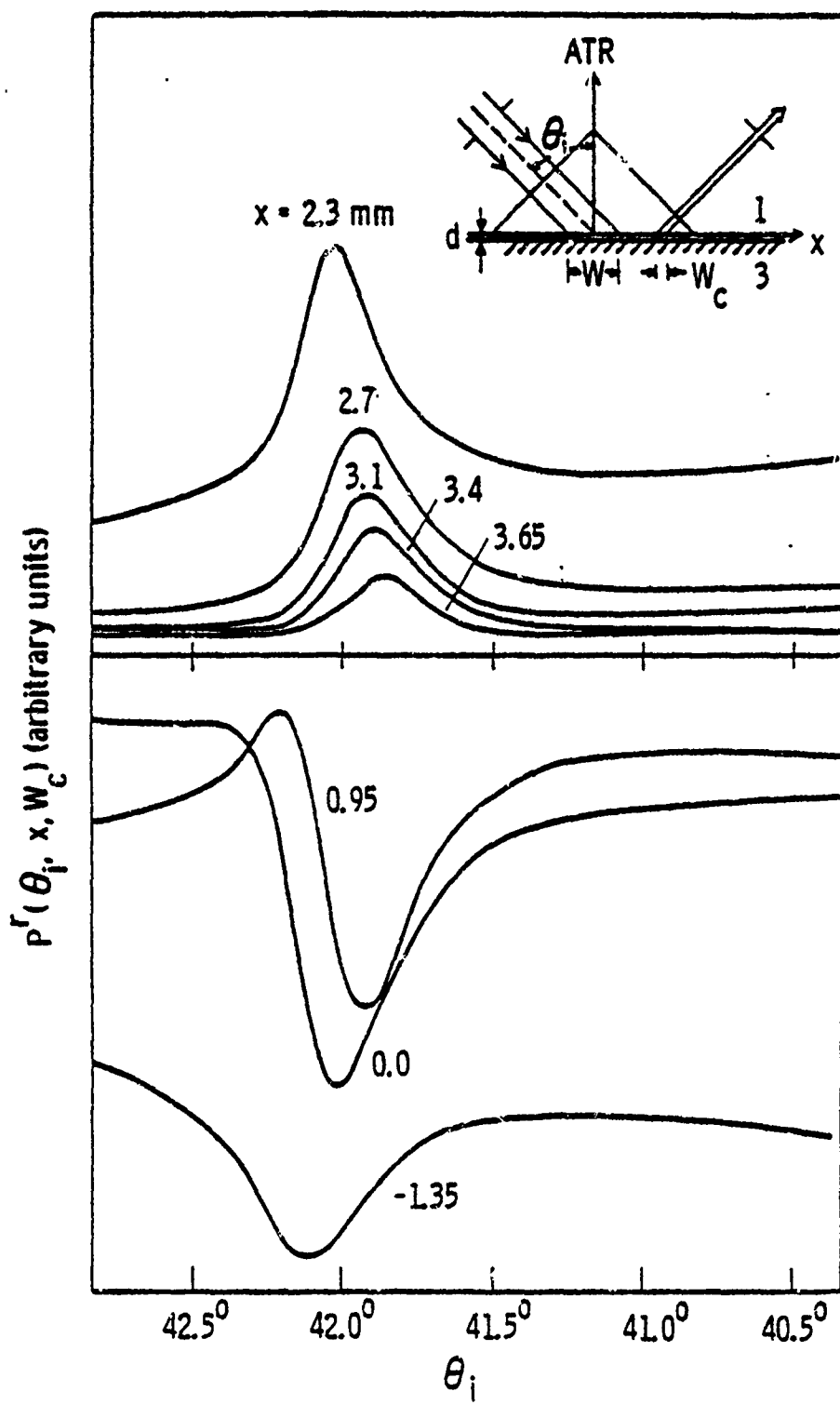


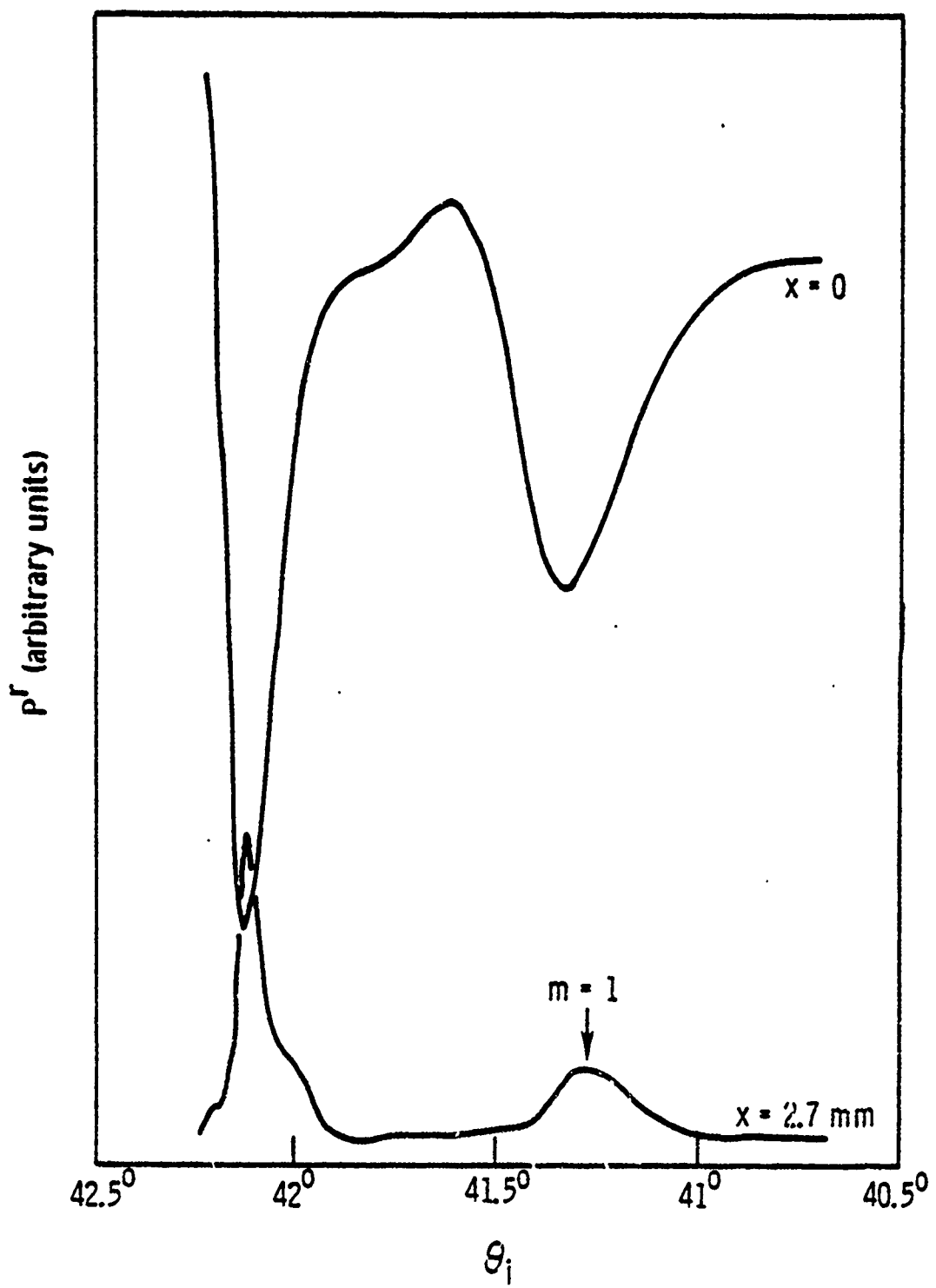




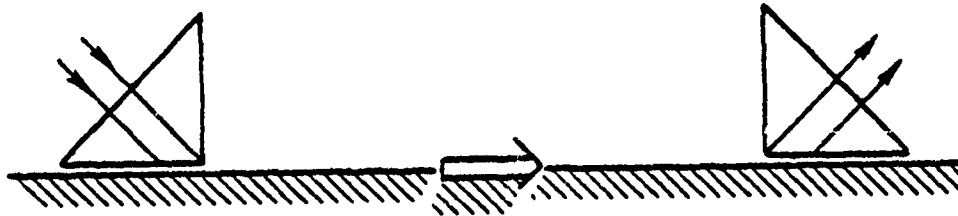




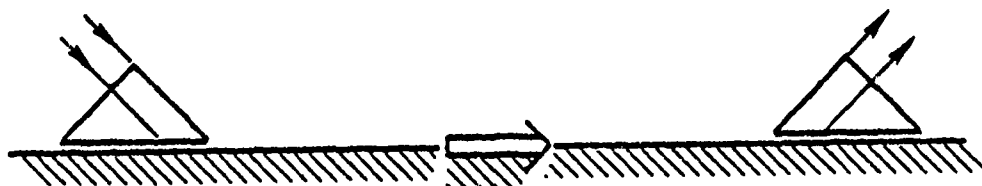


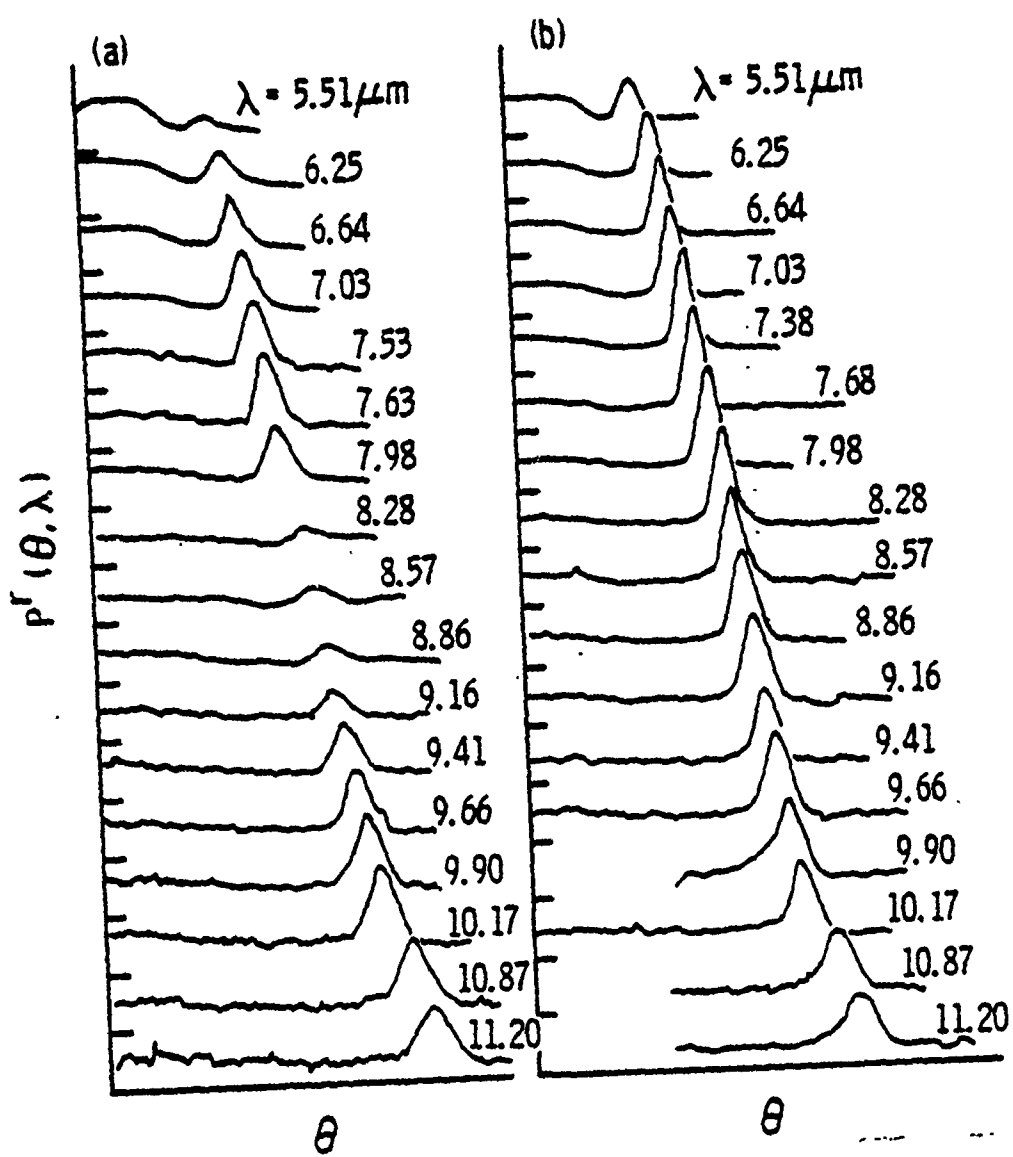


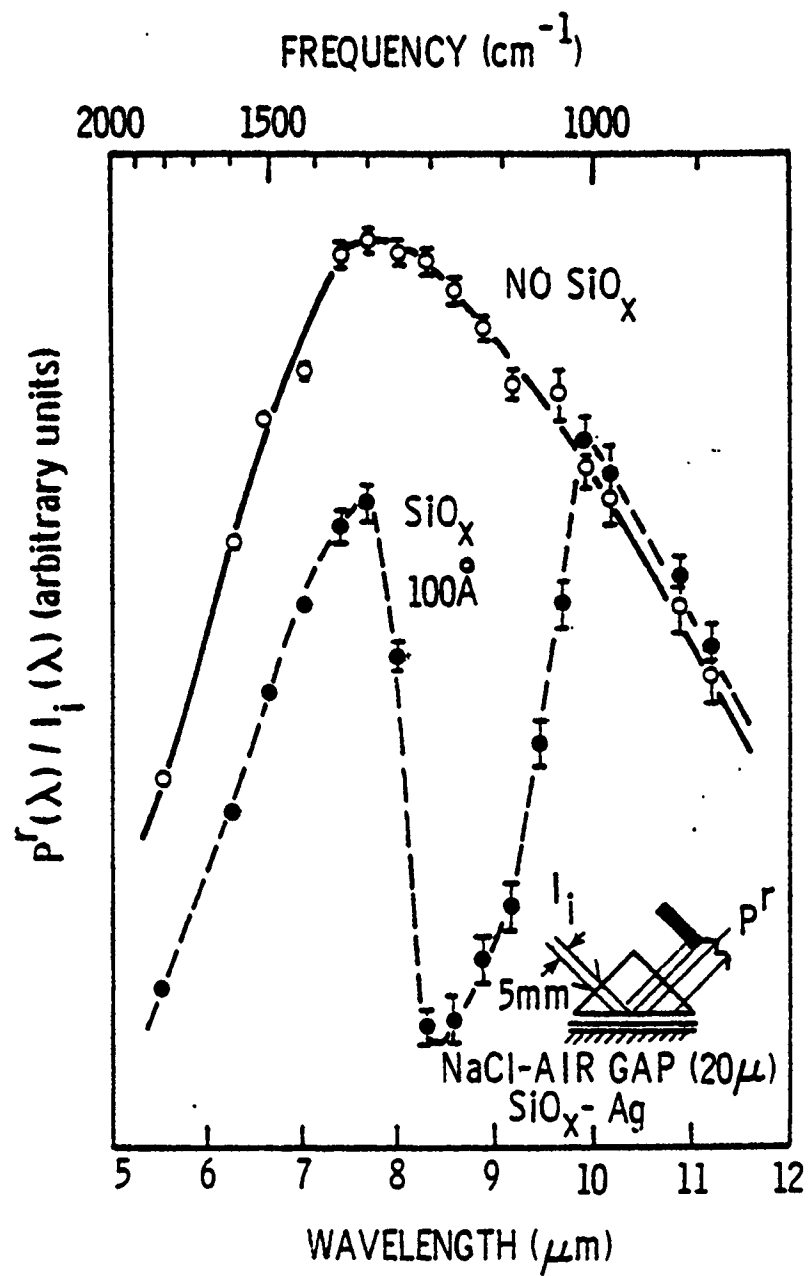
(a)



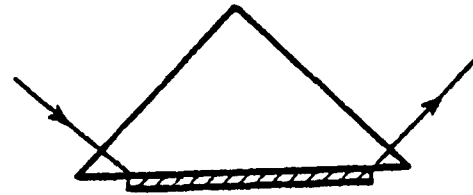
(b)



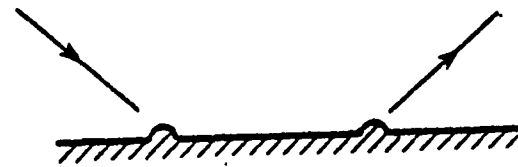




(a)



(b)



(c)

